U.PORTO

Universidade do Porto
FEUP Faculdade de Engenharia

Modelling and analysis of wind-excited vibrations of transmission lines

João Miguel Martins dos Santos

Dissertation submitted to
Faculdade de Engenharia da Universidade do Porto
for the degree of:

Mestre em Engenharia Mecânica

Advisor:
Professor José Dias Rodrigues
(Associate Professor)

Co-Advisor:
Doctor Pedro Miguel Guimarães Pires Moreira

Laboratório de Vibrações de Sistemas Mecânicos
Departamento de Engenharia Mecânica
Faculdade de Engenharia da Universidade do Porto

Porto, 2015

The work presented in this dissertation was performed at the
Laboratory of Vibrations of Mechanical Systems
Department of Mechanical Engineering
Faculty of Engineering
University of Porto
Porto, Portugal.

João Miguel Martins dos Santos
E-mail: em10003@fe.up.pt

Faculdade de Engenharia da Universidade do Porto
Departamento de Engenharia Mecânica
Laboratório de Vibrações de Sistemas Mecânicos
Rua Dr. Roberto Frias s/n, Sala M206
4200-465 Porto
Portugal

ABSTRACT

The study of transmission line performance started to take a more serious note in the late nineteen-sixties, due to the fact that a number of various failures occurred when the conductors started to have 20 to 25 years of use.

These types of failures are mainly fatigue type failures that are caused due to aeolian vibrations. One of the main applications that enables the reduction of these types of vibrations is the Stockbridge damper, that is normally used near the span ends of the conductor.

Throughout the years, the Energy Balance Method served as the main procedure to determine the evolution of the conductor's displacement due to aeolian vibration and the difference in the behaviour when dampers are used. However, this type of procedure depends on a high number of empirical values, both from the conductor and from the damper, leading to the conclusion that each case is somewhat unique and that it requires a significant amount of trial and error in order to have a fair estimation of the conductor's displacement. The method is also characterized for making a fairly large number of simplifications, most notably the disregard of the conductor's flexural rigidity.

This work tries a somewhat new approach to the study of aeolian vibration of conductors, with the introduction of the Finite Element Analysis into the study. The conductor and damper are modelled through this new philosophy of approach, and with these models, a custom designed Matlab program was created in order to run simulations for both free and forced vibration analysis. The program also allowed for heavy parametric-type analysis, which enabled the determination of an "optimal damper tuning" algorithm, which the results are shown in the present work.

Keywords: Aeolian vibration, Transmission lines, Stockbridge, damping, FEM

To my parents Margarida and Sebastião and to my brother Bruno

'Attitude is a little thing that makes a big difference.'

Winston Churchill

ACKNOWLEDGEMENTS

There is a great amount of people that I would like to thank for, people that helped me get where I am today and enabled me to do the present work this semester.

Firstly, I would like to thank my family for all the help throughout all the years of my engineering degree. Undoubtedly that without your help I could not have gone this far.

I would like to thank everyone at the Laboratório de Vibrações de Sistemas Mecânicos for all the help given throughout the entire semester, who helped immensely and always had a minute to spare.

I also owe a big thank you to Prof. Paulo Tavares de Castro for the help in finding relevant data regarding the conductor's fatigue damage.

For all the interest in the work developed and the availability in being my advisor, I also thank Dr. Pedro Moreira.

And lastly, I would like to thank Prof. José Dias Rodrigues for all the time, patience and dedication throughout the entire semester, that allowed me to have a complete new understanding of the complexity of the study of vibrations, which will most certainly be useful in the years to come.

CONTENTS

LIST OF FIGURES

LIST OF TABLES

NOMENCLATURE

δ	Variational operator
ϵ	Reduction of bending amplitude
ρ	Mass density, fluid density
$\rho\mathbf{A}$	Conductor mass per unit length
$\rho\mathbf{A}_{\mathrm{ml}}$	Mass per unit length of the left messenger
$\rho\mathbf{A}_{\mathrm{mr}}$	Mass per unit length of the right messenger
γ	Loop length
$\rho\mathbf{A}_{\mathrm{m}}$	Mass per unit length of the messenger
$[\mathbf{K}]$	Stiffness matrix of the conductor
$[\mathbf{K}_{\mathrm{d}}]$	Stiffness matrix of the damper
$[\mathbf{K}_{\mathrm{T}}]$	Stiffness matrix of the conductor due to axial tension
$[\mathbf{M}]$	Mass matrix of the conductor
$[\mathbf{M}_{\mathrm{d}}]$	Mass matrix of the damper
$\overline{\mathbf{Y}_{\mathrm{l}}}$	Peak-to-peak normalized vertical displacement of the left node
$\overline{\mathbf{Y}_{\mathrm{maxd}}}$	Maximum peak-to-peak normalized displacement of a damped case
$\overline{\mathbf{Y}_{\mathrm{maxu}}}$	Maximum peak-to-peak normalized displacement of an undamped case
$\overline{\mathbf{Y}_{\mathrm{max}}}$	Peak-to-peak normalized vertical displacement of the node with maximum displacement
$\overline{\mathbf{Y}_{\mathrm{mid}}}$	Peak-to-peak normalized vertical displacement of the mid span node
$\overline{\mathbf{Y}_{\mathrm{r}}}$	Peak-to-peak normalized vertical displacement of the right node
$\{\mathbf{F}\}$	Force vector of the conductor
$\{\mathbf{F}_{\mathrm{g}}\}$	Force vector of the gravitational forces
$\mathbf{C}_{\mathrm{L}}$	Lift coefficient

$\mathbf{c_S}$ Strouhal number

$\mathbf{D}$ Conductor diameter

$\mathbf{EI_m}$ Messenger flexural rigidity

$\mathbf{EI_{ml}}$ Flexural rigidity of the left messenger

$\mathbf{EI_{mr}}$ Flexural rigidity of the right messenger

$\mathbf{EI}$ Conductor flexural rigidity

$\mathbf{F_L}$ Lift force

$\mathbf{f_{vs}}$ Vortex-shredding frequency

$\mathbf{f}$ Forcing frequency

$\mathbf{h}$ Height of the clamp of the messenger

$\mathbf{J_{dl}}$ Moment of inertia of the left counterweight

$\mathbf{J_{dr}}$ Moment of inertia of the right counterweight

$\mathbf{L_c}$ Length at which the damper is placed in the conductor

$\mathbf{L_l}$ Left messenger length

$\mathbf{L_r}$ Right messenger length

$\mathbf{L}$ Conductor span length

$\mathbf{m_c}$ Conductor mass

$\mathbf{m_l}$ Left counterweight mass of the damper

$\mathbf{m_r}$ Right counterweight mass of the damper

$\mathbf{N_c}$ Conductor shape functions

$\mathbf{N_l}$ Left messenger shape functions

$\mathbf{N_r}$ Right messenger shape functions

$\mathbf{P_C}$ Power dissipated by the conductor

$\mathbf{P_D}$ Power dissipated by the damper

$\mathbf{P_W}$ Wind power input

$\mathbf{P}$ Wave period

$\mathbf{T}$ Total kinetic energy, axial tension on the conductor

$\mathbf{T_c}$ Kinetic energy of the conductor

$\mathbf{T_{dl}}$ Kinetic energy of the left counterweight

$\mathbf{T_{dr}}$ Kinetic energy of the right counterweight

$\mathbf{T_{ml}}$ Kinetic energy of the left messenger

$\mathbf{T}_{mr}$ Kinetic energy of the right messenger

$\mathbf{V}$ Total potential energy

$\mathbf{V}_{c}$ Potential energy of the conductor

$\mathbf{V}_{dl}$ Potential energy of the left counterweight

$\mathbf{V}_{dr}$ Potential energy of the right counterweight

$\mathbf{V}_{ml}$ Potential energy of the left messenger

$\mathbf{V}_{mr}$ Potential energy of the right messenger

$\mathbf{v}$ Wind velocity

$\mathbf{w}_{c}$ Generalized coordinates of the conductor element

$\mathbf{w}_{l}$ Generalized coordinates of the left messenger

$\mathbf{w}_{r}$ Generalized coordinates of the right messenger

$\mathbf{W}_{g}$ Work of the gravitational forces of the damper

$\mathbf{W}_{nc}$ Work of the non-conservative forces

$\mathbf{Y}_{l}$ Normalized vertical displacement of the left node

$\mathbf{y}_{l}$ Vertical displacement of the left node

$\mathbf{Y}_{max}$ Normalized vertical displacement of the node with maximum displacement

$\mathbf{y}_{max}$ Vertical displacement of the node with maximum displacement

$\mathbf{Y}_{mid}$ Normalized vertical displacement of the mid span node

$\mathbf{y}_{mid}$ Vertical displacement of the mid span node

$\mathbf{Y}_{r}$ Normalized vertical displacement of the right node

$\mathbf{y}_{r}$ Vertical displacement of the right node

CHAPTER 1

INTRODUCTION

1.1 Motivation

The study of conductor behaviour is not a recent one. [Claren and Diana, 1969] and [Diana and Falco, 1971] conducted studies to initiate the understanding of the performance of a transmission line.

These types of studies served as basis for several consequent analysis, many of which serve the same purpose: the understanding of the behaviour of a conductor due to aeolian vibration and to find the solution on how to reduce it. Aeolian vibration is the main cause of fatigue failure on conductors.

One of the most evident examples of this type of failure is the infamous 2002 Brazil ACSR conductor failure, which lead to almost 67 million Brazilians be in complete blackout [Azevedo and Cescon, 2002]. The failure of the ACSR conductor, due to various dynamic and static solicitations, lead to the breakage of several conductor strands, as depicted in Figure 1.1.

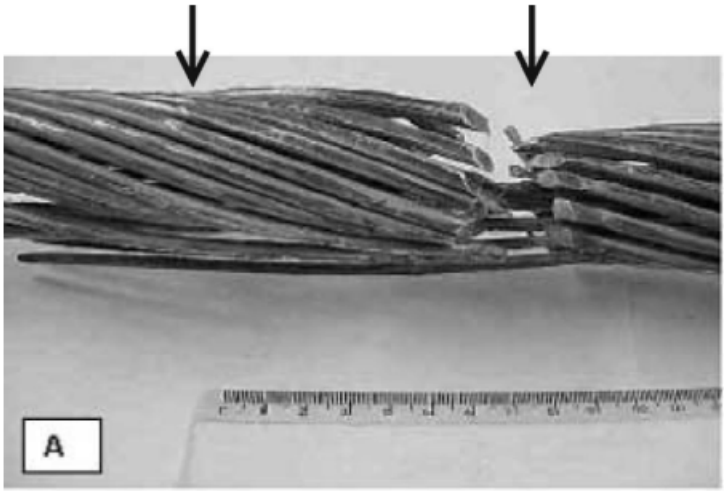

Figure 1.1: Conductor with broken strands, retrieved from [Azevedo and Cescon, 2002].

In order to reduce the values of conductor displacement, in 1925 George H. Stockbridge developed the Stockbridge damper, which consists of a mechanical system with two counterweights positioned at the extremities of a large stranded cable know as the messenger wire. This mechanical system is clamped to the conductor and aims to reduce the conductor vibration by the vibration of the damper's counterweights and also by the hysteretic damping of the messenger strands.

Many studies were done to understand the behaviour of the Stockbridge damper and one conclusion is common between various authors: the performance of the damper is heavily non-linear [Barbieri and Barbieri, 2012].

The main method to study the conductor displacement when dampers are attached is the Energy Balance Method [Hagedorn, 1982]. This method produces fair estimations of the displacement of the conductor, besides the fact of making a several number of simplifications. This method is also heavily characterized by the dependance of a high number of empirical values, leading to every case of a mechanical system of a conductor with a damper attached to be somewhat unique.

The process of obtaining the optimal solution and increasing damper efficiency, with the present solutions, can become a heavy process of trial and error. Therefore, the study of new ways of predicting the conductor's behaviour with and without Stockbridge dampers is of great importance to effectively reduce the process of trial and error, have the ability to achieve the optimal solution and consequently avoid fatigue failure on transmission lines. New procedures based on the finite element method have been referred in recent years for studying the conductor and the conductor-Stockbridge damper vibration behaviour [Barry, 2010].

1.2 Objectives

This dissertation work aims to analyse the transmission lines aeolian vibration without and with external damping devices like the commonly used Stockbridge dampers.

To attain this main objective, complementary objectives are also fixed for this dissertation work. The most noteworthy are:

- development of a FEM based model for the conductor and for the conductor with Stockbridge dampers considering the Euler-Bernoulli theory of beams under axial tension;
- implementation of the FEM model in a Matlab environment to calculate the modal parameters as well as the forced response induced by the aeolian excitation;
- perform a parametric analysis in order to acquire insight about the influence of parameters like axial tension, damper properties, damper configuration and damper location on the global dynamic behaviour of the conductor-damper system;
- extract some guidelines for the design of devices to passively control the aeolian vibration of transmission lines.

1.3 Thesis overview

This work is divided into six main chapters. This present chapter introduces the problem and shows the work objectives. Chapter 2 and Chapter 3 contain the literature review and all the mathematical formulations and consequent finite element modeling, respectively.

The validation of the model is done in Chapter 4 according to the works of [Barbieri et al., 2004] and through a comparison of data with simulations done with *Ansys*. The Matlab program workflow and variable overview is also presented in this chapter.

Chapter 5 presents the majority of the simulations done, as well as the parametric analysis for an ACSR conductor.

Finally, Chapter 6 presents the conclusions of this work as well as the proposed future works.

CHAPTER 2

THEORETICAL INTRODUCTION AND PREVIOUS WORKS

As previously stated, the interest of this work is to gain a better understanding of transmission line aeolian vibration and to find a more efficient way to implement damping through the instalation of Stockbridge dampers. These types of dampers are very commonly used and can vary its properties, depending on the work conditions that the conductor has.

This chapter aims to expose the majority of relevant studies done in this field.

2.1 Transmission lines

Aeolian vibration stands as a threat to the life-span of undamped transmission lines, leading in many cases to fatigue failure in the clamps and broken strands. These type of failures cannot only cost a great amount of money to repair, but most of all it can threaten human life [Barry, 2010].

The conductor (or transmission line) is, on a construction standpoint, a group of several strands structured in helix shaped layers. These can have a wide range of materials, such as [Barry, 2010]:

- Aluminum conductor steel reinforced (ACSR - known for its high tensile-strength-to-weight ratio, due to the reinforcement with steel in the inner layers). This is the most common material seen on transmission lines;
- All aluminum conductor (AAC - with 99.5% aluminum purity);
- All aluminum alloy conductor (AAAC - made from an aluminum-magnesium-silicon alloy, presenting itself with good corrosion resistance and strength-to-weight-ratio).

A cross-section view of an ACSR conductor can be seen in Figure 2.1.

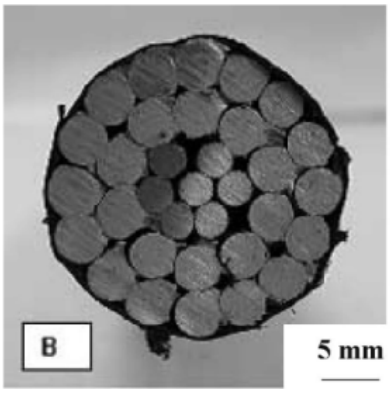

Figure 2.1: Cross-section view of an ACSR conductor, retrieved from [Azevedo and Cescon, 2002].

A schematical representation of a normal placement of a conductor between two electrical towers can be seen in Figure 2.2.

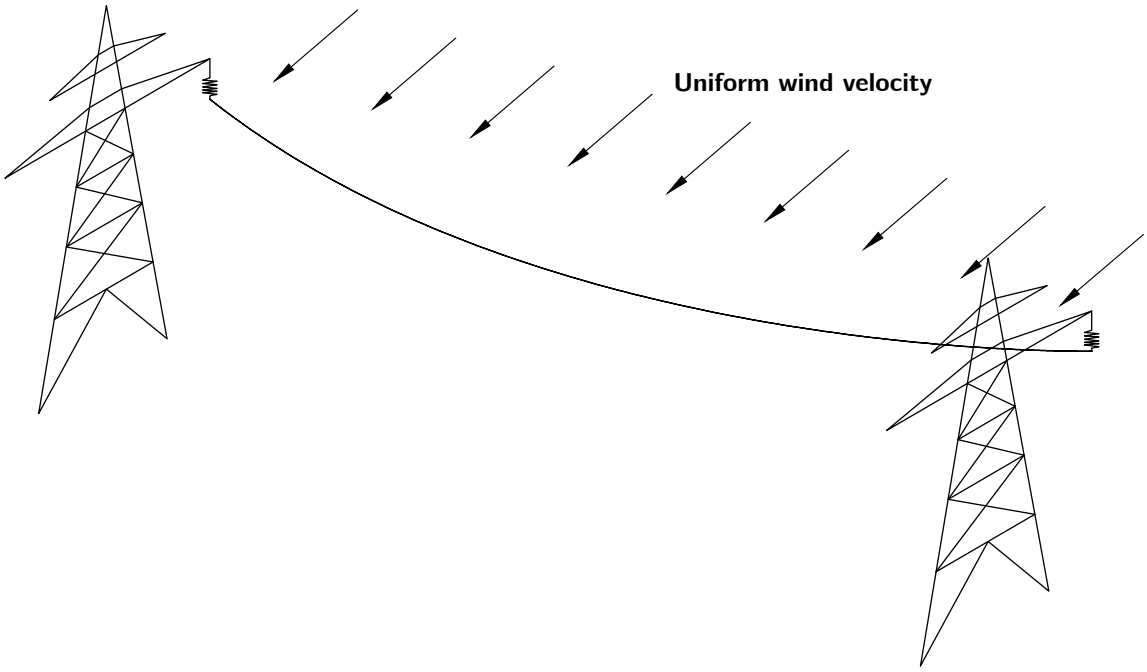

Figure 2.2: An example of a conductor, strung between two electrical towers, adapted from [Vecchiarelli, 1997].

It is important to note that due to its configuration of a set of layered strands in helix shape, the conductor itself presents a form of self-damping, known as hysteretic damping, which consists on the friction between the strands caused by the movement of the conductor.

[Nawrocki and Labrosse, 2000] conducted a study to create a finite element model to determine the slippage and the distribution of tension on the various strands. The study showed that if slippage occurs, the probability of existing friction between the strands and consequently self-damping, reduces.

When a mathematical formulation of the conductor is achieved, there must be a factor in its equation of motion that accounts for the influence of the axial tension on the conductor. When formulating a Finite Element for these types of conductors, the influence of the axial tension comes as an additional "secondary" stiffness matrix to be added to the "original" stiffness matrix [Barry, 2010]. The manipulation of said "secondary" matrix can determine the influence that the axial tension at

which the conductor is strung has to the behaviour of the conductor.

That value of tension is always a certain percentage of the Rated Tensile Strength (RTS) and is considered as a limit of axial tension to which the conductor should be subjected. A rule of thumb determines the conductor to be strung at between 20 to 25 % of its RTS. From that point on out, the probability of fatigue failure on the clamps or breakage of the strands is increased.

Many mathematical formulations for the equation of motion of a transmission line due to wind vibration were achieved throughout the years. Starting by the earlier work of [Claren and Diana, 1969] and more recently the works of [Barry, 2010; Vecchiarelli et al., 2000; Wang et al., 1997], a general equation of motion of a transmission line can be represented as,

$$EI\frac{\partial^4 y}{\partial x^4} - T\frac{\partial^2 y}{\partial x^2} + \rho A\frac{\partial^2 y}{\partial t^2} = \sum_{i=1}^{n} p_i \delta(x - xi). \tag{2.1}$$

In the above mathematical formulation defined by [Wang et al., 1997] y represents the vertical displacement of the conductor at a distance x from one of the two extremities, EI is the bending stiffness of the cable, T is the axial tension at which the conductor is strung, ρA is the mass per unit length of the conductor and p_i is a function of frequency that translates into the force exerted by the i^{th} damper on the conductor.

Considering an arbitrary vibration of the conductor, as seen in Figure 2.3, the loop length γ represents essentially half of the wavelength of the conductor vibration, the node is the point where the vertical displacement is null and the antinode is the point of the conductor at which the displacement is maximum.

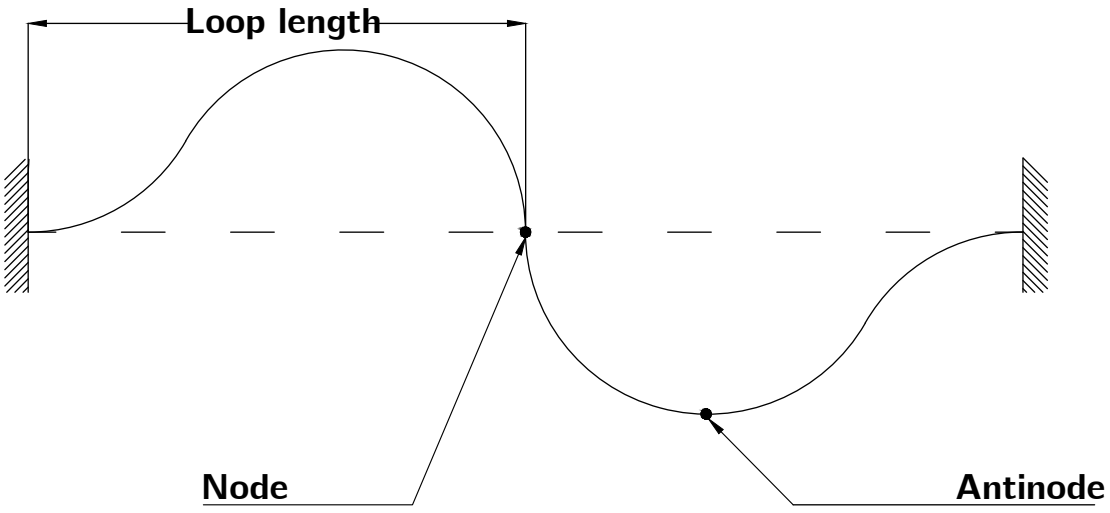

Figure 2.3: An example of a conductor vibration.

Regarding the actual vibration of the conductor, it is assumed that the amplitude of vibration is mostly inferior in value when in comparison with the conductor diameter. [Meynen et al., 2005] stated that damping is required when the amplitude, usually represented as $X(\omega)$, is lower than $0.7D$, where D represents the diameter of the conductor. From that point on out the conductor starts to give back energy received from the wind, acting as a form of self-damping. This type of behaviour is also backed up by [Richardson, 1996], where calculations were done and compared to experimental values. The results were presented in a *wind energy vs. wind speed* graph form where two types of information were compared:

- Wind energy input;
- Conductor energy loss.

Figure 2.4 demonstrates a schematic representation of the graph as seen in [Richardson, 1996]:

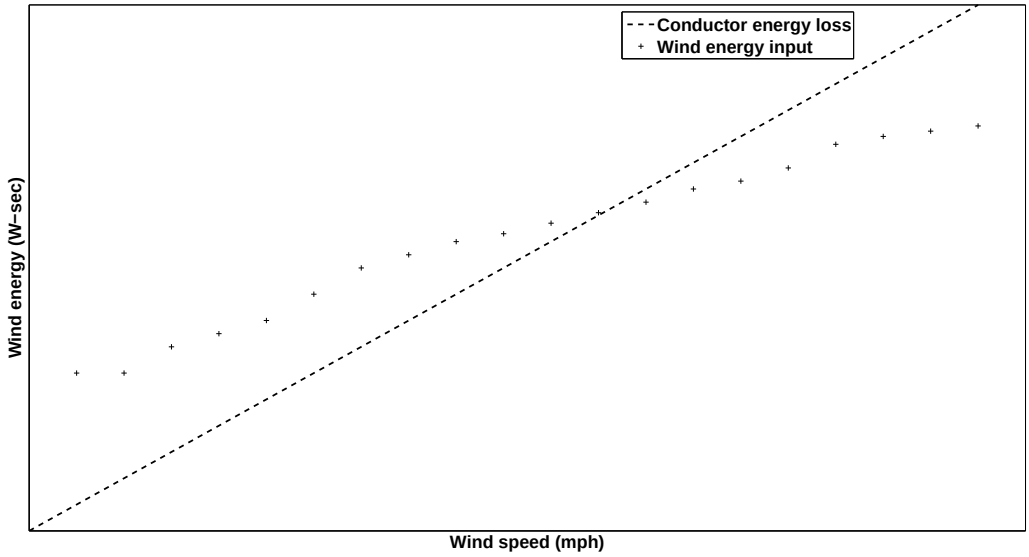

Figure 2.4: Schematic representation of *wind energy vs. wind speed*, adapted from [Richardson, 1996].

The point of intersection between the two curves was designated the "critical wind speed". It is then visible that below that critical point, the use of dampers was required, where the difference between the two curves would be the amount of damping needed. On the other hand, above the critical wind speed damping was not required because, as mentioned before, the conductor was giving back energy, resulting in a form of damping.

[Barbieri et al., 2004] presented a complex study of the dynamics of transmission lines, having experimental results compared to analytical results. In the first two parts of the study the author achieved a Finite Element formulation for the conductor and was able to have good agreement between experimental results and analytical solutions. Throughout the work three procedures were used (interpolation of a fourth order equation, auxiliary modal damping matrix and an iterative procedure) in order to achieve a formulation of an equivalent viscous damping matrix of the form:

$$[C] = \alpha[M] + \beta[K], \tag{2.2}$$

where [C] is the damping matrix, [M] the mass matrix and [K] the stiffness matrix. The last two matrices are multiplied by the two influence factors α and β, respectively.

This part of the study also proved that the damping ratio increases with the increase of the span length and decreases with the increase of the mechanical load applied. The final part of the work studied the nonlinear characteristics of the large amplitude free vibrations of noninclined and inclined elastic cables, numerically and experimentally, proving that with cables with larger sag, variations can be noticed in the first natural frequencies, when comparing the linear and non-linear results (heavily dependent on the sag and the applied load). It was also proved that the addition of a concentrated mass in the cable alters the dynamic behaviour with modal uncoupling, presenting the same behaviour as an inclined cable. Finally, variations of the cable load or increasing the central sag of the cable would effectively change the natural frequencies.

Some previous works, like the one by [Vecchiarelli et al., 2000], reference the existence of a *lock-in phenomenon* where the frequency of vortex-shredding, or f_{vs}, is almost or equal to f_n, which represents

one of the natural frequencies of the conductor. This type of phenomenon leads to a significant level of vibration on the conductor.

[Meynen et al., 2005] also accounted for this phenomenon when integrating numerically the Navier-Stokes equations. The authors considered that the *lock-in phenomenom* was present throughout the entirety of the wind speed range, which is comprehended between 1-7 m/s. This is given due to the fact that almost every frequency is a natural frequency in that given range.

The previously mentioned works have taken an approach where the wind excitation is considered uniformly distributed throughout the entirety of the conductor. However, [Diana et al., 1993] were able to create an analytical approach to turbulence conditions of aeolian vibration, leading to the creation of a model of a conductor by finite elements, to reproduce the mass and stiffness characteristics of the cable and introduce turbulence models to generate a space and time history of the wind, with the final objective of obtaining an appropriate wind speed and direction model.

The representation of the non-uniformity of the wind excitation can be seen in Figure 2.5.

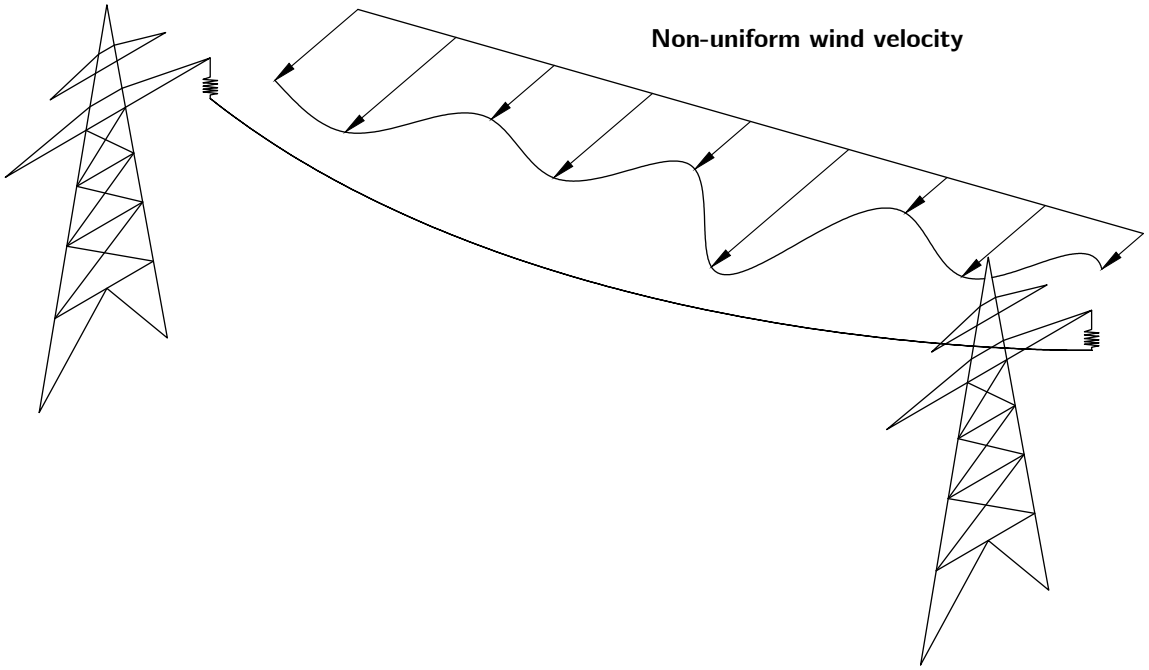

Figure 2.5: An example of a conductor, strung between two electrical towers, subjected to a non-uniform wind excitation.

This was created in order to simulate the existence of a more realistic wind excitation. Its numerical approach proved to be successful, achieving a good approximation between the experimental and numerical values.

2.2 Wind excitation modeling

Aeolian vibration occurs due to vortex-shredding, resulting from the flow of the wind through the conductor. The various regimes of flows can be determined by the Reynolds number, that can be calculated as:

$$R_e = \frac{vD}{\nu}, \tag{2.3}$$

in which D represents the conductor diameter, v the wind velocity and ν the kinematic viscosity of the fluid. The various flow regimes can be seen in Figure 2.6.

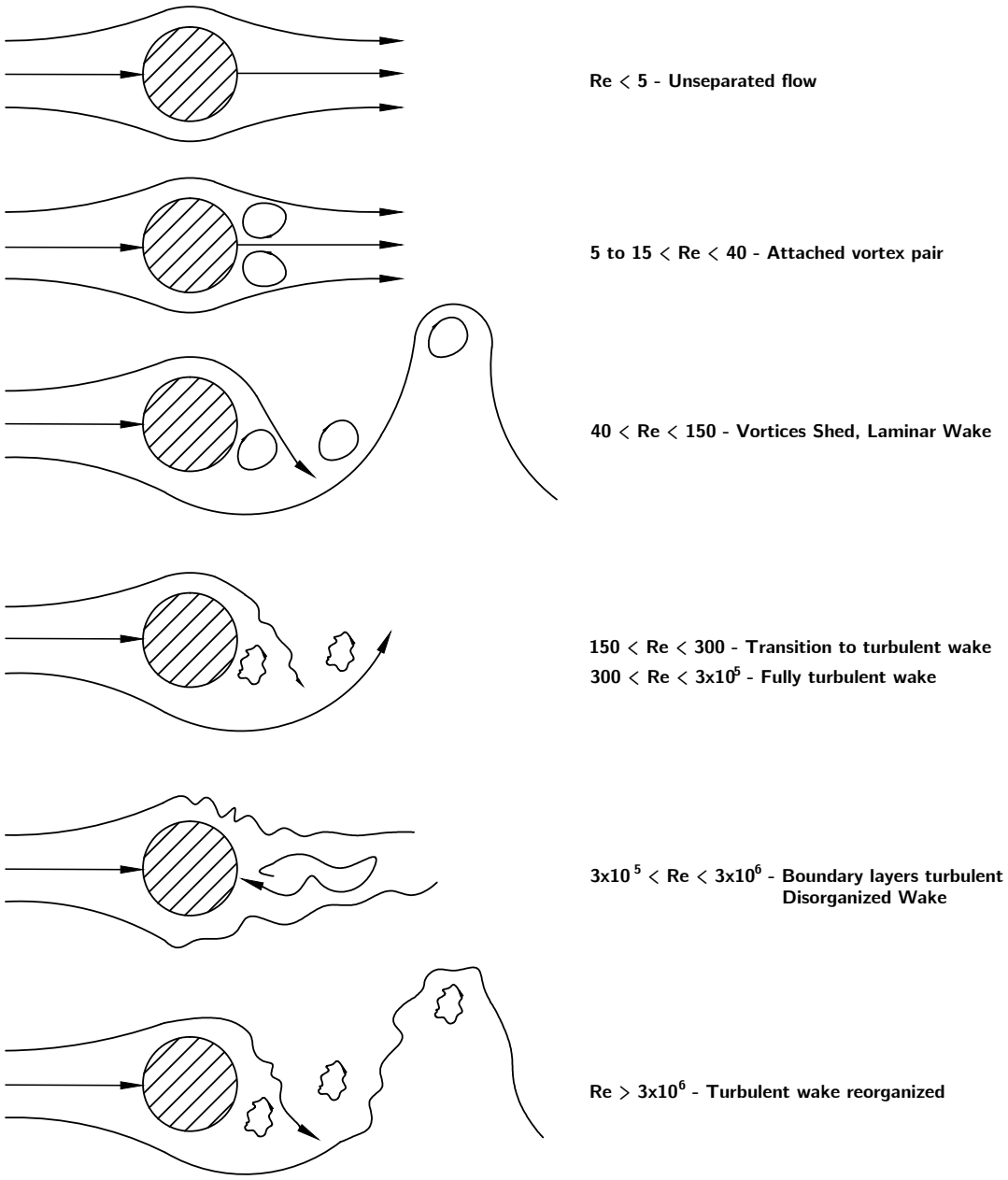

Figure 2.6: Schematical representation of the various flow regimes, adapted from [Vecchiarelli, 1997] and [Lienhard, 1966].

As stated previously, aeolian vibration is caused due to vortex-shredding, which generates alternating forces that act fundamentally in the transverse direction of the flow (lift force).

The frequencies of the vortex-shredding can be calculated through the following relation:

$$f_{vs} = \frac{c_S V}{D}, \tag{2.4}$$

where c_S is the Strouhal number, v is the wind velocity and D is the conductor diameter. An usual value for c_S is about 0.2, regarding aeolian vibration.

A study from [Diana and Falco, 1971] concluded that the lift force that acts during the vibration

of the conductor (considered as a rigid cylinder in a uniform flow) is virtually harmonic in time, as well as the conductor displacement, when in steady-state.

The magnitude of the lift force can be calculated as:

$$F_L = \frac{1}{2} C_L \rho D L v^2, \tag{2.5}$$

where C_L represents the lift coefficient, ρ is the density of the fluid, D is the conductor diameter, L is the span length of the conductor and v is the wind velocity. According to a study by [Griffin and Koopmann, 1977] a maximum lift coefficient of 0.55 was measured on a cylinder which showed a maximum normalized vibration of $0.55D$, peak-to-peak. The cylinders with maximum vibration amplitudes above and below the value experienced lift coefficients between the values of 0.28 and 0.33.

2.3 Stockbridge dampers

Developed by George H. Stockbridge in 1925, the Stockbridge damper is mainly comprised of a clamp, a messenger cable that spans to both sides and also 2 counterweights positioned at each extremity of the messenger cable. The main purpose of the damper is to reduce aeolian vibration on the transmission lines through the vibration of the damper's own counterweights. There is also damping in the messenger cables due to the friction between the strands.

The dampers are usually placed near the span ends, as exemplified in Figure 2.7, between 0.5 to 5 m from the clamp, as proposed by [Vecchiarelli, 1997]. Normally one or two are used, although some cases require an existence of bundled conductors, as mentioned by [Lu and Chan, 2007].

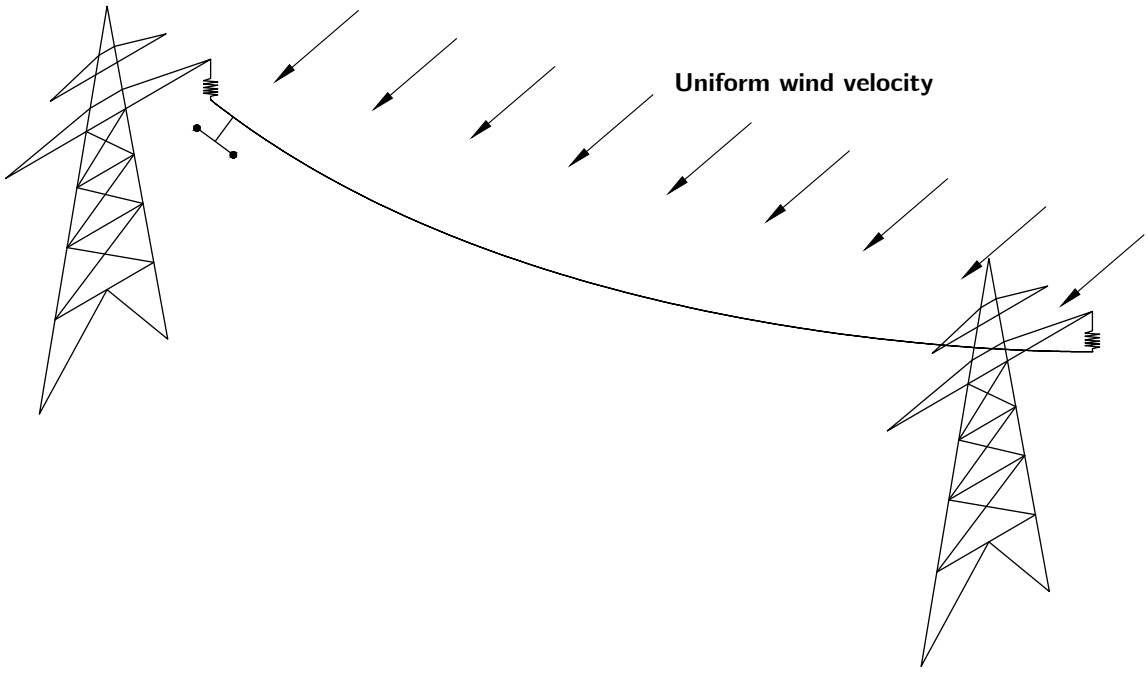

Figure 2.7: An example of a Stockbridge damper attached to a conductor, adapted from [Vecchiarelli, 1997].

Commonly, Stockbridge dampers have the following configuration, as shown by Figure 2.8.

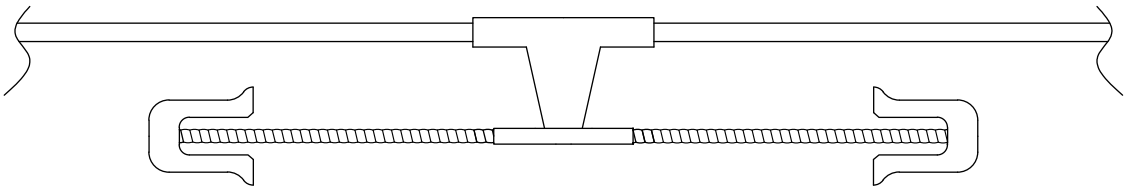

Figure 2.8: An example of a Stockbridge damper attached to a conductor.

Regarding the counterweights, they can be symmetrical or asymmetrical, resulting in different behaviours when excited. Earlier work done by [Wagner et al., 1973] helped to initiate the understanding of the dynamics of a Stockbridge damper. Using a simplified mechanical version of the damper due to its symmetry, [Wagner et al., 1973] were able to determine that a Stockbridge damper is a system with 4 degrees of freedom: two rotational and two translational vibrations at each tip mass.

Using only half of the damper and using a simplified version as seen in Figures 2.9a and 2.9b:

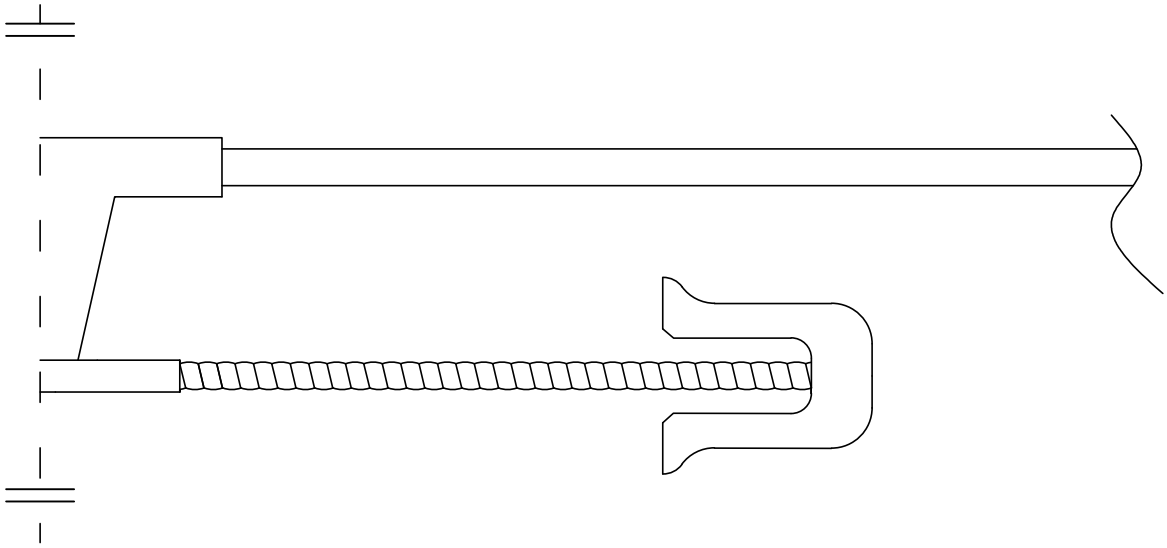

(a) Representation of one half of a Stockbridge damper.

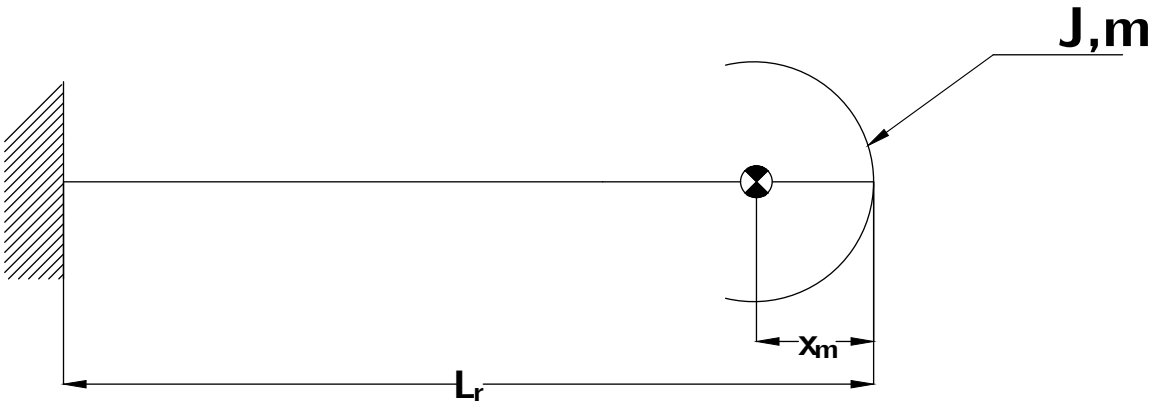

(b) Simplified free-body diagram representation of one half of the Stockbridge damper.

Figure 2.9: Representation and model of half of a Stockbridge damper.

[Wagner et al., 1973] used a free-body diagram similar to the one shown in Figure 2.9b, where L_r

is considered the length of the messenger, sub-index r for right and l for left, the same for the mass of each counterweight m and for the moment of inertia J. The variable x_m represents the position of the center of mass of each of the counterweights.

The author considered the entire messenger length as massless and established the following mass and stiffness matrices:

$$[M] = \begin{bmatrix} m & mx_m \\ mx_m & J \end{bmatrix}; \qquad [K] = \begin{bmatrix} k & 2kL_r \\ 2kL_r & \frac{4kL_r^3}{3} \end{bmatrix}, \tag{2.6}$$

where k represents the stiffness coefficient of the messenger cable. The damping matrix was considered as a multiplication of a certain constant μ with the stiffness matrix. The purpose of the work was to create a theoretical analysis of the damper in order to predict its behaviour. The author determined that the equivalent bending stiffness of the messenger was low due to the fact of the slippage of the rods that are part of the messenger cable.

Many studies were done for Stockbridge dampers, regarding various types of behaviours. There is a common agreement among various authors: that the performance of the Stockbridge damper is nonlinear, depending not only of the frequency of excitation but also of the amplitude.

[Kalombo et al., 2012] performed experimental tests on Stockbridge dampers and compared the values with a mathematical model as presented by [Wagner et al., 1973], confirming the existence of two resonances. However, due to the friction between the wires, the stiffness and non-homogeneity of the Stockbridge damper messenger cable, it lead to a significant gap between the experimental and numerical values after the first mode of vibration.

[Guedes et al., 2005] conducted experimental tests to a damper at various velocity amplitudes and were able to obtain curves of force and moment, mechanical impedance and power absorbed by the damper as functions of frequency, proving the heavy nonlinear behaviour of the damper. As the clamp velocity increased, the damper's natural frequencies decreased, the force exerted and power absorbed increased (the power is directly proportional to the increase in velocity). However, as the velocity of the clamp increases, the frequency bands at which the damper acts efficiently become narrower. Independent of the velocity amplitude is the location of the maximum value of force exerted which always remains at the second mode of vibration.

In order to investigate the linear and nonlinear dynamical performance of the damper, [Barbieri and Barbieri, 2012] performed experimental tests with varying excitation frequencies and measured the loss factor and Young's modulus with data adjustment from linear and nonlinear models. What was stated in [Guedes et al., 2005] was confirmed in this study, where when the amplitude of motion is higher, the natural frequencies lower in value.

The study also showed that the damping ratio of the system decreases as the motion amplitude decreases, as well as both the real and imaginary parts of the Young's modulus.

[Lara-Lopez and Colin-Venegas, 2001] studied the endurance of the damper by calculating the stress at the center rod of the messenger (at the end, where it connects to the counterweight). The damper's life is calculated at the maximum stress condition. The study proved that the life of the damper is highly sensitive to the amplitude of excitation of the damper, where for a high number of cycles (N) comprehended between 10^5 to 10^6, the amplitude of excitation is comprehended between 5.96 and 6.36 mm, where for low life cycles ($N < 10^5$) the interval of amplitude is between 6.36 and 7.45 mm.

The previous study is one of many to try and reduce the process of trial and error when designing Stockbridge dampers. The study of [Sauter and Hagedorn, 2002] used a single Jenkin element to model the damper cable in order to simulate the impedances based on data retrieved from an experiment with a singular damper cable, obtaining good results, although the method needed improvement in the neighbourhood of the second resonance.

[Krispin, 2007] studied the optimization of the damper clamp in order to obtain a more favorable damping performance. The author proved that using lightweight clamps, designed specifically for attachments by means of helical factory formed rods, instead of the conventionally used bolted clamps (larger mass), would result in a significant gain in damping performance.

2.4 The Energy Balance Method (EBM)

One of the methods to determine the conductor's behaviour due to aeolian vibration is the Energy Balance Method (EBM). The method is based upon the balance of the following simple equation,

$$P_W = P_D + P_C\,, \tag{2.7}$$

where P_W is the wind power input (or the power of aerodynamical forces), P_D is the power dissipated by the damper and P_C is the power dissipated by the conductor. The methods to obtain the power expressions and the strain values are retrieved from the works of [Hagedorn, 1980], [Hagedorn, 1982] and [Wolf et al., 2010].

2.4.1 Power of the aerodynamical forces

The power input from the wind can be calculated as [Wolf et al., 2010]:

$$P_W = L f_{vs}^3 D^4 f nc\left(\frac{A}{D}\right), \tag{2.8}$$

which is heavily dependent on the frequency of vortex-shredding f_{vs}, presented in equation (2.4), which itself depends on the Strouhal coefficient, largely considered by many authors to be approximately 0.2. The power input also depends on the reduced power function, represented by $f nc\left(\frac{A}{D}\right)$ in equation (2.8), also known as the function of relative vibration amplitude $\frac{A}{D}$, being A the vibration amplitude of the conductor.

This function has had various interpretations throughout the years, that can be presented as an experimental curve, measured at an ideal laminar flow. The work of [Diana and Falco, 1971] is one of the earliest studies of this type of behaviour.

2.4.2 Power dissipated by the conductor

The conductor itself, as stated previously, has the capacity to dissipate power through the friction between the strands that are part of the conductor. The value of the dissipated power can be given as [Wolf et al., 2010]:

$$P_C = L K \frac{(A/D)^l f^m}{T^n}, \tag{2.9}$$

where K is a proportionality factor which characterizes the self-damping properties of the cable and l, m and n are exponents of amplitude, frequency and cable tension, respectively, which should be equal for all cables. These types of values are of empirical nature and in Table 2.1 is a gathering of values from various authors who determined them through experimental procedures. Two types of methods were used, the Inverse Standing Wave Method (ISWR) and the Power Method (PT).

Table 2.1: Common exponent values from various authors, adapted from [Wolf et al., 2010].

Authors	l	m	n	Length (m)	Method
Tompkins et al.	2.30	5.00	1.90	36	ISWR
Claren & Diana	2.00	4.00	2.50	46	PT
Seppä	2.50	5.75	2.80	36	ISWR
Kraus & Hagedorn	2.47	5.38	2.80	30	PT
Noiseux	2.44	5.63	2.76	63	ISWR
Möcks & Schmidt	2.45	5.38	2.40	30	PT
Politecnico di Milano	2.43	5.50	2.00	46	ISWR
Rawlins	2.20	5.40	1.00	36	ISWR

2.4.3 Power dissipated by the damper

In order to obtain the power dissipated by the conductor it is necessary to know the impedance of the damper, which is essentially knowing the behaviour of the damper when excited, and at what range of frequencies the damper is efficient. The impedance of a damper is then considered as the transfer function connecting the velocity amplitude of the damper clamp and the force acting on it.

Studies such as the one by [Hagedorn, 1982] state that to properly know the dynamical properties of a Stockbridge damper it is necessary to consider the translational as well as the rotational motion, given the fact that they co-exist in real life applications. The author then proceeded to identify a 2×2 impedance matrix, resultant of the simplification of the damper to a system with two degrees of freedom, for one half of the damper.

As stated previously, the Stockbridge has a strongly nonlinear behaviour, depending on both the frequency of excitation and the amplitude, which makes the process of obtaining a trustworthy model of its behaviour a more complex procedure. The power dissipated by the damper can be given as [Hagedorn, 1982; Wolf et al., 2010],

$$P_D = \frac{1}{4} T c k^2 \frac{1-(h^2+g^2)}{1+h^2+g^2} D^2 \left(\frac{A}{D}\right)^2, \tag{2.10}$$

where the various variables present in equation (2.10) and their related variables can be calculated as:

$$h = -\frac{\sin^2 k l_1 (\sin 2k l_1 + 2\gamma \sin\alpha)}{\sin^2 k l_1 + \gamma^2 + 2\gamma \sin k l_1 \sin(k l_1 + \alpha)}, \tag{2.11}$$

$$g = \frac{\sin^2 k l_1 \cos 2k l_1 + \gamma^2 + \gamma \sin 2k l_1 \sin\alpha}{\sin^2 k l_1 + \gamma^2 + 2\gamma \sin k l_1 \sin(k l_1 + \alpha)}, \tag{2.12}$$

$$k = 2\pi f \sqrt{\frac{m_L}{T}}, \tag{2.13}$$

$$c = \sqrt{\frac{T}{m_L}}, \tag{2.14}$$

$$\gamma = \frac{T}{Zc}. \tag{2.15}$$

The variable k is the wave number associated to the excitation, c is the wave velocity, T is the axial tension at which the conductor is strung, Z is the magnitude value of the impedance at each excitation frequency, α is the phase value of the impedance, m_L is the mass per unit of length of

the conductor, f is the frequency of excitation and l_1 is the position at which the damper is placed throughout the conductor.

Works such as the one by [Verma and Hagedorn, 2005] were able to adapt the EBM to include the calculation of warning spheres, use the adapted method to estimate values of aeolian vibration and calculate bending stresses in critical sections of the conductor.

2.4.4 EBM assumptions

Given all the equations to calculate each of the power inputs, equation (2.7) is computed to obtain A or $\frac{A}{D}$ for various values of excitation frequency. The process is known to not be very computationally heavy, which can give useful results when trying to predict the conductor behaviour, regardless of the fact that the method is subjected to some considerable simplifications.

The method can be characterized by the following [Vecchiarelli, 1997]:

- Ignores the flexural rigidity of the conductor;
- Considers a wind velocity for which lock-in occurs at one of the conductor's natural frequencies of vibration;
- For a steady-state condition, assumes that the conductor vibrates in a standing wave and in the mode corresponding to the lock-in frequency;
- Hypothesizes that the conductor is composed of infinitesimal rigid cylinders which absorb wind power according to their displacement amplitudes;
- Integrates the wind power input per unit length over the span of the conductor to determine the total wind power input in terms of the antinodal displacement amplitude;
- Expresses the total power dissipated through damping as a function of the antinodal displacement amplitude;
- Calculates the antinodal displacement amplitude at which the total wind power input is equal to the total power dissipation.

2.4.5 Strain calculation

Even though the flexural rigidity of the cable is not accounted for in the EBM, it is necessary to know its value (or the range at which it fluctuates) to determine the values of the strain on certain conductor sections. The general expression for the bending strain can be given as the following expression, dependent of the vertical displacement u [Hagedorn, 1982],

$$\varepsilon(x,t) = \frac{d}{2} y''(x,t), \tag{2.16}$$

where d stands as the bending diameter, which is different from the conductor diameter and can be determined as,

$$d = K_s D, \tag{2.17}$$

being K_s a slippage coefficient (to be determined empirically) resultant of the relative displacement between the strands of the conductor.

The cable strain at a section far away from the clamps can be given as [Hagedorn, 1980, 1982; Wolf et al., 2010],

$$\varepsilon_A = A k^2 \frac{d}{2}. \tag{2.18}$$

The strain value at the suspension clamp with a damper near is determined by,

$$\varepsilon_B = k\frac{A}{\sqrt{2(1+h^2+g^2)}}\sqrt{\frac{1+g^2+h^2}{\sin^2 kl_1}+4h\cot kl_1+2g(1-\cot^2 kl_1)}\sqrt{\frac{T}{EI}}\frac{d}{2}, \tag{2.19}$$

and at the same section but with no damper near,

$$\varepsilon_C = kA\frac{T}{EI}\frac{d}{2}. \tag{2.20}$$

It is also possible to determine the strain at the damper clamp which is presented in the equation below:

$$\varepsilon_D = \frac{d}{2}kA\sqrt{(b_1-c_1)^2+(b_2-c_2)^2}\sqrt{\frac{T}{EI}}, \tag{2.21}$$

with:

$$b_1 = -\sin kl_1 - g\cos kl_1 - h\sin kl_1, \tag{2.22}$$

$$b_2 = \cos kl_1 + g\sin kl_1 - h\cos kl_1, \tag{2.23}$$

$$c_1 = (1-g)\frac{\cos^2 kl_1}{\sin kl_1} + h\cos kl_1, \tag{2.24}$$

$$c_2 = (1+g)\cos kl_1 + h\frac{\cos^2 kl_1}{\sin kl_1}. \tag{2.25}$$

2.5 Fatigue failure in conductors

As previously mentioned, the major risk to damaging a transmission line is aeolian vibration. This type of vibration has the characteristic of having an alternating nature, leading to the cable suffering alternate bending stresses in the cable strands, increasing the chance of fretting fatigue. Fretting occurs when two contacting wire surfaces are subjected to a normal clamping force and consequently undergo a relative moment on the two surfaces [Boniardi et al., 2007].

[Vecchiarelli, 1997] stated that the bending amplitude, which determines the conductor's behaviour and risk to fatigue failure, is related to the maximum amplitude of displacement that the conductor presents for each vibration mode and can be calculated as:

$$Y_b = Y_{\max}\sin\left(0.089\frac{n\pi}{L}\right), \tag{2.26}$$

where $Y_{\max}$ is the maximum relative conductor displacement, n is the mode number and the factor of 0.089 relates to an industry standard, where the risk of fatigue failure should be calculated at 89 mm from the last point of contact between the conductor and the suspension clamp.

Figure 2.10 demonstrates a suspension clamp with a conductor attached and demonstrates the point of calculation of bending amplitude.

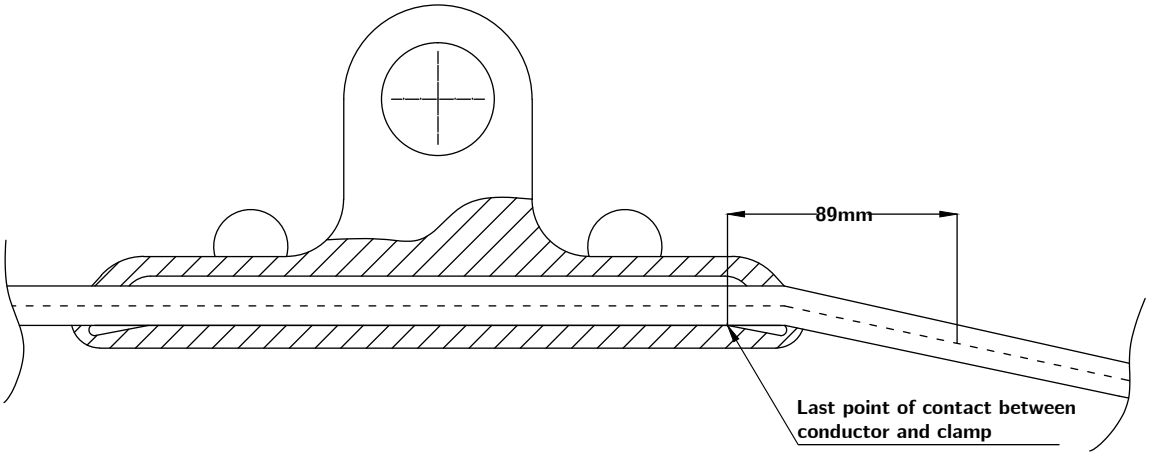

Figure 2.10: An example of a suspension clamp with a conductor attached, adapted from [Vecchiarelli, 1997].

If the value of Y_b surpasses the safe value of Y_{bsafe} (maximum value of allowed bending amplitude), which varies from conductor to conductor and from its service conditions, then the conductor is at risk of fatigue failure.

[Azevedo and Cescon, 2002] conducted a study of the infamous 2002 blackout in Brazil, resultant of fatigue failure in an ACSR conductor, which lead to nearly 67 million people be without power.

Aside from the oxidation phenomenons that were also seen in the incident, the authors concluded that the most affected region was the region nearing the clamping area, indicated by the presence of large and intense black elliptical markings, as exemplified in Figure 2.11.

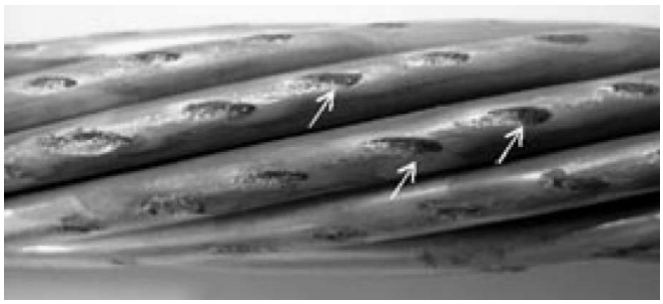

Figure 2.11: Fretting wear on the conductor, retrieved from [Azevedo and Cescon, 2002]

The fretting wear consequently promoted more fretting wear due to the creation of hard particles, aluminum oxide and oxidised silicon, that acted as an abrasive material against the aluminum strands.

These types of phenomenons can effectively be related to aeolian vibration, where it is simple to conclude that the larger the displacement of the conductor, the possibility of fretting wear consequently increases.

2.6 The EBM and FEM in the context of transmission line study

As previously stated, for many years the EBM served as the standard for predicting transmission line aeolian vibration. Due to its high dependency on empirical values and use of some parameters issued from wind tunnel experimentation associated with some limitations like the disregard of the conductor flexural rigidity, new procedures have been referred in recent years for studying the conductor and conductor-Stockbridge damper behaviour, being the work of [Barry, 2010] one of the starting works regarding the analysis of the transmission lines aeolian vibration based on the Finite Element Method.

CHAPTER 3

CONDUCTOR AND CONDUCTOR-DAMPER FINITE ELEMENT MODEL

This work tries a somewhat new approach to the study of aeolian vibration by using the finite element method (FEM). To be able to perform this type of study, both the conductor and the damper have to be formulated under the FEM approach with the purpose of implementing them into a custom designed Matlab program.

The conductor is considered as a beam under an axial tension and the Euler-Bernoulli beam theory is applied.

3.1 Conductor modeling

In order to understand and properly analyze the behaviour of a transmission line due to aeolian vibration it is necessary to determine a generic equation of motion for a beam subjected to an axial force. Figure 3.1 shows a beam element subjected to an axial force.

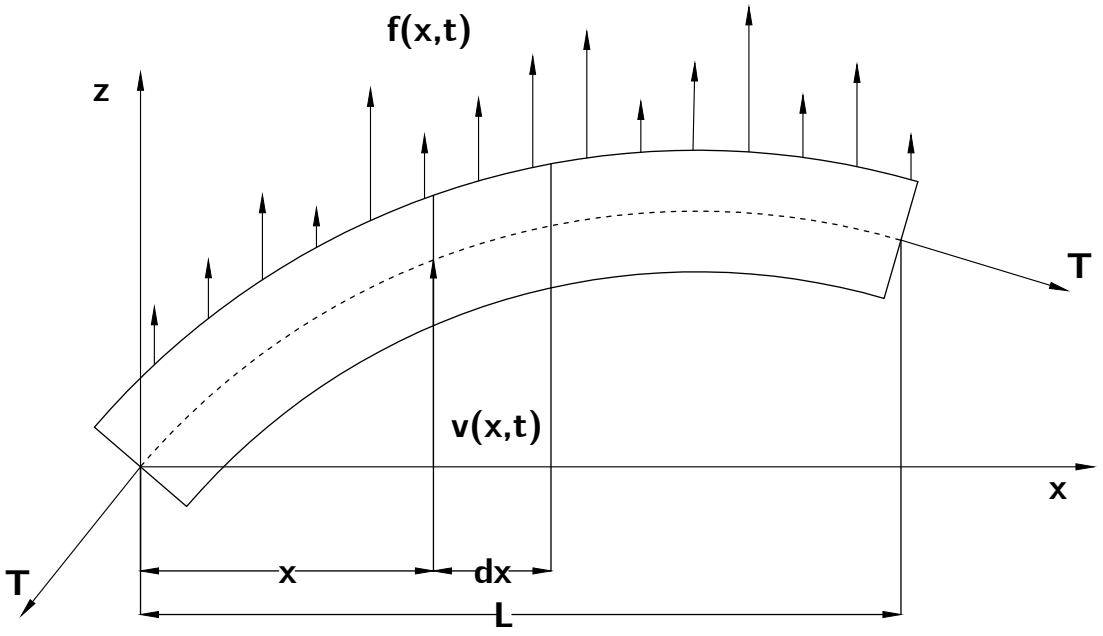

Figure 3.1: Representation of a beam element, subjected to axial force.

Highlighting a finite part of the element and presenting it in Figure 3.2 it is possible to have the present balance of forces and moments.

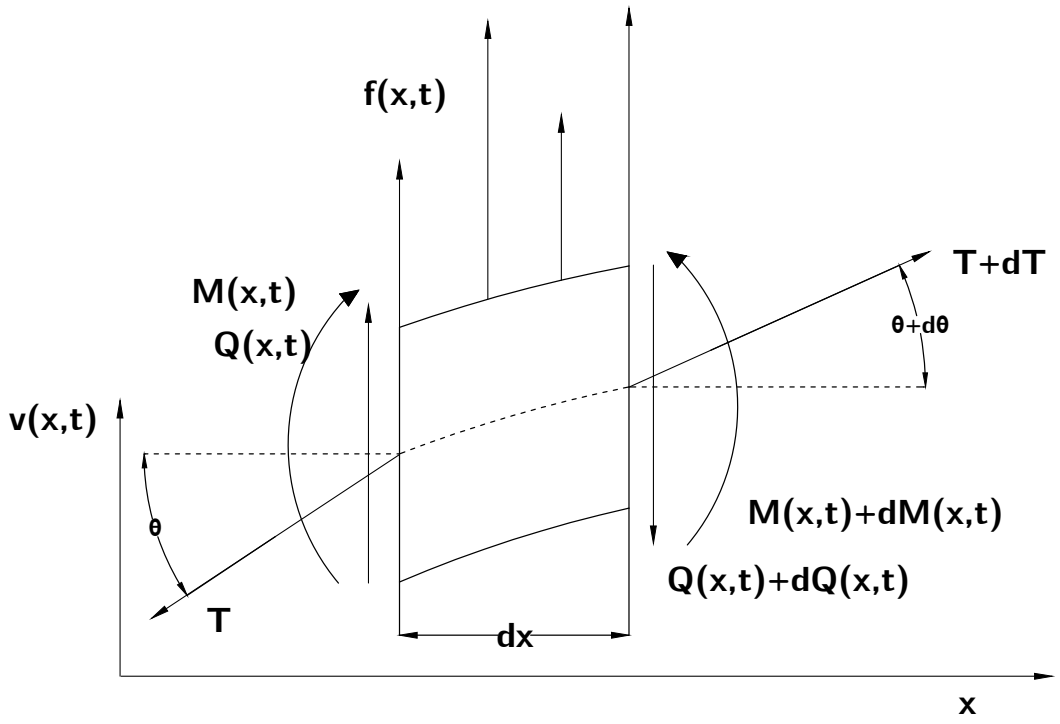

Figure 3.2: Representation of an infinitesimal beam element.

Considering the following parameters:

- $v(x,t)$ - Vertical displacement of the straight section;
- $f(x,t)$ - Force per unit length;
- $A(x)$ - Area of the straight section;
- $I(x)$ - Second moment of area of the straight section;
- E - Modulus of longitudinal elasticity;
- $\rho(x)$ - Volumic mass;
- T - Axial tension.

Before formulating the element, a few assumptions are considered:

- The Euler-Bernoulli beam theory is applicable since it is the case of a slender beam where the diameter is considerably smaller than the span length ($D << \frac{L}{20}$);
- The factor of mass per unit length ρA is considered constant throughout the entirety of the span length;
- The second moment of area I is also constant throughout the entirety of the span;

- The tension T at which the element is subjected to is also considered constant, even though it is clear that in the vicinity of the conductor clamps the tension is larger, albeit not a significant difference;
- Even though the conductor can have a wide range of flexural rigidity EI values, for this formulation it is considered constant throughout the entirety of the span;
- The rotation of the beam is much smaller when compared to the vertical displacement, therefore, the principle of small deformation can be assumed.

Remembering the Hamilton's Principle, where the variation of the kinetic and potential energy, summed with the variation of the work done by the non-conservative forces in any interval $[t_1, t_2]$ is equals to zero:

$$\int_{t_1}^{t_2} \delta(T - V)dt + \int_{t_1}^{t_2} \delta W_{nc}\, dt = 0, \tag{3.1}$$

where T represents the kinetic energy of the system, V the potential energy and W_{nc} the work done by the non-conservative forces. The δ represents the variation of T, V and W_{nc}.

Assuming that the kinetic energy exists only due to the vertical displacement of the straight section of the beam $v(x, t)$:

$$T = \frac{1}{2}\int_0^L \rho A \left(\frac{\partial v(x,t)}{\partial t}\right)^2 dx. \tag{3.2}$$

For the potential energy, the classical Euler-Bernoulli theory is applied where:

$$V = \frac{1}{2}\int_0^L EI \left(\frac{\partial^2 v(x,t)}{\partial x^2}\right)^2 dx. \tag{3.3}$$

Knowing that there can be a permutation between the variational operator δ and the partial derivation $\frac{\partial}{\partial x}$, the kinetic energy can be written as:

$$\begin{aligned} \delta T &= \int_0^L \rho A \left(\frac{\partial v(x,t)}{\partial t}\right) \delta \left(\frac{\partial v(x,t)}{\partial t}\right) dx \\ &= \int_0^L \rho A \frac{\partial v(x,t)}{\partial t} \frac{\partial}{\partial t}(\delta v(x,t))dx, \end{aligned} \tag{3.4}$$

therefore, the first term in equation (3.1) can be expressed as:

$$\int_{t_1}^{t_2} \delta T\, dt = \int_{t_1}^{t_2}\int_0^L \rho A \frac{\partial v(x,t)}{\partial t} \frac{\partial}{\partial t}(\delta v(x,t))dx\, dt, \tag{3.5}$$

and integrating by parts with respect to time, it is possible to obtain:

$$\begin{aligned} \int_{t_1}^{t_2} \delta T\, dt &= \int_{t_1}^{t_2}\int_0^L \rho A \frac{\partial v(x,t)}{\partial t} \frac{\partial}{\partial t}(\delta v(x,t))dx\, dt \\ &= \int_0^L \left(\rho A \frac{\partial v(x,t)}{\partial t}\delta v(x,t)\Big|_{t_1}^{t_2} - \int_{t_1}^{t_2} \rho A \frac{\partial^2 v(x,t)}{\partial t^2}\delta v(x,t)\right) dx. \end{aligned} \tag{3.6}$$

Considering that the variation $\delta v(x, t)$ is null for $t = t_1 = t_2$,

$$\delta v(x, t_1) = \delta v(x, t_2) = 0, \tag{3.7}$$

therefore, the kinetic energy variation can be written as:

$$\int_{t_1}^{t_2} \delta T\, dt = -\int_{t_1}^{t_2} \left(\int_0^L \rho A \frac{\partial^2 v(x,t)}{\partial t^2} \delta v(x,t) \right) dt. \tag{3.8}$$

The variation of the potential energy is described as:

$$\begin{aligned} \delta V &= \int_0^L EI \left(\frac{\partial^2 v(x,t)}{\partial x^2} \right) \delta \left(\frac{\partial^2 v(x,t)}{\partial x^2} \right) dx \\ &= \int_0^L EI \frac{\partial^2 v(x,t)}{\partial x^2} \frac{\partial^2}{\partial x^2} (\delta v(x,t)) dx, \end{aligned} \tag{3.9}$$

leading to the second term of equation (3.1) to become:

$$\int_{t_1}^{t_2} \delta V\, dt = \int_{t_1}^{t_2} \int_0^L EI \frac{\partial^2 v(x,t)}{\partial x^2} \frac{\partial^2}{\partial x^2} (\delta v(x,t)) dx dt. \tag{3.10}$$

Integrating by parts twice, with respect to x:

$$\begin{aligned} \int_{t_1}^{t_2} \delta V\, dt = \int_{t_1}^{t_2} &\left(EI \frac{\partial^2 v(x,t)}{\partial x^2} \frac{\partial^2}{\partial x^2} (\delta v(x,t)) \Big|_0^L - \frac{\partial}{\partial x} \left(EI \frac{\partial^2 v(x,t)}{\partial x^2} \right) \delta v(x,t) \Big|_0^L \right) dt \\ &+ \int_{t_1}^{t_2} \left(\int_0^L \frac{\partial^2}{\partial x^2} \left(EI \frac{\partial^2 v(x,t)}{\partial x^2} \right) \delta v(x,t) dx \right). \end{aligned} \tag{3.11}$$

The length variation of the beam element can be given as:

$$ds - dx = \left[(dx)^2 + \left(\frac{\partial v(x,t)}{\partial x} dx \right)^2 \right]^{\frac{1}{2}} - dx, \tag{3.12}$$

and that for small amplitudes of vibration equation (3.12) can be approximated as:

$$ds - dx \approx \sqrt{dx^2 + dv^2} - dx \approx \frac{1}{2} \left(\frac{\partial v}{\partial x} \right)^2 dx. \tag{3.13}$$

The work done by the axial force T can be expressed as:

$$W_T = -\frac{1}{2} \int_0^L T(x,t) \left(\frac{\partial v(x,t)}{\partial x} \right)^2 dx. \tag{3.14}$$

The work done by the transversal force $f(x,t)$ can be given as:

$$W_f = \int_0^L f(x,t) v(x,t) dx, \tag{3.15}$$

therefore, the total work done by the non-conservative forces is:

$$W_{nc} = W_T + W_f = -\frac{1}{2} \int_0^L T(x,t) \left(\frac{\partial v(x,t)}{\partial x} \right)^2 dx + \int_0^L f(x,t) v(x,t) dx, \tag{3.16}$$

and thus, the variation:

$$\begin{aligned} \delta W_{nc} &= -\int_0^L T \frac{\partial v(x,t)}{\partial x} \delta \left(\frac{\partial v(x,t)}{\partial x} \right) dx + \int_0^L f(x,t) \delta v(x,t) dx \\ &= -\int_0^L T \frac{\partial v(x,t)}{\partial x} \frac{\partial}{\partial x} (\delta v(x,t)) dx + \int_0^L f(x,t) \delta v(x,t) dx. \end{aligned} \tag{3.17}$$

Integrating by parts once the equation can be rewritten as:

$$\begin{aligned}\delta W_{nc} = &-T\frac{\partial v(x,t)}{\partial x}\delta v(x,t)\Big|_0^L + \int_0^L \frac{\partial}{\partial x}\left(T\frac{\partial v(x,t)}{\partial x}\right)\delta v(x,t)dx \\ &+ \int_0^L f(x,t)\delta v(x,t)dx.\end{aligned} \tag{3.18}$$

Substituting equations (3.8), (3.11) and (3.18) into equation (3.1), after grouping all the terms:

$$\begin{aligned}&-\int_{t_1}^{t_2}\int_0^L \left[\rho A\frac{\partial^2 v(x,t)}{\partial t^2} + \frac{\partial^2}{\partial x^2}\left(EI\frac{\partial^2 v(x,t)}{\partial x^2}\right) - \frac{\partial}{\partial x}\left(T\frac{\partial v(x,t)}{\partial x}\right) - f(x,t)\right]\delta v(x,t)dxdt \\ &-\int_{t_1}^{t_2} EI\frac{\partial^2 v(x,t)}{\partial x^2}\delta\left(\frac{\partial v(x,t)}{\partial x}\right)\Big|_0^L dt + \int_{t_1}^{t_2}\left[\frac{\partial}{\partial x}\left(EI\frac{\partial^2 v(x,t)}{\partial x^2}\right) - T\frac{\partial v(x,t)}{\partial x}\right]\delta v(x,t)\Big|_0^L dt = 0.\end{aligned} \tag{3.19}$$

Since $\delta v(x,t)$ is an arbitrary variation in x which interval is between 0 and L, the expression inside the double integral operation in equation (3.19) is equaled to zero, obtaining the equation of motion,

$$\frac{\partial^2}{\partial x^2}\left(EI\frac{\partial^2 v(x,t)}{\partial x^2}\right) - \frac{\partial}{\partial x}\left(T\frac{\partial v(x,t)}{\partial x}\right) + \rho A\frac{\partial^2 v(x,t)}{\partial t^2} = f(x,t) \quad 0 < x < L. \tag{3.20}$$

Equation (3.20) represents the equation of motion for the transversal vibration of the beam, to be verified in each straight section of the domain $0 < x < L$.

Taking the terms within the first order integrals present in equation (3.19) and equaling them to zero it is possible to obtain the generalized boundary conditions:

$$EI\frac{\partial^2 v(x,t)}{\partial x^2}\delta\left(\frac{\partial v(x,t)}{\partial x}\right)\Big|_0^L = 0, \tag{3.21}$$

$$\left[\frac{\partial}{\partial x}\left(EI\frac{\partial^2 v(x,t)}{\partial x^2}\right) - T\frac{\partial v(x,t)}{\partial x}\right]\delta v(x,t)\Big|_0^L = 0. \tag{3.22}$$

Equation (3.21) states that the moment (natural condition) or rotation (geometrical condition) are null at $x = 0$ or $x = L$,

$$EI\frac{\partial^2 v(x,t)}{\partial x^2}\Big|_{x=0,L} = 0; \qquad \frac{\partial v(x,t)}{\partial x}\Big|_{x=0,L} = 0, \tag{3.23}$$

where equation (3.22) states that the transverse force (natural condition) or vertical displacement (geometrical condition) must be null at $x = 0$ or $x = L$,

$$\frac{\partial}{\partial x}EI\frac{\partial^2 v(x,t)}{\partial x^2}\Big|_{x=0,L}; \qquad v(x,t)\Big|_{x=0,L} = 0. \tag{3.24}$$

3.1.1 Free vibration general solution

Considering a free vibration hypothesis the value $f(x,t)$ in equation (3.20) turns to zero, obtaining:

$$\frac{\partial^2}{\partial x^2}\left(EI\frac{\partial^2 v(x,t)}{\partial x^2}\right) - \frac{\partial}{\partial x}\left(T\frac{\partial v(x,t)}{\partial x}\right) + \rho A\frac{\partial^2 v(x,t)}{\partial t^2} = 0 \quad 0 < x < L. \tag{3.25}$$

In order to determine the movement of the beam it is necessary to solve the differential equation of motion and determine the solution $v(x,t)$ in space and time.

The hypothesis of synchronous movement, where the spatial configuration of the beam does not vary throughout time, is admitted. This way, it is possible to separate $v(x,t)$ in space and time, leading to a separation defined in the following form:

$$v(x,t) = V(x)g(t), \tag{3.26}$$

where $V(x)$ represents the spatial configuration of the beam and $g(t)$ determines the type of movement that the spatial configuration of the beam has, only dependent of time. In a stable harmonic vibration the function $g(t)$ is limited for all values of t. Derivating expression (3.26) with respect to x and t:

$$\frac{\partial^2 v(x,t)}{\partial x^2} = \frac{d^2V(x)}{dx^2}g(t) \qquad \frac{\partial^2 v(x,t)}{dt^2} = V(x)\frac{d^2g(t)}{dt^2}. \tag{3.27}$$

Due to the fact that $V(x)$ only depends of x and $g(t)$ only depends of t, the partial differential operators are substituted by total differential operations.

The equation of motion can then be rewritten as:

$$\frac{d^2}{dx^2}\left(EI\frac{d^2V(x)}{dx^2}\right) + \rho AV(x)\frac{d^2g(t)}{dt^2} - T\frac{d^2V(x)}{dx^2}g(t) = 0, \tag{3.28}$$

which can also be represented by:

$$\frac{1}{\rho AV(x)}\frac{d^2}{dx^2}\left(EI\frac{d^2V(x)}{dx^2}\right) - \frac{1}{\rho AV(x)}T\frac{d^2V(x)}{dx^2} = -\frac{1}{g(t)}\frac{d^2g(t)}{dt^2}, \tag{3.29}$$

where the first member depends solely of x and the second solely of t.

The equation (3.29) is therefore of distinct nature and it is only verified for all x and t if both members are equal to a constant, λ, for example. It translates to:

$$\frac{1}{\rho AV(x)}\frac{d^2}{dx^2}\left(EI\frac{d^2V(x)}{dx^2}\right) - \frac{1}{\rho AV(x)}T\frac{d^2V(x)}{dx^2} = \lambda, \tag{3.30}$$

and

$$-\frac{1}{g(t)}\frac{d^2g(t)}{dt^2} = \lambda. \tag{3.31}$$

After a rearranging of the variables the above equations can also be represented as:

$$\frac{d^2}{dx^2}\left(EI\frac{d^2V(x)}{dx^2}\right) - T\frac{d^2V(x)}{dx^2} - \lambda\rho AV(x) = 0, \tag{3.32}$$

and

$$\frac{d^2g(t)}{dt^2} + \lambda g(t) = 0. \tag{3.33}$$

Making the constant λ equals to ω^2, the equations are written as:

$$\frac{d^2}{dx^2}\left(EI\frac{d^2V(x)}{dx^2}\right) - T\frac{d^2V(x)}{dx^2} - \omega^2\rho AV(x) = 0, \tag{3.34}$$

$$\frac{d^2g(t)}{dt^2} + \omega^2 g(t) = 0. \tag{3.35}$$

Equation (3.35) represents an ordinary differential equation where the solution is of the type:

$$g(t) = C\cos\omega t + D\sin\omega t, \tag{3.36}$$

and equation (3.34) represents a problem where the solutions $V(x)$ have to verify the differential equation. Therefore, the solution for equation (3.26) is written as:

$$v(x,t) = V(x)(C\cos\omega t + D\sin\omega t), \tag{3.37}$$

where the constants C and D are determined by the initial conditions.

Assuming that the solution of $V(x)$ is in the form of:

$$V(x) = Ce^{sx}, \tag{3.38}$$

where C is a constant, equation (3.34) has the following auxiliary solution:

$$s^4 - \frac{T}{EI}s^2 - \frac{\rho A\omega^2}{EI} = 0, \tag{3.39}$$

where the squared roots of equation (3.39) are given by:

$$s_{1,2}^2 = \frac{T}{2EI} \pm \sqrt{\left(\frac{T}{2EI}\right)^2 + \frac{\rho A\omega^2}{EI}}. \tag{3.40}$$

Thus, equation (3.39) presents real and imaginary roots as follows,

$$s_1 = -s_3 \in \mathbb{R} \tag{3.41}$$

$$s_2 = -s_4 \in \mathbb{C}. \tag{3.42}$$

Therefore, the general solution for $V(x)$ is a combination of exponentials,

$$V(x) = C_1e^{s_1x} + C_2e^{-s_1x} + C_3e^{js_2x} + C_4e^{-js_2x}. \tag{3.43}$$

All the constants are defined by the boundary conditions. Redefining C_1 and C_2 as $C_1 = A_1 + A_2$ and $C_2 = A_1 - A_2$, being A_1 and A_2 two new constants, the previous equation can be written as:

$$\begin{aligned} V(x) &= \frac{1}{2}(A_1 + A_2)e^{s_1x} + \frac{1}{2}(A_1 - A_2)e^{-s_1x} \\ &\quad + C_3\cos s_2x + jC_3\sin s_2x + C_4\cos s_2x - jC_4\sin s_2x \\ &= \frac{1}{2}A_1(e^{s_1x} + e^{-s_1x}) + \frac{1}{2}A_2(e^{s_1x} - e^{-s_1x}) \\ &\quad + (C_3 + C_4)\cos s_2x + j(C_3 - C_4)\sin s_2x, \end{aligned} \tag{3.44}$$

considering that $C_3 + C_4 = A_3$, $C_3 - C_4 = A_4$ and taking into consideration the definition of the hyperbolic functions:

$$V(x) = A_1\cosh s_1x + A_2\sinh s_1x + A_3\cos s_2x + A_4\sin s_2x. \tag{3.45}$$

3.1.1.1 Simply-supported boundary condition

It is possible to describe a simply-supported boundary condition as the following set of equations:

$$V(0) = 0, \tag{3.46}$$

$$EI\frac{d^2V(x)}{dx^2}\Big|_{x=0} = 0, \tag{3.47}$$

$$V(l) = 0, \tag{3.48}$$

$$EI\frac{d^2V(x)}{dx^2}\Big|_{x=L} = 0. \tag{3.49}$$

Knowing that the second derivation of $V(x)$ is

$$\frac{d^2V(x)}{dx^2} = A_1 s_1^2 \cosh s_1 x + A_2 s_2^2 \sinh s_2 x - A_3 s_2^2 \cos s_2 x - A_4 s_2^2 \sin s_2 x. \tag{3.50}$$

Inserting the conditions obtained at $x = 0$ in equations (3.45) and (3.50) it is possible to retrieve that,

$$A_1 = A_3 = 0, \tag{3.51}$$

which allows to simplify equations (3.45) and (3.50) into the following,

$$V(x) = A_2 \sinh s_1 x + A_4 \sin s_2 x, \tag{3.52}$$

$$\frac{d^2V(x)}{dx^2} = A_2 s_2^2 \sinh s_2^2 x - A_4 s_2^2 \sin s_2 x. \tag{3.53}$$

Substituting the boundary conditions for $x = L$ in a set of homogeneous system of algebraic equations,

$$\begin{cases} A_2 \sin s_1 L + A_4 \sin s_2 L = 0 \\ A_2 s_1^2 \sinh s_1 L - A_4 s_2^2 \sin s_2 L = 0 \end{cases} \tag{3.54}$$

which can be written in a matrix form as

$$\begin{bmatrix} \sinh s_1 L & \sin s_2 L \\ s_1^2 \sinh s_1 L & -s_2^2 \sin s_2 L \end{bmatrix} \begin{Bmatrix} A_2 \\ A_4 \end{Bmatrix} = \begin{Bmatrix} 0 \\ 0 \end{Bmatrix}. \tag{3.55}$$

For an homogeneous system to contain non-null solutions, the matrix determinant must be null,

$$\begin{vmatrix} \sinh s_1 L & \sin s_2 L \\ s_1^2 \sinh s_1 L & -s_2^2 \sin s_2 L \end{vmatrix} = 0, \tag{3.56}$$

and resolving the determinant of the equation the solution gives,

$$\sin s_2 L(\sinh s_1 L(s_1^2 + s_2^2)) = 0. \tag{3.57}$$

Knowing that $s_1 L > 0$, it implies that $\sinh s_1 L > 0$, obtaining the following equation of frequencies,

$$\sin s_2 L = 0, \tag{3.58}$$

where the roots of $s_{2n}L$ for $n = 1, ..., \infty$, are

$$s_{2n}L = n\pi. \tag{3.59}$$

The solution for s_2 was already found in equation (3.40) and introducing the solution in the above equation and solving it in order of ω_n:

$$\omega_n = \frac{\pi^2}{L^2}\sqrt{\frac{EI}{\rho A}}\sqrt{n^4 + \frac{n^2 T L^2}{\pi^2 EI}} \quad \text{for} \quad n = 1, ..., \infty, \tag{3.60}$$

gives the value of the natural frequencies for any mode of vibration n.

3.2 Conductor finite element

For this work, to model the conductor, the Euler-Bernoulli element with two degrees of freedom per node was chosen. A visual representation of the element can be seen in Figure 3.3. In order to utilize it for simulation purposes it is necessary do discretize it into a singular element which will be a part of a larger assembly of elements. The element is formulated using the Weighted-Residual Method and the approximation of the solution and weight functions is done with the Galerkin Method [Reddy, 2006].

Figure 3.3: Schematical representation of a two degrees of freedom per node Euler-Bernoulli Element.

Considering the equation of motion (3.20) for an Euler-Bernoulli beam under axial tension,

$$\frac{\partial^2}{\partial x^2}\left(EI\frac{\partial^2 v(x,t)}{\partial x^2}\right) - \frac{\partial}{\partial x}\left(T\frac{\partial v(x,t)}{\partial x}\right) + \rho A\frac{\partial^2 v(x,t)}{\partial t^2} = f(x,t), \tag{3.61}$$

it is possible to discretize it into a singular element by applying an integral throughout a determined length L. The equation is also multiplied by a weight function W:

$$\begin{aligned}\int_0^L \frac{\partial^2}{\partial x^2}\left(EI\frac{\partial^2 v(x,t)}{\partial x^2}\right)W\,dx + \int_0^L -\frac{\partial}{\partial x}\left(T\frac{\partial v(x,t)}{\partial x}\right)W\,dx + \int_0^L \rho A\frac{\partial^2 v(x,t)}{\partial t^2}W\,dx \\ = \int_0^L f(x,t)W\,dx.\end{aligned} \tag{3.62}$$

It is necessary to equally distribute the derivations. Firstly, the term regarding the elastic behaviour of the system is integrated twice leading to:

$$\begin{aligned}\int_0^L \frac{\partial^2}{\partial x^2}\left(EI\frac{\partial^2 v(x,t)}{\partial x^2}\right)W\,dx = EIW\frac{\partial^3 v(x,t)}{\partial x^3}\Big|_0^L - EI\frac{\partial W}{\partial x}\frac{\partial^2 v(x,t)}{\partial x^2}\Big|_0^L \\ + \int_0^L EI\frac{\partial^2 v(x,t)}{\partial x^2}\frac{\partial^2 W}{\partial x^2}dx,\end{aligned} \tag{3.63}$$

where the first two terms of the equation above are null due to the boundary conditions previously defined. Then, it is necessary to integrate by parts once the term relating to the axial force applied to the element:

$$-\int_0^L T\frac{\partial^2 v(x,t)}{\partial x^2}W\,dx = -\left(TW\frac{\partial v(x,t)}{\partial x}\Big|_0^L - \int_0^L T\frac{\partial v(x,t)}{\partial x}\frac{\partial W}{\partial x}dx\right). \tag{3.64}$$

Similarly to the integration of the elastic behaviour term, the first term of the equation above is also null due to boundary conditions.

With all the integrations distributed the equation of motion can be written as:

$$\int_0^L EI\frac{\partial^2 v(x,t)}{\partial x^2}\frac{\partial^2 W}{\partial x^2}dx + \int_0^L T\frac{\partial v(x,t)}{\partial x}\frac{\partial W}{\partial x}dx + \int_0^L \rho A\frac{\partial^2 v(x,t)}{\partial t^2}W dx = \int_0^L f(x,t)W dx. \tag{3.65}$$

As previously stated, the approximation of the unknown function v(x,t) and the weight function is done using the Galerkin Method, therefore,

$$W = Nw \quad \text{and} \quad v(x,t) = Nw, \tag{3.66}$$

where N is the vector containing all the shape functions for all degrees of freedom and w is the vector containing the generalized coordinates of the element and can be represented as:

$$N = \left\{ \begin{array}{c} N_1 \\ \overline{N_1} \\ N_2 \\ \overline{N_2} \end{array} \right\}, \tag{3.67}$$

$$w = \{ v_1 \quad \theta_1 \quad v_2 \quad \theta_2 \}. \tag{3.68}$$

Making the necessary changes to obtain the matricial form, it is possible to obtain:

$$\int_0^L EIw^T N''^T N'' w dx + \int_0^L Tw^T N'^T N' w dx + \int_0^L \rho A w^T N^T N\ddot{w} dx = \int_0^L f(x,t)w^T N^T dx, \tag{3.69}$$

which can be rearranged as:

$$w^T\left(\int_0^L EIN''^T N'' w dx + \int_0^L TN'^T N' w dx + \int_0^L \rho A N^T N\ddot{w} dx\right) = w^T \int_0^L f(x,t)N^T dx. \tag{3.70}$$

Knowing that it is valid for any approximation function the above equation can be simplified as:

$$\left(\int_0^L EIN''^T N'' dx\right) w + \left(\int_0^L TN'^T N' dx\right) w + \left(\int_0^L \rho A N^T N dx\right)\ddot{w} = \int_0^L f(x,t)N^T dx, \tag{3.71}$$

where,

$$EI\int_0^L N''^T N'' dx \rightarrow \mathrm{K}, \tag{3.72}$$

$$T\int_0^L N'^T N' dx \rightarrow \mathrm{K_T}, \tag{3.73}$$

$$\rho A\int_0^L N^T N dx \rightarrow \mathrm{M}, \tag{3.74}$$

$$f(x,t)\int_0^L N^T dx \rightarrow \mathrm{F}. \tag{3.75}$$

The matrix identified as K stands as the standard Euler-Bernoulli stiffness matrix, $\mathrm{K_T}$ is the additional stiffness matrix due to axial tension and is added to the standard stiffness matrix. M is the mass matrix of the element and F is the force vector.

Equation (3.71) can then be rewritten as:

$$[M]\{\ddot{w}\} + ([K] + [K_T])\{w\} = \{F\}. \tag{3.76}$$

As a final remark it is important to note that due to the fact that each of the nodes have two degrees of freedom, with the rotation being the derivative of the displacement, the shape functions have to be Hermitian shape functions that have the following formulation [Oñate, 2013]:

$$\begin{aligned} N_1 &= \frac{1}{4}(2 - 3\xi + \xi^3), & N_2 &= \frac{1}{4}(2 + 3\xi - \xi^3), \\ \overline{N_1} &= \frac{1}{4}(1 - \xi - \xi^2 + \xi^3), & \overline{N_2} &= \frac{1}{4}(-1 - \xi + \xi^2 + \xi^3), \end{aligned} \tag{3.77}$$

where ξ can be defined as [Oñate, 2013]:

$$\xi = \frac{2}{l}(x - x_c) \qquad \text{with} \qquad x_c = \frac{x_1 + x_2}{2}. \tag{3.78}$$

Figure 3.4 demonstrates the element with coordinates along ξ.

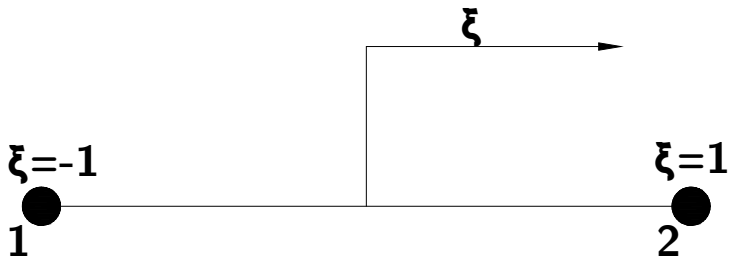

Figure 3.4: Schematical representation of the element parametrization.

Once completed the formulation of the element it is necessary to assemble them into a series of connected elements to form the entirety of the conductor, as exemplified in Figure 3.5.

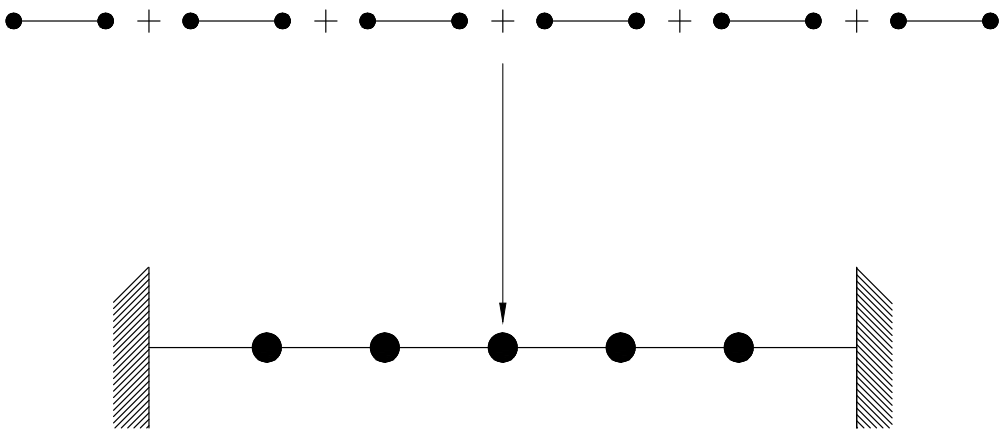

Figure 3.5: Schematical example of the assembly of various elements into a conductor.

3.3 Conductor-damper modeling

To effectively model the damper a similar approach to [Barry, 2010] was considered, where the damper element is an assembly of a conductor element with an element with 3 nodes that represent both the messenger wires with weights in each extremity, as seen in Figure 3.6.

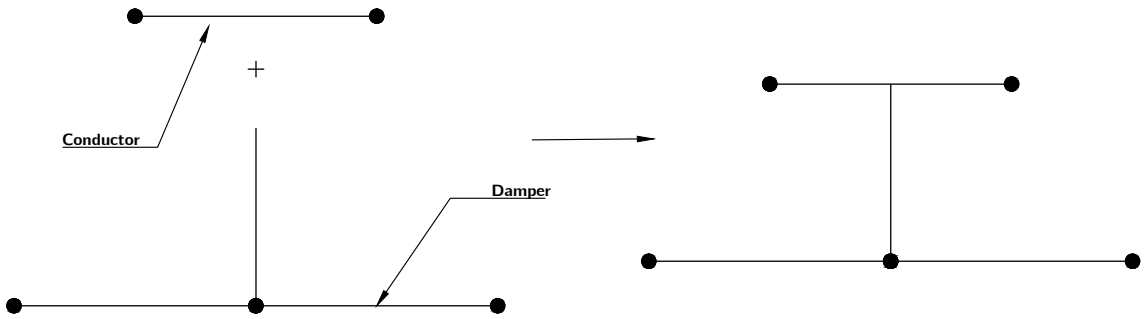

Figure 3.6: Representation of the formation of the damper element.

Figure 3.7 shows the visual representation of part of the conductor with one damper attached at a given position.

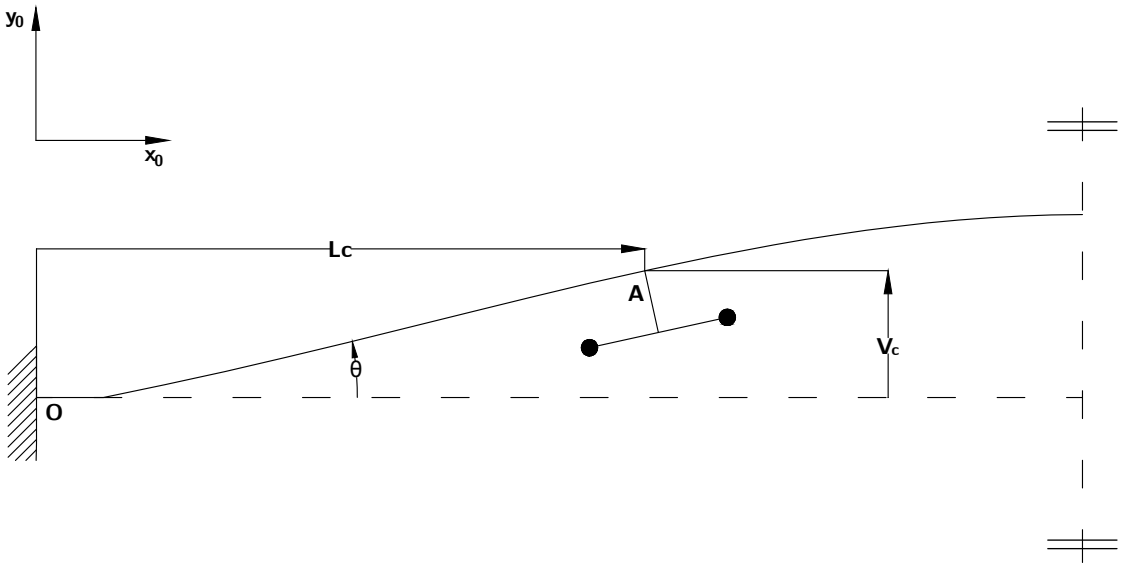

Figure 3.7: Representation the conductor, with one Stockbridge damper attached.

In the formulation of the conductor-damper finite element, an energetic approach is followed and the Hamilton's Principle is used to derive the variational weak form to obtain the elemental matrices and vectors. In order to better understand the dynamics of a Stockbridge damper, Figure 3.8 presents a zoom of the actual damper at a certain vibration position of the conductor.

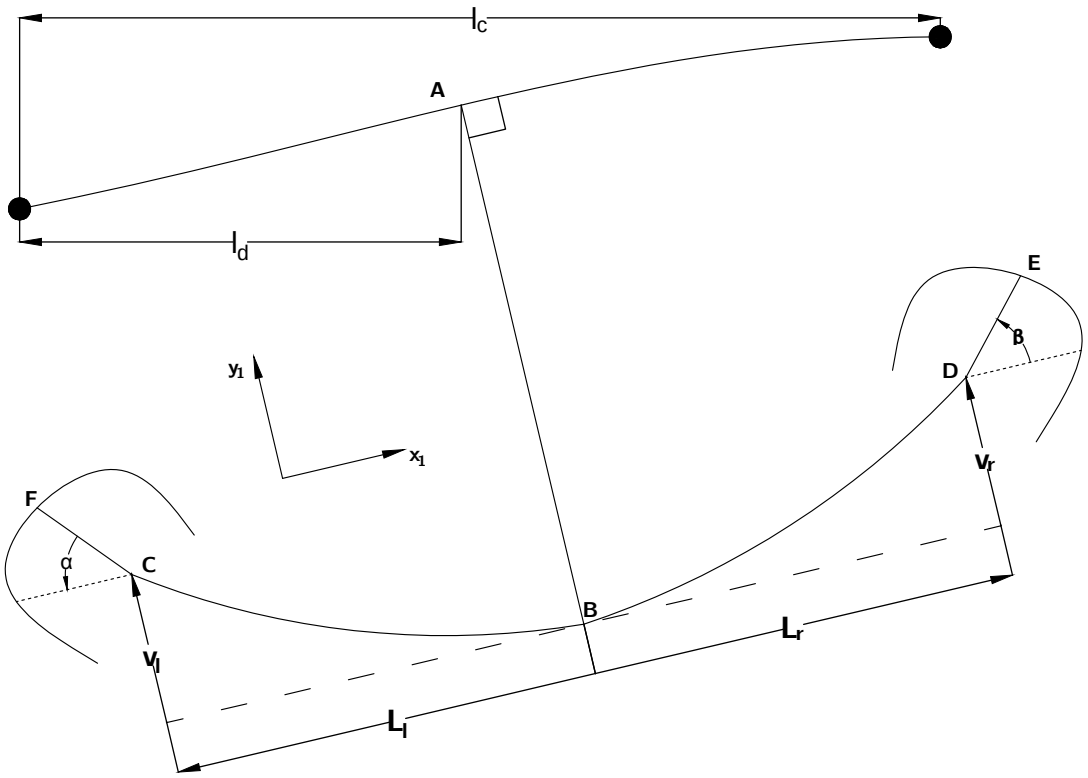

Figure 3.8: Schematical representation of a Stockbridge damper when positioned along the span of a conductor.

It is clear to see that due to the clamp high rigidity in comparison to the messenger cable and the conductor, the damper clamp is always positioned at a $90°$ angle in relation to the conductor. It is then necessary to define the various positions of the points of the damper. If not explicitly stated, all vectors and matrices must be considered in the S_0 axis system presented in Figure 3.7. The position of the damper attachment along the conductor is given as:

$$\overrightarrow{OA} = \left\{ \begin{array}{c} L_c \\ v_c \\ 0 \end{array} \right\}. \tag{3.79}$$

The transformation matrix for the S_1 axis system to the S_0 axis system can be determined as:

$$[T_{10}] = \left[\begin{array}{ccc} \cos\theta & -\sin\theta & 0 \\ \sin\theta & \cos\theta & 0 \\ 0 & 0 & 1 \end{array} \right]. \tag{3.80}$$

Note that all rotations are very small when compared to the vertical displacements, therefore the following simplifications were done:

$$\cos\theta \approx 1, \qquad \sin\theta \approx \theta. \tag{3.81}$$

The operation of having a generic vector $\overrightarrow{PQ}$ expressed in the S_1 axis system, transformed into the S_0 axis system can be described as:

$$\overrightarrow{PQ}|_{S_0} = [T_{10}]\overrightarrow{PQ}|_{S_1}, \tag{3.82}$$

therefore,

$$\overrightarrow{AB}|_{S_1} = \begin{Bmatrix} 0 \\ -h \\ 0 \end{Bmatrix} \Rightarrow \overrightarrow{AB}|_{S_0} = \begin{Bmatrix} h\theta \\ -h \\ 0 \end{Bmatrix}, \tag{3.83}$$

where h is the height of the clamp of the damper. Remembering that, for three arbitrary points G, P and Q,

$$\overrightarrow{PQ} = \overrightarrow{PG} + \overrightarrow{GQ}, \tag{3.84}$$

and that, if a position vector is given, the velocity can be obtained by the direct derivation of said vector. It is then possible to have the following:

$$\overrightarrow{OB} = \overrightarrow{OA} + \overrightarrow{AB} = \begin{Bmatrix} L_c + h\theta \\ v_c - h \\ 0 \end{Bmatrix}; \overrightarrow{v_B} = \dot{\overrightarrow{OB}} = \begin{Bmatrix} h\dot{\theta} \\ \dot{v_c} \\ 0 \end{Bmatrix}; \tag{3.85}$$

$$\overrightarrow{BC}|_{S_1} = \begin{Bmatrix} -L_l \\ v_l \\ 0 \end{Bmatrix} \Rightarrow \overrightarrow{BC}|_{S_0} = \begin{Bmatrix} -L_l - v_l\theta \\ -L_l\theta + v_l \\ 0 \end{Bmatrix}; \overrightarrow{OC}|_{S_0} = \begin{Bmatrix} L_c + h\theta - L_l - v_l\theta \\ v_c - h - L_l\theta + v_l \\ 0 \end{Bmatrix}; \tag{3.86}$$

$$\overrightarrow{BD}|_{S_1} = \begin{Bmatrix} L_r \\ v_r \\ 0 \end{Bmatrix} \Rightarrow \overrightarrow{BD}|_{S_0} = \begin{Bmatrix} L_r - v_r\theta \\ L_r\theta + v_r \\ 0 \end{Bmatrix}; \overrightarrow{OD}|_{S_0} = \begin{Bmatrix} L_c + h\theta + L_r - v_r\theta \\ v_c - h + L_r\theta + v_r \\ 0 \end{Bmatrix}; \tag{3.87}$$

$$\overrightarrow{v_C} = \dot{\overrightarrow{OC}} = \begin{Bmatrix} h\dot{\theta} - \dot{v_l}\theta - v_l\dot{\theta} \\ \dot{v_c} - L_l\dot{\theta} + \dot{v_l} \\ 0 \end{Bmatrix}; \overrightarrow{v_D} = \dot{\overrightarrow{OD}} = \begin{Bmatrix} h\dot{\theta} - \dot{v_r}\theta - v_r\dot{\theta} \\ \dot{v_c} + L_r\dot{\theta} + \dot{v_r} \\ 0 \end{Bmatrix}. \tag{3.88}$$

Before the determination of the kinetic and potential energies of the conductor it is important to note the following, in order to understand the transition of the formulation to a matricial form:

$$\begin{aligned} v_c &= N_c w_c, \quad & v_l &= N_l w_l, \quad & v_r &= N_r w_r, \\ \theta &= N_c^{'} w_c, \quad & \alpha &= N_l^{'} w_l, \quad & \beta &= N_r^{'} w_r, \end{aligned} \tag{3.89}$$

where N_c and w_c relate to the shape functions of the conductor part of the damper element and the generalized coordinates, respectively. The same applies for N_l and w_l which relates to the left messenger with N_r and w_r for the right messenger. Note that the angles α and β are the rotations of the left and right counterweights, relative to their center of mass present on the messenger, respectively.

Before defining each of the kinetic and potential energies of the system, some variables have to be introduced into the problem.

- EI_{ml} and EI_{mr} are the flexural rigidities of each of the messenger cables, left and right, respectively;
- The same goes for the mass per unit length of each of the messenger cables, ρA_{ml} and ρA_{mr};
- The moment of inertia of each of the damper counterweights (J_{dl} and J_{dr}), resultant of the rotation of each of the masses relative to their center of masses, present in each of their respective messengers.

The same subscript nomenclatures are also used for the definition of each of the kinetic and potential energies.

3.3.1 Kinetic energy

In order to obtain the mass matrix it is necessary to determine the kinetic energies of the all the relevant components of the damper.

3.3.1.1 Conductor

For the kinetic energy of the conductor, the velocity at a generic point A is given by,

$$\overrightarrow{OA} = \begin{Bmatrix} L_c \\ v_c \\ 0 \end{Bmatrix}; \overrightarrow{v_A} = \begin{Bmatrix} 0 \\ \dot{v_c} \\ 0 \end{Bmatrix}. \tag{3.90}$$

Therefore, the kinetic energy of the conductor can be defined as:

$$T_c = \frac{1}{2}\int_m \overrightarrow{v_A}.\overrightarrow{v_A} dm = \frac{1}{2}\rho A_c \int_0^{l_c} \dot{v_c}^2 dx_c, \tag{3.91}$$

which in matricial form can be written as,

$$T_c = \frac{1}{2}\rho A_c \int_0^{l_c} \dot{w_c}^T N_c^T N_c \dot{w_c} dx_c. \tag{3.92}$$

3.3.1.2 Damper counterweights

The next step is to define the kinetic energies of each of the counterweights. Remembering the Mozzi equation for determination of the velocity of an arbitrary point P, knowing the velocity of another arbitrary point Q,

$$\overrightarrow{v_P} = \overrightarrow{v_Q} + \overrightarrow{\omega} \times \overrightarrow{QP}. \tag{3.93}$$

The kinetic energy of the left and right counterweights can be defined as,

$$\begin{aligned} T_{dl} &= \frac{1}{2}\int_m \overrightarrow{v_F}.\overrightarrow{v_F} = \frac{1}{2}\int_m (\overrightarrow{v_C} + \overrightarrow{\omega_{20}} \times \overrightarrow{CF}).(\overrightarrow{v_C} + \overrightarrow{\omega_{20}} \times \overrightarrow{CF}) dm \\ &= \frac{1}{2}\int_m \overrightarrow{v_C}.\overrightarrow{v_C} + 2.\overrightarrow{v_C}(\overrightarrow{\omega_{20}} \times \overrightarrow{CF}) + (\overrightarrow{\omega_{20}} \times \overrightarrow{CF}).(\overrightarrow{\omega_{20}} \times \overrightarrow{CF}) dm, \end{aligned} \tag{3.94}$$

$$\begin{aligned} T_{dr} &= \frac{1}{2}\int_m \overrightarrow{v_E}.\overrightarrow{v_E} = \frac{1}{2}\int_m (\overrightarrow{v_D} + \overrightarrow{\omega_{30}} \times \overrightarrow{DE}).(\overrightarrow{v_D} + \overrightarrow{\omega_{30}} \times \overrightarrow{DE}) dm \\ &= \frac{1}{2}\int_m \overrightarrow{v_D}.\overrightarrow{v_D} + 2\overrightarrow{v_D}.(\overrightarrow{\omega_{30}} \times \overrightarrow{DE}) + (\overrightarrow{\omega_{30}} \times \overrightarrow{DE}).(\overrightarrow{\omega_{30}} \times \overrightarrow{DE}) dm. \end{aligned} \tag{3.95}$$

The values of the angular velocity $\overrightarrow{\omega_{20}}$ and $\overrightarrow{\omega_{30}}$ are:

$$\overrightarrow{\omega_{20}} = \begin{Bmatrix} 0 \\ 0 \\ \dot{\alpha} + \dot{\theta} \end{Bmatrix}, \qquad \overrightarrow{\omega_{30}} = \begin{Bmatrix} 0 \\ 0 \\ \dot{\beta} + \dot{\theta} \end{Bmatrix}. \tag{3.96}$$

Note that the angular velocities consist of the absolute values of velocity of the left and right counterweights, respectively. Separating the terms of the kinetic energy for the left damper counterweight into three different integrations,

$$\begin{aligned}\frac{1}{2}\int_m \overrightarrow{v_C}.\overrightarrow{v_C}dm =&\frac{1}{2}m_l((h\dot{\theta}-\dot{v_l}\theta-v_l\dot{\theta})^2+(\dot{v_c}-L_l\dot{\theta}+\dot{v_l})^2)\\ =&\frac{1}{2}m_l(\dot{\theta}^2h^2+\dot{v_l}^2\theta^2+v_l^2\dot{\theta}^2-2h\dot{\theta}\dot{v_l}\theta-2hv_l\dot{\theta}^2+2\dot{v_l}\theta v_l\dot{\theta}\\ &+\dot{v_c}^2+L_l^2\dot{\theta}^2+\dot{v_l}^2-2L_l\dot{v_c}\dot{\theta}+2\dot{v_c}\dot{v_l}-2L_l\dot{\theta}\dot{v_l})\\ =&\frac{1}{2}m_l(\dot{\theta}^2h^2+\dot{v_c}^2+L_l^2\dot{\theta}^2+\dot{v_l}^2-2L_l\dot{v_c}\dot{\theta}+2\dot{v_c}\dot{v_l}-2L_l\dot{\theta}\dot{v_l}).\end{aligned} \tag{3.97}$$

It is important to note that in the equation above, all terms equals and above of the third order were dismissed. The following integration results into the first moment with relation to the center of mass of the counterweight, which is:

$$\frac{1}{2}\int_m 2\overrightarrow{v_C}.(\overrightarrow{\omega_{20}}\times\overrightarrow{CF})dm=0. \tag{3.98}$$

The final integration results into:

$$\frac{1}{2}\int_m(\overrightarrow{\omega_{20}}\times\overrightarrow{CF}).(\overrightarrow{\omega_{20}}\times\overrightarrow{CF})dm=\frac{1}{2}J_{dl}(\dot{\alpha}+\dot{\theta})^2, \tag{3.99}$$

therefore, the kinetic energy of the left counterweight can be written as

$$T_{dl}=\frac{1}{2}m_l(\dot{\theta}^2h^2+\dot{v_c}^2+L_l^2\dot{\theta}^2+\dot{v_l}^2-2L_l\dot{v_c}\dot{\theta}+2\dot{v_c}\dot{v_l}-2L_l\dot{\theta}\dot{v_l})+\frac{1}{2}J_{dl}(\dot{\alpha}+\dot{\theta})^2. \tag{3.100}$$

The same procedure is done for the right counterweight,

$$\begin{aligned}\frac{1}{2}\int_m \overrightarrow{v_D}.\overrightarrow{v_D}dm =&\frac{1}{2}m_r((h\dot{\theta}-\dot{v_r}\theta-v_r\dot{\theta})^2+(\dot{v_c}+L_r\dot{\theta}+\dot{v_r})^2)\\ =&\frac{1}{2}m_r(\dot{\theta}^2h^2+\dot{v_r}^2\theta^2+v_r^2\dot{\theta}^2-2h\dot{\theta}\dot{v_r}\theta-2hv_r\dot{\theta}^2+2\dot{v_r}\theta v_r\dot{\theta}\\ &+\dot{v_c}^2+L_r^2\dot{\theta}^2+\dot{v_r}^2+2L_r\dot{v_c}\dot{\theta}+2\dot{v_c}\dot{v_r}+2L_r\dot{\theta}\dot{v_r})\\ =&\frac{1}{2}m_r(\dot{\theta}^2h^2+\dot{v_c}^2+L_r^2\dot{\theta}^2+\dot{v_r}^2+2L_r\dot{v_c}\dot{\theta}+2\dot{v_c}\dot{v_r}+2L_r\dot{\theta}\dot{v_r}),\end{aligned} \tag{3.101}$$

$$\frac{1}{2}\int_m 2\overrightarrow{v_D}.(\overrightarrow{\omega_{30}}\times\overrightarrow{DE})dm=0, \tag{3.102}$$

$$\frac{1}{2}\int_m(\overrightarrow{\omega_{30}}\times\overrightarrow{DE}).(\overrightarrow{\omega_{30}}\times\overrightarrow{DE})dm=\frac{1}{2}J_{dr}(\dot{\beta}+\dot{\theta})^2. \tag{3.103}$$

The kinetic energy of the right counterweight can be defined as,

$$T_{dr}=\frac{1}{2}m_r(\dot{\theta}^2h^2+\dot{v_c}^2+L_r^2\dot{\theta}^2+\dot{v_r}^2+2L_r\dot{v_c}\dot{\theta}+2\dot{v_c}\dot{v_r}+2L_r\dot{\theta}\dot{v_r})+\frac{1}{2}J_{dr}(\dot{\beta}+\dot{\theta})^2. \tag{3.104}$$

Both kinetic energies can be written in matricial form as,

$$\begin{aligned}T_{dl}=&\frac{1}{2}m_l(\dot{w_c}^T{N_c'}^T N_c'\dot{w_c}h^2+\dot{w_c}^T N_c^T N_c\dot{w_c}+L_l^2\dot{w_c}^T{N_c'}^T N_c'\dot{w_c}+\dot{w_l}^T N_l^T N_l\dot{w_l}\\ &-2L_l\dot{w_c}^T N_c^T N_c'\dot{w_c}+2\dot{w_c}^T N_c^T N_l\dot{w_l}-2L_l\dot{w_c}^T{N_c'}^T N_l\dot{w_l})\\ &+\frac{1}{2}J_{dl}(\dot{w_l}^T{N_l'}^T N_l'\dot{w_l}+2\dot{w_l}^T{N_l'}^T N_c'\dot{w_c}+\dot{w_c}^T{N_c'}^T N_c'\dot{w_c}),\end{aligned} \tag{3.105}$$

$$\begin{aligned} T_{dr} =& \frac{1}{2} m_r (\dot{w}_c{}^T N_c'{}^T N_c' \dot{w}_c h^2 + \dot{w}_c{}^T N_c{}^T N_c \dot{w}_c + L_r^2 \dot{w}_c{}^T N_c'{}^T N_c' \dot{w}_c + \dot{w}_r{}^T N_r{}^T N_r \dot{w}_r \\ &+ 2 L_r \dot{w}_c{}^T N_c^T N_c' \dot{w}_c + 2 \dot{w}_c{}^T N_c^T N_r \dot{w}_r + 2 L_r \dot{w}_c{}^T N_c'{}^T N_r \dot{w}_r) \\ &+ \frac{1}{2} J_{dr} (\dot{w}_r{}^T N_r'{}^T N_r' \dot{w}_r + 2 \dot{w}_r{}^T N_r'{}^T N_c' \dot{w}_c + \dot{w}_c{}^T N_c'{}^T N_c' \dot{w}_c), \end{aligned} \tag{3.106}$$

being m_l and m_r the total value of mass of each of the counterweights.

3.3.1.3 Messenger wires

For the messenger wires it is necessary to consider any given point throughout the messenger cable. Therefore, two new points are considered, C' and D', where

$$\overrightarrow{BC'}|_{S_1} = \begin{Bmatrix} -x_l \\ v_l \\ 0 \end{Bmatrix} \Rightarrow \overrightarrow{BC'}|_{S_0} = \begin{Bmatrix} -x_l - v_l\theta \\ -x_l\theta + v_l \\ 0 \end{Bmatrix}, \tag{3.107}$$

$$\overrightarrow{BD'}|_{S_1} = \begin{Bmatrix} x_r \\ v_r \\ 0 \end{Bmatrix} \Rightarrow \overrightarrow{BD'}|_{S_0} = \begin{Bmatrix} x_r - v_r\theta \\ x_r\theta + v_r \\ 0 \end{Bmatrix}, \tag{3.108}$$

$$\overrightarrow{OC'}|_{S_0} = \begin{Bmatrix} L_c + \theta h - x_l + v_l\theta \\ v_c - h + x_l\theta + v_l \\ 0 \end{Bmatrix}; \overrightarrow{v_{C'}}|_{S_0} = \begin{Bmatrix} \dot{\theta} h - \dot{v}_l\theta - v_l\dot{\theta} \\ \dot{v}_c - x_l\dot{\theta} + \dot{v}_l \\ 0 \end{Bmatrix}, \tag{3.109}$$

$$\overrightarrow{OD'}|_{S_0} = \begin{Bmatrix} L_c + \theta h + x_r - v_r\theta \\ v_c - h + x_r\theta + v_r \\ 0 \end{Bmatrix}; \overrightarrow{v_{C'}}|_{S_0} = \begin{Bmatrix} \dot{\theta} h - \dot{v}_r\theta - v_r\dot{\theta} \\ \dot{v}_c + x_r\dot{\theta} + \dot{v}_r \\ 0 \end{Bmatrix}. \tag{3.110}$$

The kinetic energies of the left and right messenger can be determined, respectively:

$$\begin{aligned} T_{ml} =& \frac{1}{2} \int_m \overrightarrow{v_{C'}} . \overrightarrow{v_{C'}} dm = \frac{1}{2} \rho A_{ml} \int_0^{L_l} (\dot{\theta} h - \dot{v}_l\theta - v_l\dot{\theta})^2 + (\dot{v}_c - x_l\dot{\theta} + \dot{v}_l)^2 dx_l \\ =& \frac{1}{2} \rho A_{ml} \int_0^{L_l} (\dot{\theta}^2 h^2 + \dot{v}_l{}^2\theta^2 + v_l^2\dot{\theta}^2 - 2\dot{\theta} h\theta\dot{v}_l - 2h v_l\dot{\theta}^2 + 2\dot{v}_l\theta v_l\dot{\theta} \\ &+ \dot{v}_c{}^2 + x_l^2\dot{\theta}^2 + \dot{v}_l{}^2 - 2\dot{v}_c\dot{\theta}x_l + 2\dot{v}_c\dot{v}_l - 2\dot{\theta}\dot{v}_l x_l) dx_l \\ =& \frac{1}{2} \rho A_{ml} \int_0^{L_l} (\dot{\theta}^2 h^2 + \dot{v}_c{}^2 + x_l^2\dot{\theta}^2 + \dot{v}_l{}^2 - 2\dot{v}_c\dot{\theta}x_l + 2\dot{v}_c\dot{v}_l - 2\dot{\theta}\dot{v}_l x_l) dx_l, \end{aligned} \tag{3.111}$$

$$\begin{aligned} T_{mr} =& \frac{1}{2} \int_m \overrightarrow{v_{D'}} . \overrightarrow{v_{D'}} dm = \frac{1}{2} \rho A_{mr} \int_0^{L_r} (\dot{\theta} h - \dot{v}_r\theta - v_r\dot{\theta})^2 + (\dot{v}_c + x_r\dot{\theta} + \dot{v}_r)^2 dx_r \\ =& \frac{1}{2} \rho A_{mr} \int_0^{L_r} (\dot{\theta}^2 h^2 + \dot{v}_r{}^2\theta^2 + v_r^2\dot{\theta}^2 - 2\dot{\theta} h\theta\dot{v}_r - 2h v_r\dot{\theta}^2 + 2\dot{v}_r\theta v_r\dot{\theta} \\ &+ \dot{v}_c{}^2 + x_r^2\dot{\theta}^2 + \dot{v}_r{}^2 + 2\dot{v}_c\dot{\theta}x_r + 2\dot{v}_c\dot{v}_r + 2\dot{\theta}\dot{v}_r x_r) dx_r \\ =& \frac{1}{2} \rho A_{mr} \int_0^{L_r} (\dot{\theta}^2 h^2 + \dot{v}_c{}^2 + x_r^2\dot{\theta}^2 + \dot{v}_r{}^2 + 2\dot{v}_c\dot{\theta}x_r + 2\dot{v}_c\dot{v}_r + 2\dot{\theta}\dot{v}_r x_r) dx_r. \end{aligned} \tag{3.112}$$

The simplification of dismissing the terms of order higher than three adopted for the damper counterweight kinetic energies was followed as well for the messenger wires.

Expressing the kinetic energies of the messenger cable in the matricial form,

$$T_{ml} = \frac{1}{2}\rho A_{ml}\int_0^{L_l}(\dot{w_c}^T N_c'^T N_c' \dot{w_c} h^2 + \dot{w_c}^T N_c^T N_c \dot{w_c} + x_l^2 \dot{w_c}^T N_c'^T N_c' \dot{w_c} + \dot{w_l}^T N_l^T N_l \dot{w_l} - 2x_l \dot{w_c}^T N_c^T N_c' \dot{w_c} + 2\dot{w_c}^T N_c^T N_l \dot{w_l} - 2x_l \dot{w_c}^T N_c'^T N_l \dot{w_l}) dx_l, \tag{3.113}$$

$$T_{mr} = \frac{1}{2}\rho A_{mr}\int_0^{L_r}(\dot{w_c}^T N_c'^T N_c' \dot{w_c} h^2 + \dot{w_c}^T N_c^T N_c \dot{w_c} + x_r^2 \dot{w_c}^T N_c'^T N_c' \dot{w_c} + \dot{w_r}^T N_r^T N_r \dot{w_r} + 2x_r \dot{w_c}^T N_c^T N_c' \dot{w_c} + 2\dot{w_c}^T N_c^T N_r \dot{w_r} + 2x_r \dot{w_c}^T N_c'^T N_r \dot{w_r}) dx_r. \tag{3.114}$$

3.3.2 Potential energy

The potential energy for the conductor deformation energy can be obtained through:

$$U = \frac{1}{2}\int_V \sigma \varepsilon dV, \tag{3.115}$$

where:

$$\sigma = E\varepsilon, \tag{3.116}$$

$$\varepsilon = \frac{\partial u}{\partial x} = -z\frac{\partial^2 v}{\partial x^2}, \tag{3.117}$$

$$u = -z\frac{\partial v}{\partial x}. \tag{3.118}$$

Leading to:

$$U = \frac{1}{2}\int_0^{l_c}\int_A z^2 \left(\frac{\partial^2 v}{\partial x^2}\right)^2 E dA dx = \frac{1}{2}EI\int_0^{l_c}\left(\frac{\partial^2 v}{\partial x^2}\right)^2 dx. \tag{3.119}$$

The relation between the deformed length of the conductor and the undeformed length is described as:

$$ds = (dx^2 + dv^2)^{\frac{1}{2}}, \tag{3.120}$$

leading to:

$$ds - dx = \frac{1}{2}\left(\frac{dv}{dx}\right)^2 dx, \tag{3.121}$$

and therefore, the work done by the tension T at which the conductor is strung is:

$$W_T = \frac{1}{2}T\int_0^{l_c}\left(\frac{\partial v}{\partial x}\right)^2 dx. \tag{3.122}$$

The potential energy of the conductor can be described as:

$$V_c = \frac{1}{2}(EI)_c\int_0^{l_c}\left(\frac{\partial^2 v}{\partial x^2}\right)^2 dx + \frac{1}{2}T\int_0^{l_c}\left(\frac{\partial v}{\partial x}\right)^2 dx. \tag{3.123}$$

The potential energy of each of the counterweights can be determined by their position. In order to facilitate the calculation, an approximation is done where the position of each counterweight is considered at each extremity of the messenger cable. Therefore:

$$V_{dl} = m_l \overrightarrow{g}.\overrightarrow{OC} = m_l \begin{Bmatrix} 0 \\ -g \\ 0 \end{Bmatrix} . \begin{Bmatrix} L_c - h\theta - L_l + v_l\theta \\ v_c - h + v_l - L_l\theta \\ 0 \end{Bmatrix}, \tag{3.124}$$

$$V_{dl} = -m_l g(v_c - h + v_l - L_l\theta), \tag{3.125}$$

$$V_{dr} = m_r \overrightarrow{g}.\overrightarrow{OD} = m_r \begin{Bmatrix} 0 \\ -g \\ 0 \end{Bmatrix} . \begin{Bmatrix} L_c + h\theta + L_r - v_r\theta \\ v_c - h + L_r\theta + v_r \\ 0 \end{Bmatrix}, \tag{3.126}$$

$$V_{dr} = -m_r g(v_c - h + L_r\theta + v_r). \tag{3.127}$$

The potential energy of each of the messenger cables is simply an integral throughout the length of the cable and can be described as:

$$V_{ml} = \frac{1}{2}(EI)_{ml} \int_0^{L_l} \left(\frac{\partial^2 v_l}{\partial x^2}\right)^2, \tag{3.128}$$

$$V_{mr} = \frac{1}{2}(EI)_{mr} \int_0^{L_r} \left(\frac{\partial^2 v_r}{\partial x^2}\right)^2. \tag{3.129}$$

The total potential energy can be written as:

$$\begin{aligned} V =& \frac{1}{2}(EI)_c \int_0^{l_c} \left(\frac{\partial^2 v}{\partial x^2}\right)^2 dx + \frac{1}{2}T \int_0^{l_c} \left(\frac{\partial v}{\partial x}\right)^2 dx - m_r g(v_c - h + L_r\theta + v_r) \\ & - m_l g(v_c - h + v_l - L_l\theta) + \frac{1}{2}(EI)_{mr} \int_0^{L_r} \left(\frac{\partial^2 v_r}{\partial x^2}\right)^2 dx_r + \frac{1}{2}(EI)_{ml} \int_0^{L_l} \left(\frac{\partial^2 v_l}{\partial x^2}\right)^2 dx_l, \end{aligned} \tag{3.130}$$

and making the transition to the matricial form,

$$\begin{aligned} V =& \frac{1}{2}(EI)_c \int_0^{l_c} w_c^T N_c^{T''} N_c'' w_c dx_c + \frac{1}{2}T \int_0^{l_c} w_c^T N_c^{T'} N_c' w_c dx_c \\ & - m_r g({w_c}^T {N_c}^T - h + {w_r}^T {N_r}^T + L_r {w_c}^T {N_c'}^T) - m_l g({w_c}^T {N_c}^T - h + {w_l}^T {N_l}^T - L_l {w_c}^T {N_c'}^T) \\ & + \frac{1}{2}(EI)_{mr} \int_0^{L_r} w_r^T N_r^{T''} N_r'' w_r dx_r + \frac{1}{2} \int_0^{L_l} w_l^T N_l^{T''} N_l'' w_l dx_l. \end{aligned} \tag{3.131}$$

3.3.3 Work of the external forces

As the work of the external forces it is only considered the wind excitation on the conductor part of the conductor-damper element with a distributed force of $f(x,t)$. Therefore,

$$W_f = \int_0^{l_c} f(x,t) v_c dx_c, \tag{3.132}$$

that can also be written as,

$$W_f = f(x,t) \int_0^{l_c} w^T {N_c}^T dx_c. \tag{3.133}$$

3.4 Conductor-damper finite element

To obtain the mass and stiffness matrix of the damper element, the Hamilton's Principle was used. Remebering the principle,

$$\int_{t_1}^{t_2} \delta(T - V)dt + \int_{t_1}^{t_2} \delta W_{nc}\, dt = 0. \tag{3.134}$$

3.4.1 Mass matrix

The mass matrix of the damper element is obtained through the kinetic energies previously obtained. To the kinetic energies a variational operation is applied, as seen in the following equations,

$$\delta T_c = \rho A_c \int_0^{l_c} \delta \dot{w}_c{}^T N_c^T N_c \dot{w}_c dx_c, \tag{3.135}$$

$$\begin{aligned}\delta T_{dl} = m_l(&\delta \dot{w}_c{}^T N_c^{'T} N_c' \dot{w}_c h^2 + \delta \dot{w}_c{}^T N_c{}^T N_c \dot{w}_c + L_l^2 \delta \dot{w}_c{}^T N_c^{'T} N_c' \dot{w}_c + \delta \dot{w}_l{}^T N_l{}^T N_l \dot{w}_l \\ &- L_l \delta \dot{w}_c{}^T N_c^T N_c' \dot{w}_c - L_l \delta \dot{w}_c{}^T N_c^{'T} N_c \dot{w}_c + \delta \dot{w}_c{}^T N_c^T N_l \dot{w}_l + \delta \dot{w}_l{}^T N_l^T N_c \dot{w}_c \\ &- L_l \delta \dot{w}_c{}^T N_c^{'T} N_l \dot{w}_l - L_l \delta \dot{w}_l{}^T N_l^T N_c' \dot{w}_c) + J_{dl}(\delta \dot{w}_l{}^T N_l^{'T} N_l' \dot{w}_l + \delta \dot{w}_l{}^T N_l^{'T} N_c' \dot{w}_c \\ &+ \delta \dot{w}_c{}^T N_c^{'T} N_l' \dot{w}_l + \delta \dot{w}_c{}^T N_c^{'T} N_c' \dot{w}_c),\end{aligned} \tag{3.136}$$

$$\begin{aligned}\delta T_{dr} = m_r(&\delta \dot{w}_c{}^T N_c^{'T} N_c' \dot{w}_c h^2 + \delta \dot{w}_c{}^T N_c{}^T N_c \dot{w}_c + L_r^2 \delta \dot{w}_c{}^T N_c^{'T} N_c' \dot{w}_c + \delta \dot{w}_r{}^T N_r{}^T N_r \dot{w}_r \\ &+ L_r \delta \dot{w}_c{}^T N_c^T N_c' \dot{w}_c + L_r \delta \dot{w}_c{}^T N_c^{'T} N_c \dot{w}_c + \delta \dot{w}_c{}^T N_c^T N_r \dot{w}_r + \delta \dot{w}_r{}^T N_r^T N_c \dot{w}_c \\ &+ L_r \delta \dot{w}_c{}^T N_c^{'T} N_r \dot{w}_r + L_r \delta \dot{w}_r{}^T N_r^T N_c' \dot{w}_c) + J_{dr}(\delta \dot{w}_r{}^T N_r^{'T} N_r' \dot{w}_r + \delta \dot{w}_r{}^T N_r^{'T} N_c' \dot{w}_c \\ &+ \delta \dot{w}_c{}^T N_c^{'T} N_r' \dot{w}_r + \delta \dot{w}_c{}^T N_c^{'T} N_c' \dot{w}_c),\end{aligned} \tag{3.137}$$

$$\begin{aligned}\delta T_{ml} = \rho A_{ml} \int_0^{L_l} (&\delta \dot{w}_c{}^T N_c^{'T} N_c' \dot{w}_c h^2 + \delta \dot{w}_c{}^T N_c^T N_c \dot{w}_c + x_l^2 \delta \dot{w}_c{}^T N_c^{'T} N_c' \dot{w}_c + \delta \dot{w}_l{}^T N_l^T N_l \dot{w}_l \\ &- x_l \delta \dot{w}_c{}^T N_c^T N_c' \dot{w}_c - x_l \delta \dot{w}_c{}^T N_c^{'T} N_c \dot{w}_c + \delta \dot{w}_c{}^T N_c^T N_l \dot{w}_l + \delta \dot{w}_l{}^T N_l^T N_c \dot{w}_c \\ &- x_l \delta \dot{w}_c{}^T N_c^{'T} N_l \dot{w}_l - x_l \delta \dot{w}_l{}^T N_l^T N_c' \dot{w}_c) dx_l,\end{aligned} \tag{3.138}$$

$$\begin{aligned}\delta T_{mr} = \rho A_{mr} \int_0^{L_r} (&\delta \dot{w}_c{}^T N_c^{'T} N_c' \dot{w}_c h^2 + \delta \dot{w}_c{}^T N_c^T N_c \dot{w}_c + x_r^2 \delta \dot{w}_c{}^T N_c^{'T} N_c' \dot{w}_c + \delta \dot{w}_r{}^T N_r^T N_r \dot{w}_r \\ &+ x_r \delta \dot{w}_c{}^T N_c^T N_c' \dot{w}_c + x_r \delta \dot{w}_c{}^T N_c^{'T} N_c \dot{w}_c + \delta \dot{w}_c{}^T N_c^T N_r \dot{w}_r + \delta \dot{w}_r{}^T N_r^T N_c \dot{w}_c \\ &+ x_r \delta \dot{w}_c{}^T N_c^{'T} N_r \dot{w}_r + x_r \delta \dot{w}_r{}^T N_r^T N_c' \dot{w}_c) dx_r.\end{aligned} \tag{3.139}$$

To obtain the mass matrix through the sum of the kinetic energies it is necessary to integrate by parts every term, so that the variation of velocity present in each of the terms turns into a variation of displacement. Remembering that,

$$\int_a^b u dv = (uv)|_a^b - \int_a^b v du, \tag{3.140}$$

and knowing that the first term of equation (3.140), which represents the variation at the instants t_1 and t_2 is zero by definition,

$$\delta T_c = \rho A_c \int_0^{l_c} \delta w_c^T N_c^T N_c \ddot{w}_c \, dx_c, \tag{3.141}$$

$$\begin{aligned}\delta T_{dl} = m_l(&\delta w_c^T {N_c'}^T N_c' \ddot{w}_c h^2 + \delta w_c^T {N_c}^T N_c \ddot{w}_c + L_l^2 \delta w_c^T {N_c'}^T N_c' \ddot{w}_c + \delta w_l^T {N_l}^T N_l \ddot{w}_l \\ &- L_l \delta w_c^T N_c^T N_c' \ddot{w}_c - L_l \delta w_c^T {N_c'}^T N_c \ddot{w}_c + \delta w_c^T N_c^T N_l \ddot{w}_l + \delta w_l^T N_l^T N_c \ddot{w}_c \\ &- L_l \delta w_c^T {N_c'}^T N_l \ddot{w}_l - L_l \delta w_l^T N_l^T N_c' \ddot{w}_c) + J_{dl}(\delta w_l^T {N_l'}^T N_l' \ddot{w}_l + \delta w_l^T {N_l'}^T N_c' \ddot{w}_c \\ &+ \delta w_c^T {N_c'}^T N_l' \ddot{w}_l + \delta w_c^T {N_c'}^T N_c' \ddot{w}_c),\end{aligned} \tag{3.142}$$

$$\begin{aligned}\delta T_{dr} = m_r(&\delta w_c^T {N_c'}^T N_c' \ddot{w}_c h^2 + \delta w_c^T {N_c}^T N_c \ddot{w}_c + L_r^2 \delta w_c^T {N_c'}^T N_c' \ddot{w}_c + \delta w_r^T {N_r}^T N_r \ddot{w}_r \\ &+ L_r \delta w_c^T N_c^T N_c' \ddot{w}_c + L_r \delta w_c^T {N_c'}^T N_c \ddot{w}_c + \delta w_c^T N_c^T N_r \ddot{w}_r + \delta w_r^T N_r^T N_c \ddot{w}_c \\ &+ L_r \delta w_c^T {N_c'}^T N_r \ddot{w}_r + L_r \delta w_r^T N_r^T N_c' \ddot{w}_c) + J_{dr}(\delta w_r^T {N_r'}^T N_r' \ddot{w}_r + \delta w_r^T {N_r'}^T N_c' \ddot{w}_c \\ &+ \delta w_c^T {N_c'}^T N_r' \ddot{w}_r + \delta w_c^T {N_c'}^T N_c' \ddot{w}_c),\end{aligned} \tag{3.143}$$

$$\begin{aligned}\delta T_{ml} = \rho A_{ml} \int_0^{L_l} (&\delta w_c^T {N_c'}^T N_c' \ddot{w}_c h^2 + \delta w_c^T N_c^T N_c \ddot{w}_c + x_l^2 \delta w_c^T {N_c'}^T N_c' \ddot{w}_c + \delta w_l^T N_l^T N_l \ddot{w}_l \\ &- x_l \delta w_c^T N_c^T N_c' \ddot{w}_c - x_l \delta w_c^T {N_c'}^T N_c \ddot{w}_c + \delta w_c^T N_c^T N_l \ddot{w}_l + \delta w_l^T N_l^T N_c \ddot{w}_c \\ &- x_l \delta w_c^T {N_c'}^T N_l \ddot{w}_l - x_l \delta w_l^T N_l^T N_c' \ddot{w}_c) dx_l,\end{aligned} \tag{3.144}$$

$$\begin{aligned}\delta T_{mr} = \rho A_{mr} \int_0^{L_r} (&\delta w_c^T {N_c'}^T N_c' \ddot{w}_c h^2 + \delta w_c^T N_c^T N_c \ddot{w}_c + x_r^2 \delta w_c^T {N_c'}^T N_c' \ddot{w}_c + \delta w_r^T N_r^T N_r \ddot{w}_r \\ &+ x_r \delta w_c^T N_c^T N_c' \ddot{w}_c + x_r \delta w_c^T {N_c'}^T N_c \ddot{w}_c + \delta w_c^T N_c^T N_r \ddot{w}_r + \delta w_r^T N_r^T N_c \ddot{w}_c \\ &+ x_r \delta w_c^T {N_c'}^T N_r \ddot{w}_r + x_r \delta w_r^T N_r^T N_c' \ddot{w}_c) dx_r.\end{aligned} \tag{3.145}$$

The total variation of the kinetic energy δT of the damper is the sum of all the variations of kinetic energies previously defined,

$$
\begin{aligned}
\delta T = {} & \delta w_c^T[((\rho A)_c \int_0^{l_c} N_c^T N_c dx_c + m_r(N_c^{'T} N_c' h^2 + N_c^T N_c + L_r^2 N_c'^T N_c' + L_r N_c^T N_c' \\
& + L_r N_c^{'T} N_c) + J_{dr} N_c^{'T} N_c' + m_l(N_c^{'T} N_c' h^2 + N_c^T N_c + L_l^2 N_c'^T N_c' - L_l N_c^T N_c' \\
& - L_l N_c^{'T} N_c) + J_{dl} N_c^{'T} N_c' + (\rho A)_{mr} \int_0^{L_r} (N_c^{'T} N_c' h^2 + N_c^T N_c + x_r^2 N_c^{'T} N_c' \\
& + x_r N_c^T N_c' + x_r N_c^{'T} N_c) dx_r + (\rho A)_{ml} \int_0^{L_l} (N_c^{'T} N_c' h^2 + N_c^T N_c + x_l^2 N_c^{'T} N_c' \\
& - x_l N_c^T N_c' - x_l N_c^{'T} N_c) dx_l) \ddot{w}_c + (m_r(N_c^T N_r + L_r N_c^{'T} N_r) + J_{dr} N_c^{'T} N_r' \\
& + (\rho A)_{mr} \int_0^{L_r} (N_c^T N_r + x_r N_c^{'T} N_r) dx_r) \ddot{w}_r + (m_l(N_c^T N_l - L_l N_c^{'T} N_l) \\
& + J_{dl} N_c^{'T} N_l' + (\rho A)_{ml} \int_0^{L_l} (N_c^T N_l - x_l N_c^{'T} N_l) dx_l) \ddot{w}_l] \\
& + \delta w_r^T[(m_r(N_r^T N_c + L_r N_r^T N_c') + J_{dr} N_r^{'T} N_c' + (\rho A)_{mr} \int_0^{L_r} (N_r^T N_c \\
& + x_r N_r{}^T N_c') dx_r) \ddot{w}_c + (m_r N_r^T N_r + J_{dr} N_r^{'T} N_r' + (\rho A)_{mr} \int_0^{L_r} (N_r^T N_r) dx_r) \ddot{w}_r] \\
& + \delta w_l^T[(m_l(N_l^T N_c - L_l N_l^T N_c') + J_{dl} N_l^{'T} N_c' + (\rho A)_{ml} \int_0^{L_l} (N_l^T N_c \\
& - x_l N_l{}^T N_c') dx_l) \ddot{w}_c + (m_l N_l^T N_l + J_{dl} N_l^{'T} N_l' + (\rho A)_{ml} \int_0^{L_l} (N_l^T N_l) dx_l) \ddot{w}_l)],
\end{aligned}
\tag{3.146}
$$

which can be written in the following form:

$$
\left\{ \begin{array}{c} \delta w_c; \delta w_r; \delta w_l \end{array} \right\}
\left[\begin{array}{ccc} M_{cc} & M_{cr} & M_{cl} \\ M_{rc} & M_{rr} & M_{rl} \\ M_{lc} & M_{lr} & M_{ll} \end{array} \right]
\left\{ \begin{array}{c} \ddot{w}_c \\ \ddot{w}_r \\ \ddot{w}_l \end{array} \right\}. \tag{3.147}
$$

It is important to note that the mass matrix is a 12×12 matrix, due to the fact that the damper element is assembled by three Euler Bernoulli elements. However, due to the completed assembly of the damper element, the number of degrees of freedom goes from 12 to 10, because of the shared node between the left and right messenger.

Each of the values inside the matrix shown above correspond to a 4×4 sub-matrix and are presented below,

$$
\begin{aligned}
M_{cc} = {} & (\rho A)_c \int_0^{l_c} N_c^T N_c dx_c + m_r(N_c^{'T} N_c' h^2 + N_c^T N_c + L_r^2 N_c'^T N_c' + L_r N_c^T N_c' \\
& + L_r N_c^{'T} N_c) + J_{dr} N_c^{'T} N_c' + m_l(N_c^{'T} N_c' h^2 + N_c^T N_c + L_l^2 N_c'^T N_c' - L_l N_c^T N_c' \\
& - L_l N_c^{'T} N_c) + J_{dl} N_c^{'T} N_c' + (\rho A)_{mr} \int_0^{L_r} (N_c^{'T} N_c' h^2 + N_c^T N_c + x_r^2 N_c^{'T} N_c' \\
& + x_r N_c^T N_c' + x_r N_c^{'T} N_c) dx_r + (\rho A)_{ml} \int_0^{L_l} (N_c^{'T} N_c' h^2 + N_c^T N_c + x_l^2 N_c^{'T} N_c' \\
& - x_l N_c^T N_c' - x_l N_c^{'T} N_c) dx_l,
\end{aligned}
\tag{3.148}
$$

$$
M_{cr} = m_r(N_c^T N_r + L_r N_c^{'T} N_r) + J_{dr} N_c^{'T} N_r' + (\rho A)_{mr} \int_0^{L_r} (N_c^T N_r + x_r N_c^{'T} N_r) dx_r, \tag{3.149}
$$

$$M_{cl} = m_l(N_c^T N_l - l_l N_c^{'T} N_l) + J_{dl} N_c^{'T} N_l^{'} + (\rho A)_{ml} \int_0^{L_l} (N_c^T N_l - x_l N_c^{'T} N_l) dx_l, \tag{3.150}$$

$$M_{rc} = m_r(N_r^T N_c + L_r N_r^T N_c^{'}) + J_{dr} N_r^{'T} N_c^{'} + (\rho A)_{mr} \int_0^{L_r} (N_r^T N_c + x_r N_r{}^T N_c^{'}) dx_r, \tag{3.151}$$

$$M_{rr} = m_r N_r^T N_r + J_{dr} N_r^{'T} N_r^{'} + (\rho A)_{mr} \int_0^{L_r} (N_r^T N_r) dx_r, \tag{3.152}$$

$$M_{lc} = m_l(N_l^T N_c - L_l N_l^T N_c^{'}) + J_{dl} N_l^{'T} N_c^{'} + (\rho A)_{ml} \int_0^{L_l} (N_l^T N_c - x_l N_l{}^T N_c^{'}) dx_l, \tag{3.153}$$

$$M_{ll} = m_l N_l^T N_l + J_{dl} N_l^{'T} N_l^{'} + (\rho A)_{ml} \int_0^{L_l} (N_l^T N_l) dx_l, \tag{3.154}$$

$$M_{lr} = M_{rl} = [0]. \tag{3.155}$$

3.4.2 Stiffness matrix and the vector of gravitational forces

The same procedure that was used for the kinetic energy is done for the potential energy. And thus, the variation of the potential energy,

$$\begin{aligned}\delta V = {} & (EI)_c \int_0^{l_c} \delta w_c^T N_c^{T''} N_c{}'' w_c dx_c + T \int_0^{l_c} \delta w_c^T N_c^{T'} N_c{}' w_c dx_c - m_r g(\delta w_c{}^T N_c{}^T + \delta w_r{}^T N_r{}^T \\ & + L_r \delta w_c{}^T N_c^{'T}) - m_l g(\delta w_c{}^T N_c{}^T + \delta w_l{}^T N_l{}^T - L_l \delta w_c{}^T N_c^{'T}) \\ & + (EI)_{mr} \int_0^{L_r} \delta w_r^T N_r^{T''} N_r{}'' w_r dx_r + (EI)_{ml} \int_0^{L_l} \delta w_l^T N_l^{T''} N_l{}'' w_l dx_l,\end{aligned} \tag{3.156}$$

that can be rearranged as:

$$\begin{aligned}\delta V = {} & \delta w_c^T \left((EI)_c \int_0^{l_c} N_c^{T''} N_c{}'' dx_c + T \int_0^{l_c} N_c^{T'} N_c{}' \right) w_c \\ & + \delta w_r^T \left((EI)_{mr} \int_0^{L_r} N_r^{T''} N_r{}'' dx_r \right) w_r + \delta w_l^T \left((EI)_{ml} \int_0^{L_l} N_l^{T''} N_l{}'' dx_l \right) w_l \\ & - m_r g(\delta w_c{}^T N_c{}^T + \delta w_r{}^T N_r{}^T + L_r \delta w_c{}^T N_c^{'T}) \\ & - m_l g(\delta w_c{}^T N_c{}^T + \delta w_l{}^T N_l{}^T - L_l \delta w_c{}^T N_c^{'T}),\end{aligned} \tag{3.157}$$

where:

$$\begin{aligned}\delta W_g = {} & -m_r g(\delta w_c{}^T N_c{}^T + \delta w_r{}^T N_r{}^T + L_r \delta w_c{}^T N_c^{'T}) \\ & - m_l g(\delta w_c{}^T N_c{}^T + \delta w_l{}^T N_l{}^T - L_l \delta w_c{}^T N_c^{'T}),\end{aligned} \tag{3.158}$$

is the work done by the gravity force. Therefore, the stiffness matrix can be obtained by subtracting δW_g to δV, obtaining:

$$\begin{aligned}\delta V_k = \delta w_c^T \left((EI)_c \int_0^{l_c} N_c^{T''} N_c'' dx_c + T \int_0^{l_c} N_c^{T'} N_c' dx_c \right) w_c \\ + \delta w_r^T \left((EI)_{mr} \int_0^{L_r} N_r^{T''} N_r'' dx_r \right) w_r + \delta w_l^T \left((EI)_{ml} \int_0^{L_l} N_l^{T''} N_l'' dx_l \right) w_l,\end{aligned} \tag{3.159}$$

which can be represented in the matricial form as:

$$\left\{ \delta w_c; \delta w_r; \delta w_l \right\} \begin{bmatrix} K_{cc} & K_{cr} & K_{cl} \\ K_{rc} & K_{rr} & K_{rl} \\ K_{lc} & K_{lr} & K_{ll} \end{bmatrix} \begin{Bmatrix} w_c \\ w_r \\ w_l \end{Bmatrix}, \tag{3.160}$$

where:

$$K_{cr} = K_{cl} = K_{rc} = K_{rl} = K_{lc} = K_{lr} = [0], \tag{3.161}$$

$$K_{cc} = (EI)_c \int_0^{l_c} N_c^{T''} N_c'' dx_c + T \int_0^{l_c} N_c^{T'} N_c' dx_c, \tag{3.162}$$

$$K_{rr} = (EI)_{mr} \int_0^{L_r} N_r^{T''} N_r'' dx_r, \tag{3.163}$$

$$K_{ll} = (EI)_{ml} \int_0^{L_l} N_l^{T''} N_l'' dx_l. \tag{3.164}$$

From equation (3.133) it is possible to obtain the equivalent nodal external forces and can be represented as:

$$\delta W_f = f(x,t) \int_0^{l_c} \delta w_c^T N_c^T dx_c, \tag{3.165}$$

and that, extending the process for the remaining of the damper with the purpose to obtain the complete force vector for the entire element,

$$\left\{ \delta w_c; \delta w_r; \delta w_l \right\} \begin{Bmatrix} f_c \\ 0 \\ 0 \end{Bmatrix} \quad \text{with} \quad \{F\} = \begin{Bmatrix} f_c \\ 0 \\ 0 \end{Bmatrix}. \tag{3.166}$$

From equation (3.158) it is possible to express the work of the gravity forces as,

$$\left\{ \delta w_c; \delta w_r; \delta w_l \right\} \begin{Bmatrix} -g(m_r(N_c^T + L_r N_c'^T) + m_l(N_c^T - L_r N_c'^T)) \\ -g m_r N_r^T \\ -g m_l N_l^T \end{Bmatrix} \Leftrightarrow \left\{ \delta w_c; \delta w_r; \delta w_l \right\} \begin{Bmatrix} f_g^c \\ f_g^r \\ f_g^l \end{Bmatrix}, \tag{3.167}$$

where,

$$\{F_g\} = \begin{Bmatrix} f_g^c \\ f_g^r \\ f_g^l \end{Bmatrix}. \tag{3.168}$$

Since δw_c, δw_l and δw_r are arbitrary variations in the interval of the boundaries of the element it is possible to write the following equation.

$$\begin{bmatrix} M_{cc} & M_{cr} & M_{cl} \\ M_{rc} & M_{rr} & M_{rl} \\ M_{lc} & M_{lr} & M_{ll} \end{bmatrix} \begin{Bmatrix} \ddot{w}_c \\ \ddot{w}_r \\ \ddot{w}_l \end{Bmatrix} + \begin{bmatrix} K_{cc} & K_{cr} & K_{cl} \\ K_{rc} & K_{rr} & K_{rl} \\ K_{lc} & K_{lr} & K_{ll} \end{bmatrix} \begin{Bmatrix} w_c \\ w_r \\ w_l \end{Bmatrix} = \begin{Bmatrix} f_c \\ 0 \\ 0 \end{Bmatrix} + \begin{Bmatrix} f_g^c \\ f_g^r \\ f_g^l \end{Bmatrix}, \tag{3.169}$$

that can also be rewritten as,

$$[M_d]\{\ddot{w}\} + [K_d]\{w\} = \{F\} + \{F_g\}, \tag{3.170}$$

where $[M_d]$ represents the mass matrix of the damper and $[K_d]$ the stiffness matrix of the damper. $\{F\}$ is the force applied by the wind and $\{F_g\}$ is the vector of nodal forces from the gravitational forces of the damper.

3.5 FE Model

With both elements formulated, and according to the chosen element discretization, the entirety of the conductor and damper mechanical system is assembled, as exemplified in Figure 3.9.

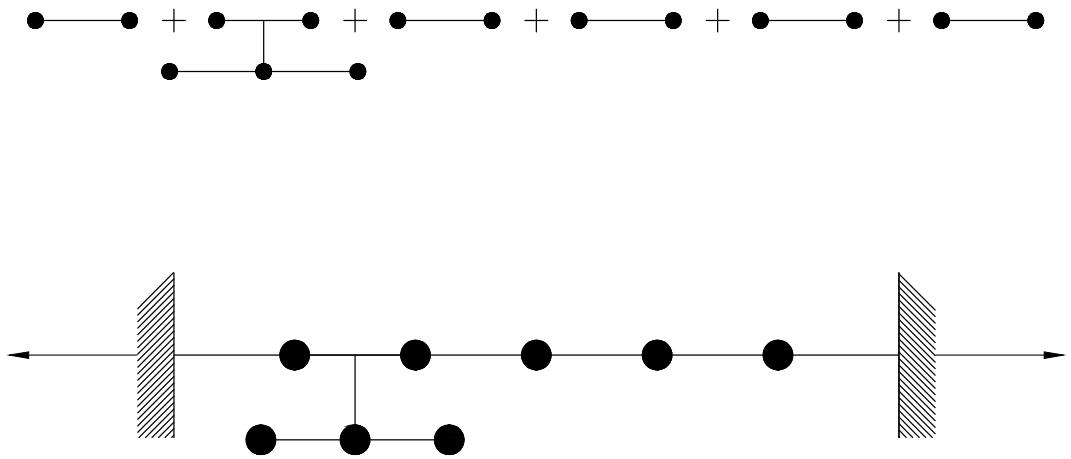

Figure 3.9: Conductor and conductor-damper element assembly.

The mechanical system has the following equation of motion:

$$[M]\{\ddot{w}\} + ([K] + [K_T])\{w\} = \{F(v)\}, \tag{3.171}$$

presenting both the before mentioned stiffness matrices, where [K] depends on the mechanical properties of the conductor and [K_T] depends on the axial tension applied to the conductor.

3.6 Forced vibration analysis

In order to attain the conductor's response throughout time due to aeolian excitation, the Newmark integration method was chosen as the procedure to follow. The Newmark integration method can be considered as an extension of the linear acceleration method. Since this method leads to the solution of $x^{t+\Delta t}$ in the $t + \Delta t$ instant, from the equation of dynamic balance in the $t + \Delta t$ instant, this is a case of an implicit integration method. Since the response only depends on the solution for the previous solution at instant t, this is a method that contains a self-start.

The algorithm for the Newmark method can be described as:

- **Preliminary calculations**

  1. Mechanical properties of the system [M], [K] and [C];
  2. Initial conditions: x^0 and $\dot{x}^0$;

3. Acceleration at the instant $t = 0$: $\ddot{x}^0$

$$[M]\ddot{x}^0 = f^0 - [C]\dot{x}^0 - [K]x^0.$$

4. Time resolution Δt, problem parameters α and δ and the integrations constants;

$$\delta = \frac{1}{2}, \qquad \alpha = \frac{1}{4};$$

$$a_0 = \frac{1}{\alpha(\Delta t)^2}, \quad a_1 = \frac{\delta}{\alpha \Delta t}, \quad a_2 = \frac{1}{\alpha \Delta t}, \quad a_3 = \frac{1}{2\alpha} - 1,$$

$$a_4 = \frac{\delta}{\alpha} - 1, \quad a_5 = \frac{\Delta t}{2}\left(\frac{\delta}{\alpha} - 2\right), \quad a_6 = \Delta t(1-\delta), \quad a_7 = \delta \Delta t.$$

5. Effective stiffness:

$$[\overline{K}] = [K] + a_0[M] + a_1[C].$$

6. Factorization of the effective stiffness $[\overline{K}]$:

$$[\overline{K}] = [L][D][L]^T.$$

- **For each time increment**

1. Effective load at instant $t + \Delta t$:

$$\overline{F}^{t+\Delta t} = F^{t+\Delta t} + [M](a_0 x^t + a_2 \dot{x}^t + a_3 \ddot{x}^t) + [C](a_1 x^t + a_4 \dot{x}^t + a_5 \ddot{x}^t).$$

2. Displacement at the $t + \Delta t$ instant:

$$[\overline{K}]x^{t+\Delta t} = \overline{F}^{t+\Delta t}.$$

3. Acceleration and velocity at instant $t + \Delta t$:

$$\ddot{x}^{t+\Delta t} = a_0(x^{t+\Delta t} - x^t) - a_2 \dot{x}^t - a_3 \ddot{x}^t,$$

$$\dot{x}^{t+\Delta t} = \dot{x}^t + a_6 \ddot{x}^t + a_7 \ddot{x}^{t+\Delta t},$$

where α and δ are specific method parameters. When these values are, respectively, $\frac{1}{4}$ and $\frac{1}{2}$ (values chosen for this thesis work), the method can be considered as unconditionally stable. The value for Δt used was 0.001 s.

Note that both finite element formulations do not account for the existence of any type of a damping matrix, but the influence of damping will also be studied in Chapter 5.2.4.

CHAPTER 4

FE MODEL VALIDATION AND PROGRAM OVERVIEW

With the conductor and conductor-damper models formulated, it was deemed necessary to proceed into a validation procedure before running extensive simulations. To do this, the work of [Barbieri et al., 2004], which has a large amount of experimental data regarding the Ibis type conductors, was chosen as a comparison standard.

In order to perform simulations and study the various types of behaviours of the conductor, it was necessary to create a custom designed Matlab program for this specific case of a beam subjected to axial tension, with the possibility of adding one or more Stockbridge dampers.

This chapter covers the validation of the finite element models and the explanation of the workflow of the program as well as the variables used for the study of the conductor behaviour.

4.1 Free vibration analysis without damper

In this section the various span lengths used by [Barbieri et al., 2004] are retrieved and compared. For this simulation it is considered that the conductor has a simply-supported boundary condition (as considered by the earlier works of transmission line studies, such as [Claren and Diana, 1969]), where an analytical solution for the natural frequencies of vibration taking into account the axial force effect can be determined as:

$$\omega_n = \frac{\pi^2}{L^2}\sqrt{\frac{EI}{\rho A}}\sqrt{n^4 + \frac{n^2 T L^2}{\pi^2 EI}} \qquad n = 1, \ldots, \infty. \tag{4.1}$$

For a conductor with a span lenth L of 13.385 m, a tension T of 15860 N, a mass per unit length ρA of 0.8127 kg/m and a flexural rigidity EI of 11.07 Nm^2 the natural frequency values for the first 5 modes (represented by the letter n in equation (4.1)) are compared with the experimental values obtained by [Barbieri et al., 2004], the analytical solution and the FEM results obtained in the present work. The results are shown in Table 4.1.

The results from the Finite Element Analysis are obtained with a 50 Euler-Bernoulli element discretization. The spacial distribution of each mode is represented on the left side of Figure 4.1. The FEM results here obtained show agreement with analytical and experimental ones.

Table 4.1: Natural frequencies for an Ibis type conductor - simply-supported boundary condition.

L = 13.385 m and T = 15860 N			
Mode	**Natural frequency (Hz)**		
	Experimental [Barbieri et al., 2004]	**Analytical**	**FEM**
1	5.2500	5.2185	5.2185
2	10.4867	10.4376	10.4376
3	15.6562	15.6579	15.6579
4	20.9687	20.8800	20.8800
5	26.1250	26.1046	26.1046

However, some authors like [Vecchiarelli, 1997] and [Barry, 2010] consider the existence of a fixed-fixed boundary condition, where the vertical displacement and the rotations are fixed for each of the span ends. Table 4.2 demonstrates the first five natural modes of vibration for a fixed-fixed condition. The right side of Figure 4.1 presents the first five mode shapes for a conductor with fixed-fixed boundary conditions.

Table 4.2: Natural frequencies for an Ibis type conductor - fixed-fixed boundary condition

L = 13.385 m and T = 15860 N	
Mode	**Natural frequency (Hz)**
	FEM
1	5.2500
2	10.5005
3	15.7522
4	21.0057
5	26.2617

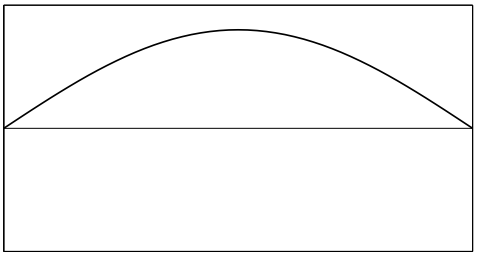

(a) First mode shape - simply-supported.

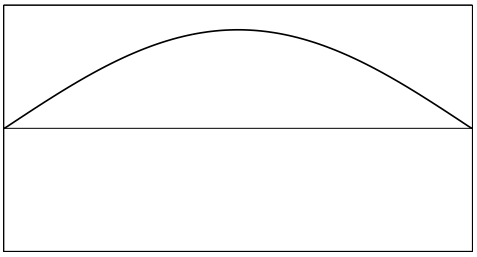

(b) First mode shape - fixed-fixed.

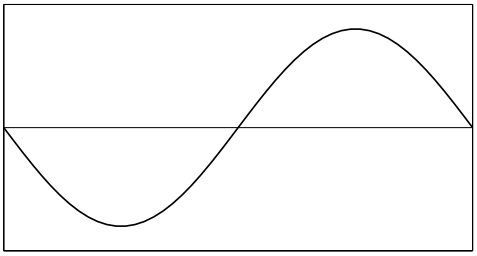

(c) Second mode shape - simply-supported.

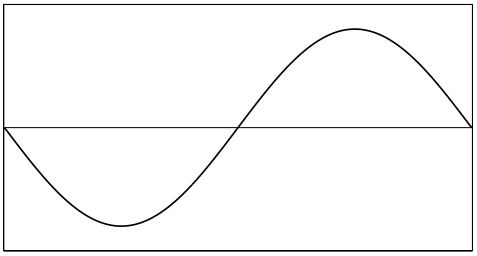

(d) Second mode shape - fixed-fixed.

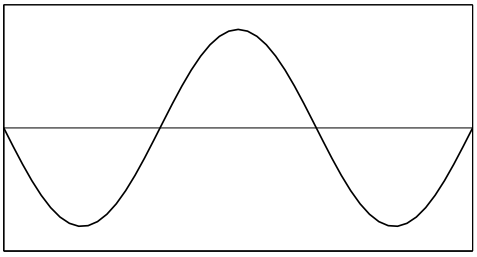

(e) Third mode shape - simply-supported.

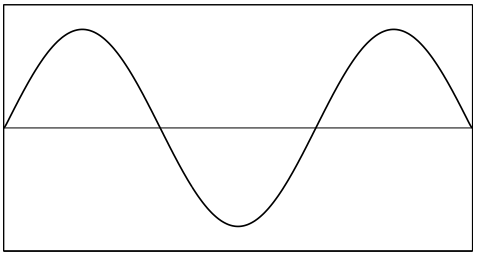

(f) Third mode shape - fixed-fixed.

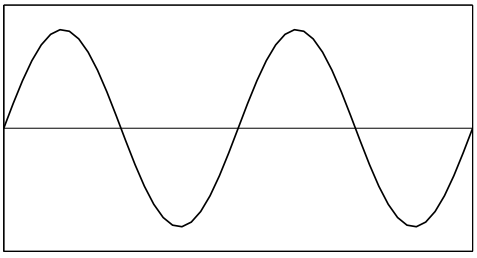

(g) Fourth mode shape - simply-supported.

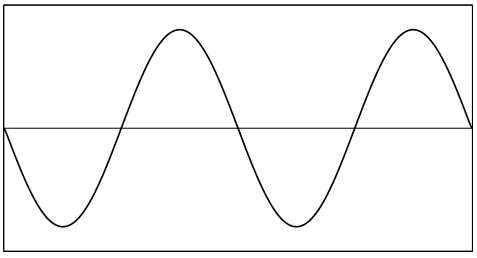

(h) Fourth mode shape - fixed-fixed.

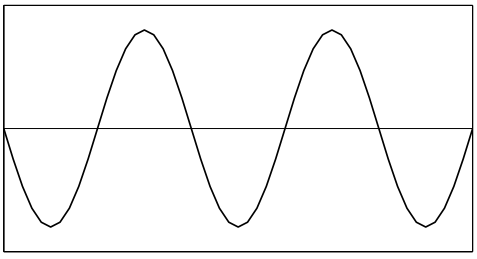

(i) Fifth mode shape - simply-supported.

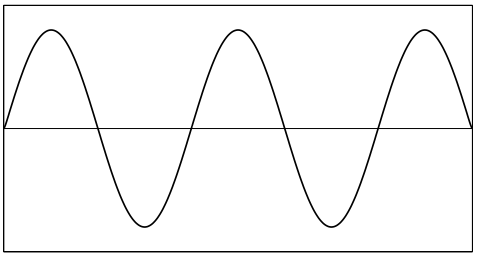

(j) Fifth mode shape - fixed-fixed.

Figure 4.1: Comparison between the first five mode shapes for different boundary conditions.

It is possible to observe from Figure 4.1 and Table 4.2 that even though there is a slight increase in the first five natural frequencies when the boundary conditions are considered as fixed-fixed, the mode shapes do not suffer any type of significant alteration. Both can be explained due to the existence of axial tension on the conductor.

The conductor effectively becomes stiffer. The tension at which the conductor is strung has its influence in a form of a "secondary" stiffness matrix, that adds to the "standard" global stiffness matrix, leading to an increase of the natural frequencies.

To better understand this phenomenon, a comparison between the first three mode shapes for the same conductor is done. The boundary conditions are fixed-fixed. In the first case there is no tension applied to the cable (left side) as opposed to the second case where the conductor is strung with a tension of $T = 15860$ N (right side).

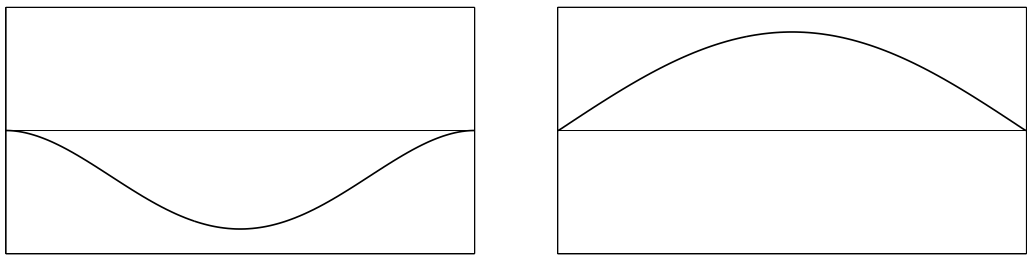

(a) First mode shape - No tension (b) First mode shape - With tension

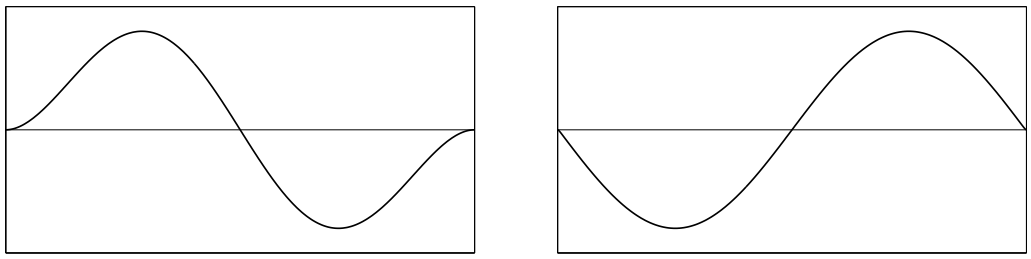

(c) Second mode shape - No tension (d) Second mode shape - With tension

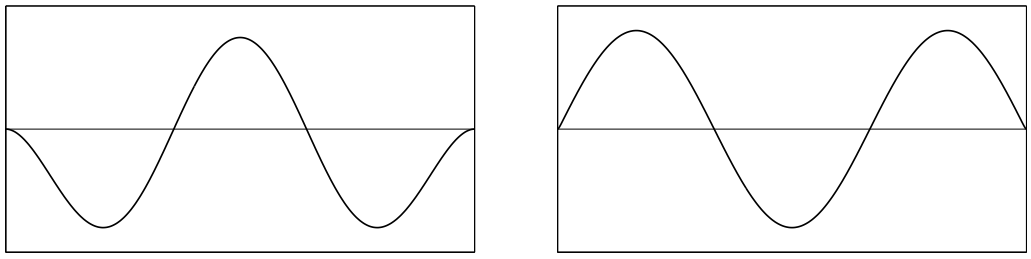

(e) Third mode shape - No tension (f) Third mode shape - With tension

Figure 4.2: Comparison of the first three mode shapes for the Ibis type conductor with fixed-fixed boundary condition for the case of absence and existence of axial tension.

It is therefore clear that the existence of axial tension leads to a considerable difference in the conductor's mode shapes, regardless of making a small difference in the values of natural frequencies.

Resuming the analysis and comparison with the study by [Barbieri et al., 2004], the results for the remaining span lengths for a simply-supported boundary condition are shown in Tables 4.3 and 4.4, which also show little difference between the experimental values, the analytical solution and the

frequencies obtained by the finite element analysis.

Table 4.3: Natural frequencies for an Ibis type conductor - simply-supported boundary condition.

L = 32.300 m and T = 10700 N			
Mode	**Natural frequency (Hz)**		
	Experimental [Barbieri et al., 2004]	**Analytical**	**FEM**
1	1.7813	1.7762	1.7762
2	3.5312	3.5525	3.5525
3	5.2812	5.3289	5.3289
4	7.0312	7.1054	7.1054
5	8.8000	8.8821	8.8821

Table 4.4: Natural frequencies for an Ibis type conductor - simply-supported boundary condition.

L = 63.355 m and T = 15860 N			
Mode	**Natural frequency (Hz)**		
	Experimental [Barbieri et al., 2004]	**Analytical**	**FEM**
1	1.1250	1.0688	1.0688
2	2.0938	2.1375	2.1375
3	3.1562	3.2063	3.2063
4	4.2500	4.2751	4.2751
5	5.2812	5.3439	5.3439

4.2 Free vibration analysis with one damper

For this analysis a similar approach as done by [Barry, 2010] was taken, where a damper is attached at a certain distance L_c from the suspension clamp and the natural frequencies are calculated with an axial tension $T = 0$ N. Then the results are compared with the ones obtained with the commercial software *Ansys* regarding the first ten natural frequencies. The simulation was performed using an Euler-Bernoulli beam element (BEAM4) and a concentrated mass element (MASS21).

The conductor used was the first referenced in Chapter 4.1, with a span length $L = 13.385$ m.

The FEM analysis was done using 50 elements and the correspondent mode shapes were retrieved, in order to demonstrate the effect that the damper has on the conductor. The boundary conditions for this conductor is a fixed-fixed boundary condition (as the works done by [Vecchiarelli, 1997] and [Barry, 2010]), therefore restricting the vertical displacement and the rotation on each span end.

The damper has its characteristics presented in Table 4.5 and it is positioned at $L_c = 4.1$ m. Here and in the following chapters the flexural rigidity (EI_m) and mass per unit length (ρA_m) of the messenger cables of the damper are considered the same, for both sides.

The comparison of values between the *Ansys* results and the FEM analysis is presented in Table 4.6, showing a relatively good agreement between both methods. Six modes shapes are shown in Figure 4.3, where the square markers present in each sub-figure represent the damper location.

Table 4.5: Stockbridge damper properties

Stockbridge damper properties	
$\mathbf{L_l}$ **(m)**	0.2
$\mathbf{L_r}$ **(m)**	0.2
h (m)	0.05
$\boldsymbol{\rho}\mathbf{A_m}$ **(kg/m)**	0.2
$\mathbf{EI_m}$ **(Nm^2)**	3.19
$\mathbf{m_l}$ **(kg)**	2.75
$\mathbf{m_r}$ **(kg)**	4

Table 4.6: Comparison of the first 10 natural frequencies

L = 13.385 m and T = 0 N		
Mode	**Natural frequency (Hz)**	
	Ansys	**FEM**
1	0.0527	0.0529
2	0.1527	0.1536
3	0.3706	0.3730
4	0.6072	0.6120
5	0.8382	0.8427
6	1.2344	1.2478
7	1.5545	1.5843
8	2.0583	2.0739
9	2.3239	2.3749
10	2.8259	2.8571

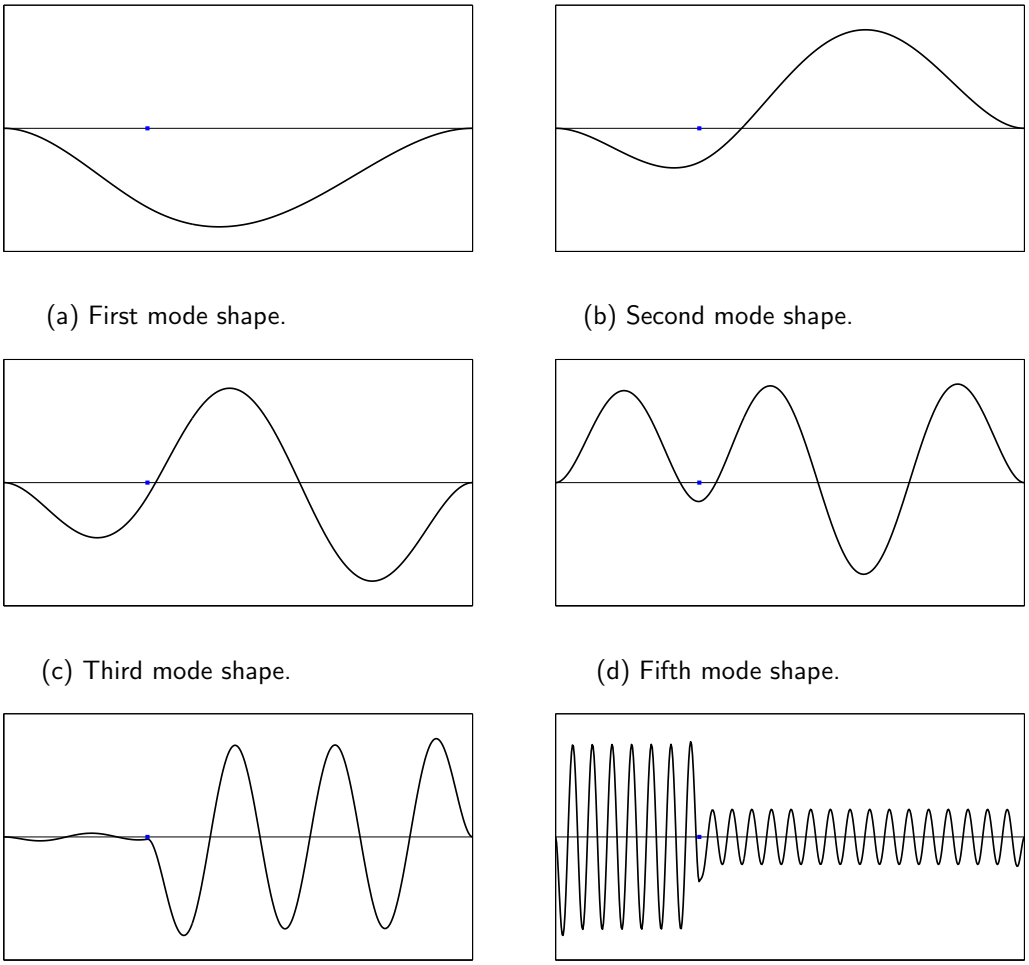

(a) First mode shape.

(b) Second mode shape.

(c) Third mode shape.

(d) Fifth mode shape.

(e) Tenth mode shape.

(f) Fiftieth mode shape.

Figure 4.3: Visual representation of several forms of vibration for the Ibis type conductor with one Stockbridge damper.

It is possible to observe that the usage of a single damper on a conductor with such a small span length ($L = 13.385$ m) has an immediate effect, noticeably on further progressing vibration modes (the 50^{th} mode, for example. It is also possible to observe that, for example, for the tenth and fiftieth mode shape of the conductor, the system conductor-damper effectively reduces the displacement of the conductor, meaning that the system entered a band of frequencies where the damper is indeed more efficient. To further understand the effect of a damper, Table 4.7 presents a comparison of the first 10 natural frequencies, with and without a damper, obtained by FEM, demonstrating a significant difference in natural frequencies when only one damper is applied, which show an obvious and considerable reduction.

Table 4.7: Comparison of the first 10 natural frequencies.

L = 13.385 m and T = 0 N		
Mode	**Natural frequency (Hz)**	
	Without damper	**With damper**
1	0.0734	0.0529
2	0.2022	0.1536
3	0.3964	0.3730
4	0.6553	0.6120
5	0.9789	0.8427
6	1.3672	1.2478
7	1.8202	1.5843
8	2.3381	2.0739
9	2.9206	2.3749
10	3.5680	2.8571

4.3 Program overview

4.3.1 Workflow

The program consists basically of one main program that initializes all the pertinent variables of the problem (such as the mechanical properties of the conductor, the damper, etc) and then, in an orderly fashion, calls various sub-programs to calculate and analyze various types of behaviours.

The program workflow can be broken down into several steps:

- Introduction and initialization of variables in a main document, including the inclusion or not of dampers;
- According to the element discretization of the conductor, the program calls a sub-routine to find the position of the damper (or dampers) element(s) along the conductor. If there is no dampers applied to the conductor, this step does not occur;
- Next, the mass and stiffness elemental matrices are calculated, including the matrices of the conductor-damper element. All the force vectors are created;
- The matrices and vectors previously created are then called into another sub-routine that assembles them accordingly to the information given in the main file;
- After all the matrices and vectors are duely assembled, they are called into a sub-routine that applies the boundary conditions defined. This program allows for both simply-supported boundary conditions, as well as fixed-fixed boundary conditions;
- Then, an eigenvalue problem is conducted in order to obtain the vibration modes, with their corresponding natural frequencies and mode shapes;
- A sub-routine calls the previous results to plot the various mode shapes of the conductor;
- Then, a program calls the initial conditions of the problem and proceeds to calculate the response of the conductor to a forced vibration, recurring to the Newmark integration method;

- All the results for each degree of freedom is retrieved and handled in a specific sub-routine in which various noteworthy node displacements are retrieved and transformed into analysable outputs;
- Finally, all the results pertinent to the problem are plotted.

A simplified version of the program overview can be seen in Figure 4.4.

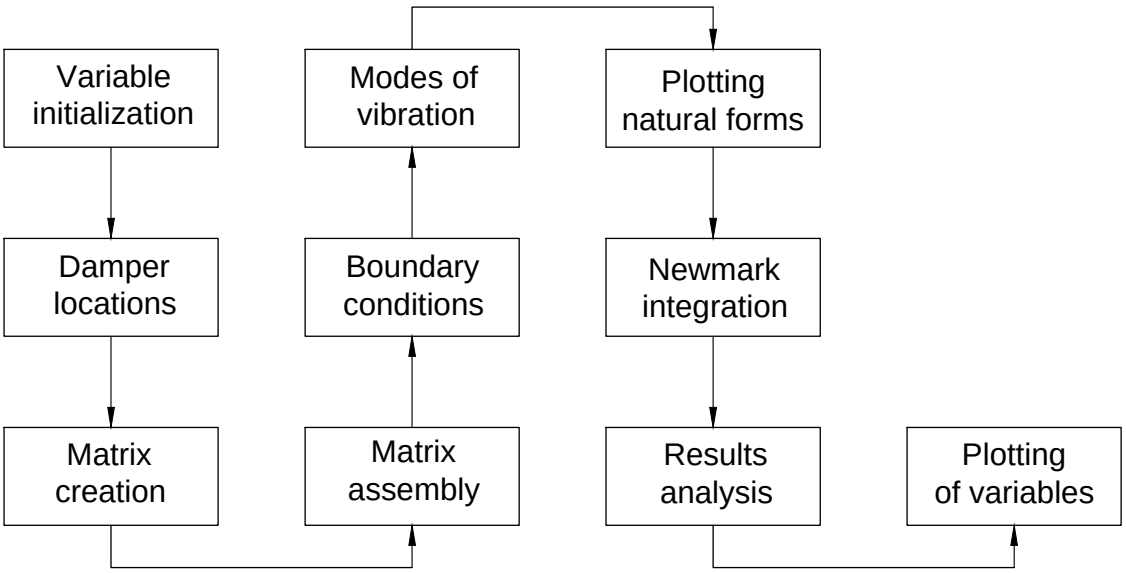

Figure 4.4: Schematic representation of the custom designed Matlab program workflow.

For heavy parametric analysis, another program was built upon the above mentioned, where it essentially calls the main function various times, in order to retrieve various data points related to each of the parameters chosen to analyze.

As previously mentioned, in order to obtain the response of the conductor to a forced vibration state, the Newmark integration method was used.

4.4 Variables overview

This chapter covers the variables used in the study presented in the following chapters, where the study conducted is mainly for the behaviour of the conductor for various states.

For the conductor, four vertical displacements are retrieved for each analysis and they have the following nomenclature:

- The left node vertical displacement y_l;
- The right node vertical displacement y_r;
- The mid-span node vertical displacement y_{mid};
- The node with maximum vertical displacement y_{max}.

The placement of the nodes can be seen in Figure 4.5. Note that the node position with maximum displacement can depend from simulation to simulation and, therefore, is not represented.

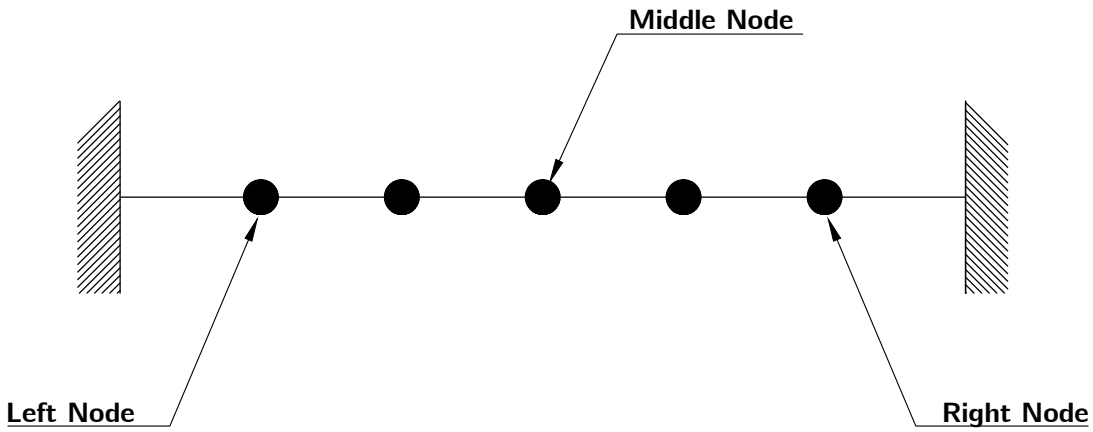

Figure 4.5: Conductor nodes representation.

It is also important to observe that the left and right node are heavily dependent on the element discretization of the problem. The larger the number of elements, the closer the nodes will be from their adjacent suspension clamps, which for simulation purposes may or may not produce relevant results.

The representation of the vertical displacement response can also be in the form of a normalized displacement (normalized by the diameter of the conductor) and has the following form:

$$Y = \frac{y}{D}, \tag{4.2}$$

and in other analysis, the vertical displacement can also be presented in the form of a peak-to-peak normalized displacement, which can be obtained in the following form:

$$\overline{Y} = 2 \times |Y| \,. \tag{4.3}$$

4.5 Concluding remarks

The presented case study and the obtained results allow:

- To validate the FEM formulation and its implementation at the Matlab environment;
- To evidence the axial tension effect on the natural frequencies and mode shapes;
- To evidence the influence of a damper on the natural frequencies and mode shapes of the conductor;
- To observe that the damper has some frequency ranges where its damping properties are more effective.

CHAPTER 5

ACSR CONDUCTOR ANALYSIS

With the model validated, the necessary conditions for a proper parametric analysis of a conductor, with and without a damper, were met. The most common conductor, heavily mentioned throughout the literature, is the ACSR type conductor and the following sections expose the simulation parameters and the results of the various analysis done in the present work.

5.1 General simulation parameters

For this chapter a free vibration simulation is done, as well as a forced vibration analysis, with and without damper, in order to understand the difference in behaviour when dampers are applied.

Therefore it is necessary to define a number of simulation parameters. It is known that a common range of wind speed that causes aeolian vibration is:

$$v = [1 : 7] \text{ m/s}, \tag{5.1}$$

and that the lift force per unit length can be defined as:

$$\frac{F_L}{L} = \frac{1}{2}\rho C_L D v^2. \tag{5.2}$$

The properties of the ACSR conductor are shown in Table 5.1.

Table 5.1: Properties of the ACSR conductor

Conductor properties	
D (m)	0.0219
L (m)	200
ρA (kg/m)	0.987
EI (Nm^2)	[16 : 577]
RTS (N)	86400

Considering the worst case scenario where the value of flexural rigidity EI is minimum, the wind speed is 7 m/s, the air density is 1.2 kg/m^3 and the lift coefficient is 0.3, the value of lift force per unit length results into:

$$\frac{F_L}{L} = 0.193158 \text{ N/m}. \tag{5.3}$$

This force per unit length will be a part of each element force vector present in the finite element formulation. As shown in Table 5.1 the span length considered is 200 m. All simulations present in this chapter are done using 250 Euler-Bernoulli elements (unless stated otherwise) in order to obtain a good amount of element discretization.

Regarding the range of frequencies used it is known also by Chapter 2.2 that the vortex-shredding frequency range can be calculated as:

$$f_{vs} = \frac{c_S V}{D}, \tag{5.4}$$

where the Strouhal coefficient has, usually, a value of about 0.2. Using the range of wind speed presented in Equation (5.1), the range of vortex-shredding frequencies for the ACSR conductor is:

$$f_{vs} = [9.13 : 63.93] \text{ Hz}. \tag{5.5}$$

For these simulations the damper's moment of inertia J_{dr} and J_{dl} are disregarded, as well as the gravitational forces and the time interval used for all of the forced vibration simulations was $20s$.

These are the general parameters used throughout all of the simulations with the final objective of analyzing the behaviour of the conductor bending amplitude. Please note that the variables used to characterize the conductor response were defined at Chapter 4.4.

5.2 Forced vibration without a damper

For a forced vibration it was considered the harmonic type solicitation from the wind to the conductor, similar to what was proven by [Diana and Falco, 1971]. The initial displacement and velocity conditions were considered null for all the degrees of freedom of the conductor.

5.2.1 Simulation with constant axial tension and varying frequency

The purpose of this simulation was to see the behaviour of the conductor when subjected to various excitation frequencies. For that, a constant percentage of the RTS was chosen, of 25%, meaning that the conductor would be strung at a tension of 21600 N. This decision falls within the acceptable range described by the literature.

Three simulations at three different frequencies were done. The first and last simulations correspond to the frequency modes that fall within the lower and upper limits of the vortex-shredding frequency range, with the 25$^{\text{th}}$ mode ($f_{25} = 9.26$ Hz) as the first simulation frequency and the 172$^{\text{nd}}$ mode ($f_{172} = 63.89$ Hz) as the last simulation frequency. A mid-range mode was chosen as well, the 99$^{\text{th}}$ mode with a frequency $f_{99} = 36.68$ Hz. The mode shapes for each of the modes of vibration are represented in Figure 5.1. The results for the forced vibration simulation are presented in Figure 5.2.

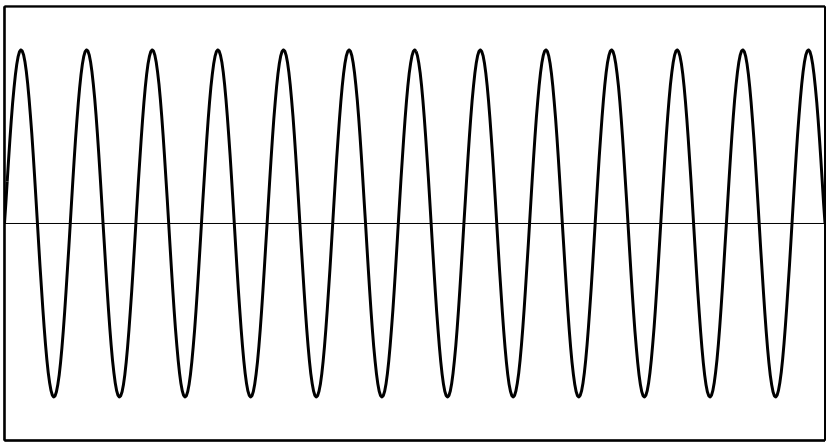

(a) 25^{th} mode shape.

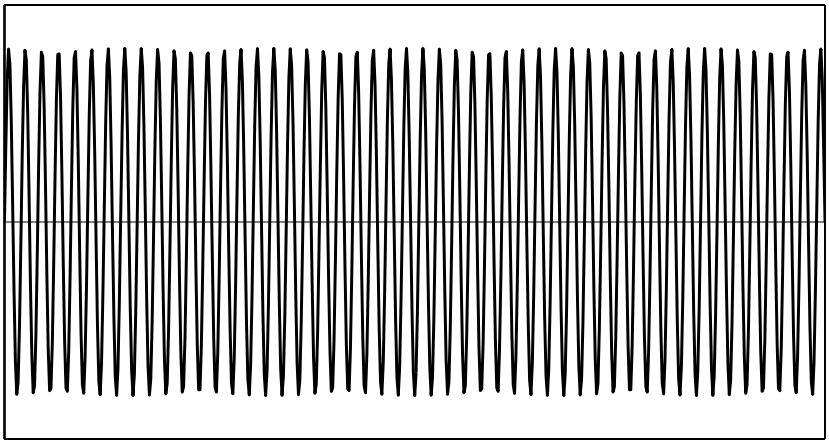

(b) 99^{th} mode shape.

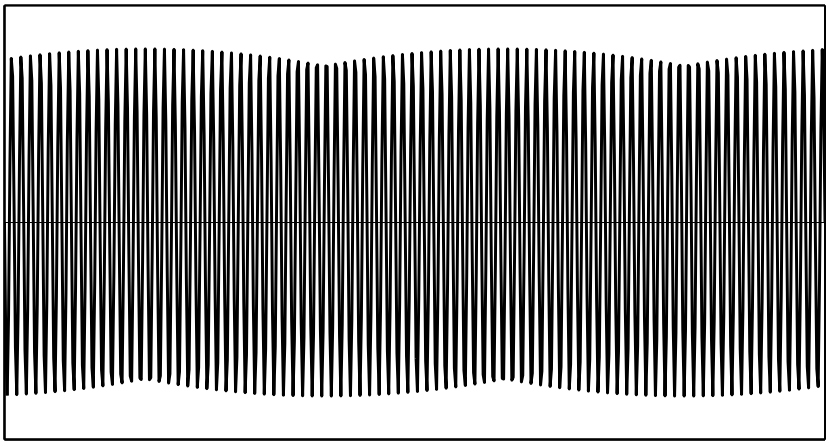

(c) 172^{nd} mode shape.

Figure 5.1: Visual representation of the various mode shapes.

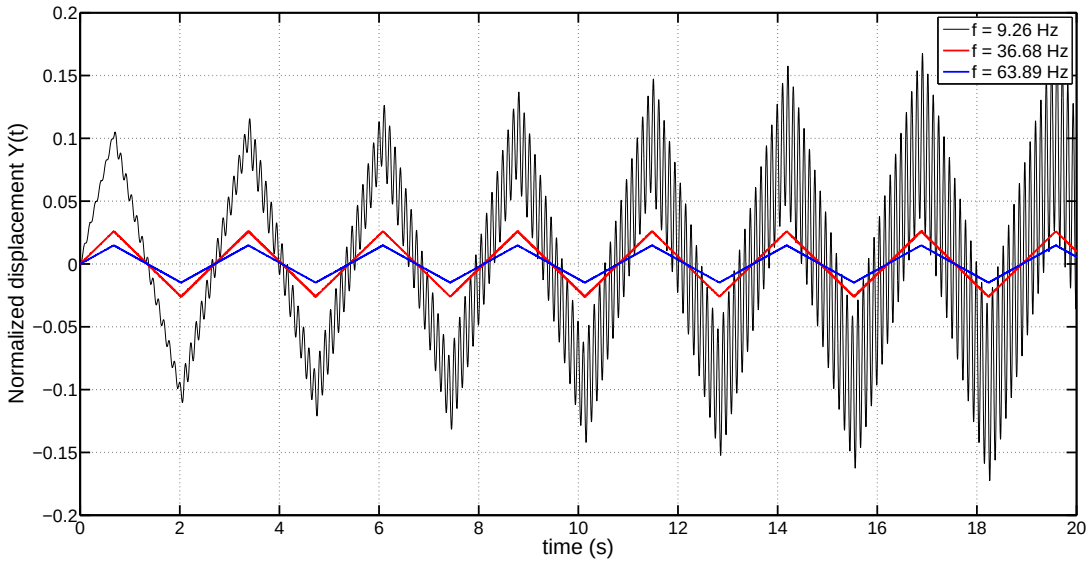

Figure 5.2: Normalized displacement of the node with maximum displacement for constant axial tension and varying excitation frequency.

It can be seen that for the first frequency that falls within the vortex-shredding frequency range, the maximum normalized displacement is much larger than the rest of the modes used for simulation purposes. To better comprehend the reduction of displacement, Table 5.2 shows the peak-to-peak normalized displacements of the various nodes of the conductor for the different modes of vibration.

Table 5.2: Values of peak-to-peak normalized displacements of the conductor for constant axial tension and varying frequencies

ACSR conductor with T = 25 % RTS = 21600 N				
Mode	**Peak-to-peak normalized displacements**			
	$\overline{Y_{max}}$	$\overline{Y_{mid}}$	$\overline{Y_l}$	$\overline{Y_r}$
25	0.20974	0.20974	0.00592	0.00592
99	0.05241	0.05241	0.00152	0.00152
172	0.02958	0.02958	0.00062	0.00062

It is important to take into consideration that for the behaviour of the response with $f = 9.26$ Hz, where the displacement grows significantly in a short span of time, the displacements considered were only the ones retrieved for an interval of time up to 1.5 s. This is due to the lack of damping but the phenomenon will be explained further.

To no surprise, given the symmetry of the conductor, the left node and the right node present identical values of displacement. The node with maximum displacement and the mid-span node appear to be the same.

Another important thing to note is that when passing from the first frequency that falls within the range of vortex-shredding to a mode that falls mid-range, the values of the maximum displacement node and both the left and right node decrease 75% and 79.4%, respectively. However, when passing from the mid-range frequency to the last frequency of the range the decrease in value of the maximum node is only 43.6% and for the left and right node is 59.2%. Therefore, the rate at which the displacement of the nodes decrease also decreases as the forcing frequency increases. This serves to

prove that in terms of risk of fatigue damage due to the displacement of the nodes, the conductor is in danger when the forcing frequencies are lower.

As a final remark, it is visible from Figure 5.2 that for all modes of vibration, which have different forcing frequencies, they all apparently have the same period. Remembering the relationship between the period P and frequency f,

$$P = \frac{1}{f}, \tag{5.6}$$

it is clear to understand that Figure 5.2 should present lower periods for each of the ordered simulations. However, this does not occur due to the simple fact that the formulation of the problem does not contain any type of damping. The equation of motion of the conductor formulated in Chapter 3 presents itself as:

$$[M]\{\ddot{w}\} + ([K] + [K_T])\{w\} = \{F\}. \tag{5.7}$$

Since there is no actual damping matrix (which explains the ever-growing behaviour of the response for $f = 9.26$ Hz), the response of the conductor will always be an overlay of two components: the transient component and the stationary component. The transient component is essentially the first mode of vibration for the given conditions of the simulation which, in this case, has a frequency $f_1 = 0.370$ Hz that leads to a period of approximately $P_1 = 2.703$ s, which shows agreement with the behaviour of the responses shown in Figure 5.2. Therefore, it can be said that the first mode of vibration is the dominant mode, contrary to what was considered in [Vecchiarelli, 1997].

The stationary component is related to the forcing frequency at which the system is excited. Considering the case where the forcing frequency is equals to the 25^{th} mode of vibration, the period would lead to $P_{25} = 0.108$ s which can be seen further in time in the simulation, where there is a noticeably more oscillating behaviour of the displacement of the conductor, leading to two distinct and superposed harmonic movements. This phenomenon will be further explored in Chapters 5.2.3 and 5.2.4.

5.2.2 Simulation with constant frequency and varying axial tension

For this simulation the 25^{th} mode of vibration was chosen since it was the one that presented higher values of displacement. Three different cases were considered for these simulations. The conductor is subjected to three different axial tensions: the first case the cable is strung at 15% of the RTS; the second case the cable is strung at 25% of the RTS; the last case the conductor is strung at 35% of the RTS. The simulation results are shown in Figure 5.3, for the maximum displacement node.

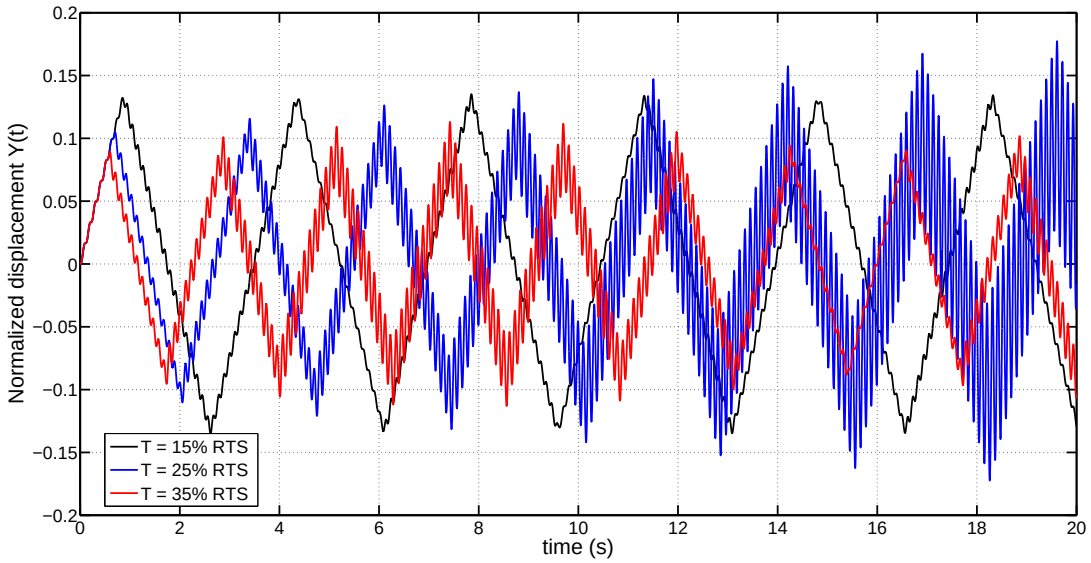

Figure 5.3: Evolution of the node with maximum displacement for a constant frequency of $f = 9.26$ Hz and varying axial tension.

It is possible to observe that, in the initial instants of the movement, the conductor amplitude increases as the conductor tension decreases. However, as time goes on, the response of the conductor for an axial tension of 25% increases significantly while the others do not, or not as significantly. This is due to the fact that the forcing frequency is only a resonance frequency of the second case and, since there is no damping, the steady-state response due to the resonant mode will gradually increase throughout time.

Another noticeable phenomenon is the fact that the response appears to have different periods for each case, contrarily to what happens in the case presented in Figure 5.2. This can also be explained due to axial tension variation. It was said previously that the first mode of vibration was the dominant one and that the most visibly depicted period would be the one corresponding to the first mode of vibration (note that these movements have an overlay of at least 2 modes of vibration).

Since the effect of the axial tension on the conductors is on the stiffness matrix of the system, when decreasing the axial tension on a conductor, the conductor effectively becomes less rigid, making it more susceptible to have larger displacements, when excited, and vice-versa.

Therefore, when a change of stiffness occurs in the conductor, the entire spectrum of natural frequencies changes as well. For the first case the first natural frequency is $f = 0.287$ Hz, for the second case $f = 0.370$ Hz and for the third case $f = 0.438$ Hz. This will lead for a first mode period of 3.484, 2.703 and 2.283 seconds for each of the cases, respectively, which show agreement with the information given in Figure 5.3. Table 5.3 shows the values of $\overline{Y}$ for the relevant nodes for each of the cases.

Table 5.3: Values of peak-to-peak normalized displacements of the various nodes of the conductor for varying axial tensions and constant frequency

ACSR conductor with f = 9.26 Hz				
Tension	**Peak-to-peak normalized displacements**			
	$\overline{Y_{max}}$	$\overline{Y_{mid}}$	$\overline{Y_l}$	$\overline{Y_r}$
15% RTS	0.26604	0.26604	0.00462	0.00462
25% RTS	0.20974	0.20974	0.00592	0.00592
35% RTS	0.17868	0.17868	0.00497	0.00497

What was mentioned previously can quantitatively be observed in Table 5.3, where the values of $\overline{Y_{max}}$ decrease as the conductor becomes effectively stiffer. Going from the first to the third case, it is also noticeable that as the maximum displacement decreases, the left and right node displacement effectively increases. In this analysis, the second case was disregarded as the forcing frequency was one of the resonant frequencies of the system, as pertaining for the left and right node.

5.2.3 Mode overlay analysis

There are many things to take into consideration in the interpretation of each of the results of the previous simulations. It is important to note that this type of analysis does not account for any type of "actual damping" in the form of an introduction of a damping matrix in the equation of motion, since it is only accounted the mass and stiffness matrix. A "true" representation of the equation of motion of the system would be:

$$[M]\{\ddot{w}\} + [C]\{\dot{w}\} + ([K] + [K_T])\{w\} = \{F\}, \tag{5.8}$$

where [C] would represent the equivalent viscous damping of the conductor, interpolated from the study of the damping of the conductor. Therefore, in every analysis where the normalized displacement is shown, there is always an overlay of two modes of vibration. There is an overlay of the first mode of vibration that has a very low frequency with the actual mode of vibration that has a much higher frequency of vibration (n^{th} mode of vibration), as exemplified in Figure 5.4.

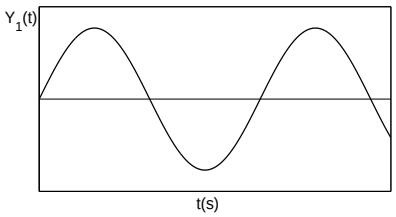

(a) First mode response.

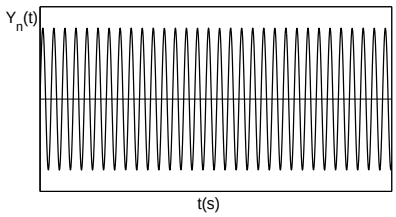

(b) n^{th} mode response.

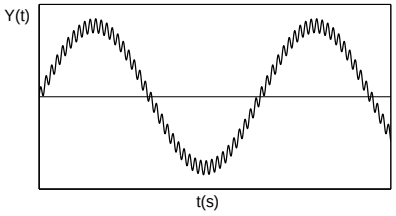

(c) Overlayed response.

Figure 5.4: Visual interpretation of the overlay of natural modes of vibration.

Note that, from a practical standpoint, this does not occur perpetually. Since there is always some form of damping, the influence of the first mode of vibration will be gradually dissipated throughout time, resulting in the existence of only the response of the n^{th} mode frequency.

The amplitude of displacement will be naturally lower than the ones obtained when the influence of the first modes of vibration are present. However, given that the wind not always enters a steady-state condition, the influence of the first modes of vibration are of great importance since it can occur various times throughout the conductor life-span, increasing the probability of serious fatigue damage.

In Figure 5.5 it is represented the maximum normalized displacement for the case presented in Chapter 5.2.1, where an axial tension of 25% of the RTS is used with a forcing frequency of $f = 9.26$ Hz.

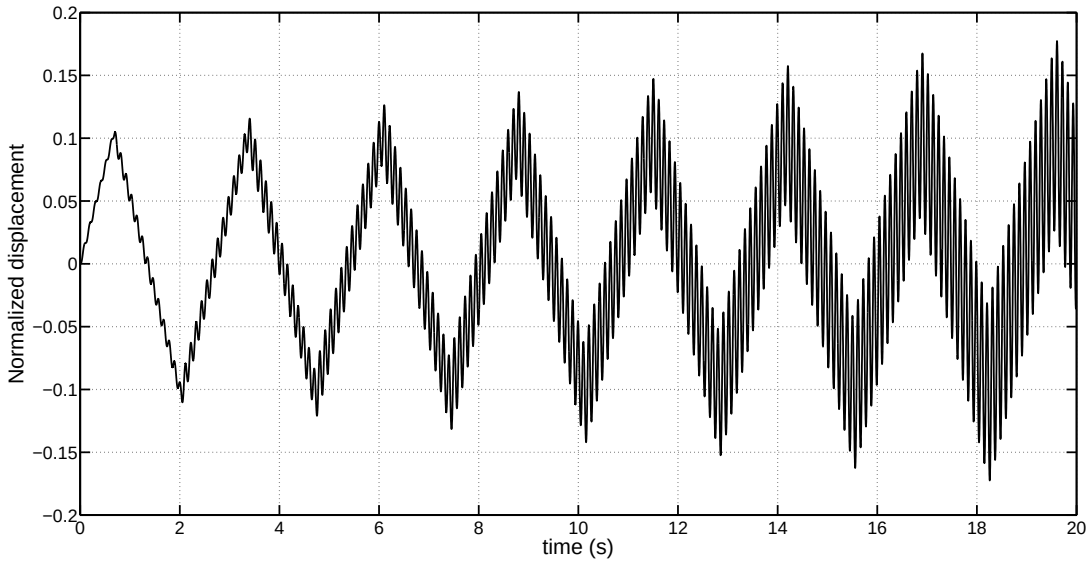

Figure 5.5: Normalized displacement of the node with maximum displacement for a tension of 25% RTS and $f = 9.26$ Hz.

Since damping is not considered and the forcing frequency is a resonance frequency, the maximum displacement will gradually increase. These values cannot be considered for analysis purposes. Therefore, the response of worst case scenario used for behaviour comparisons when dampers are used (starting in Chapter 5.3) is the first maximum value registered in the conductor response.

Note that this value of displacement also does not occur from a practical standpoint. But, in the process of designing any mechanical system, a worst case scenario has to be considered in order to account for any type of safety factor in the movement which, in this case, means considering the first maximum value of displacement of a non-damped response.

Considering this point also means that the condition of steady-state flow of the wind is not considered, in principle, so that it is possible to consider larger displacements.

5.2.4 Introduction of virtual damping

This chapter tries to demonstrate the performance of the conductor when damping is considered. For simulation purposes a viscous damping matrix [C] was created with an high value of damping ratio for the first two modes, in order to quickly obtain the steady-state, stationary response of the maximum displacement node of the conductor. This matrix has exaggerated values on purpose with the objective of reducing simulation times, with a damping ratio of 90 and 95 % for the first two modes, respectively.

Considering again the case where a conductor is strung at 25% of the RTS, with a forcing frequency of $f = 9.26$ Hz and with viscous damping, the normalized maximum response is illustrated at Figure 5.6.

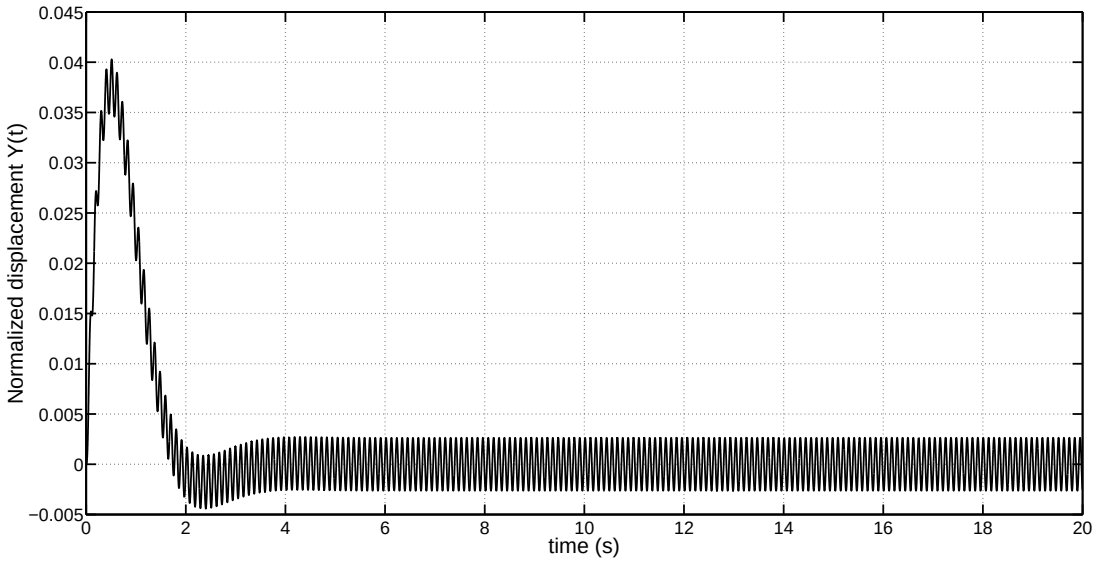

Figure 5.6: Evolution of the damped response of the node with maximum displacement.

It is possible to observe that the maximum displacement response very quickly loses the influence of the first mode of vibration and goes on into the steady-state response, which is initiated at around the 4 s mark. Figure 5.7 presents the movement at only a steady-state stationary motion within the 14 and 20 s marks.

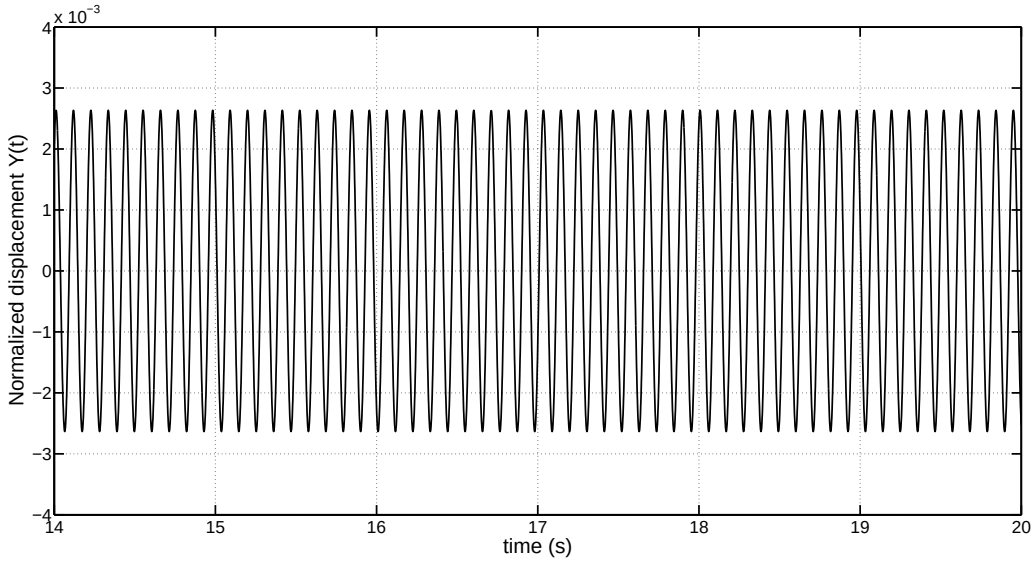

Figure 5.7: Steady-state damped response of the node with maximum displacement.

Given that now the dominant and only mode of vibration is the 25^{th} mode, the period of the

steady-state movement should be:

$$P_{25} = \frac{1}{9.26} \approx 0.108 \text{ s}, \tag{5.9}$$

which shows agreement with what is shown in Figure 5.7. Another thing to take into consideration is that the values of displacement presented in the previous Figure 5.7 are significantly lower than the ones presented in the earlier chapters, proving that the first mode or modes of vibration lead to larger displacement values. Figures 5.8 and 5.9 show a comparison between the behaviour of the displacement amplitude throughout the conductor span when no damping is applied and when damping is present.

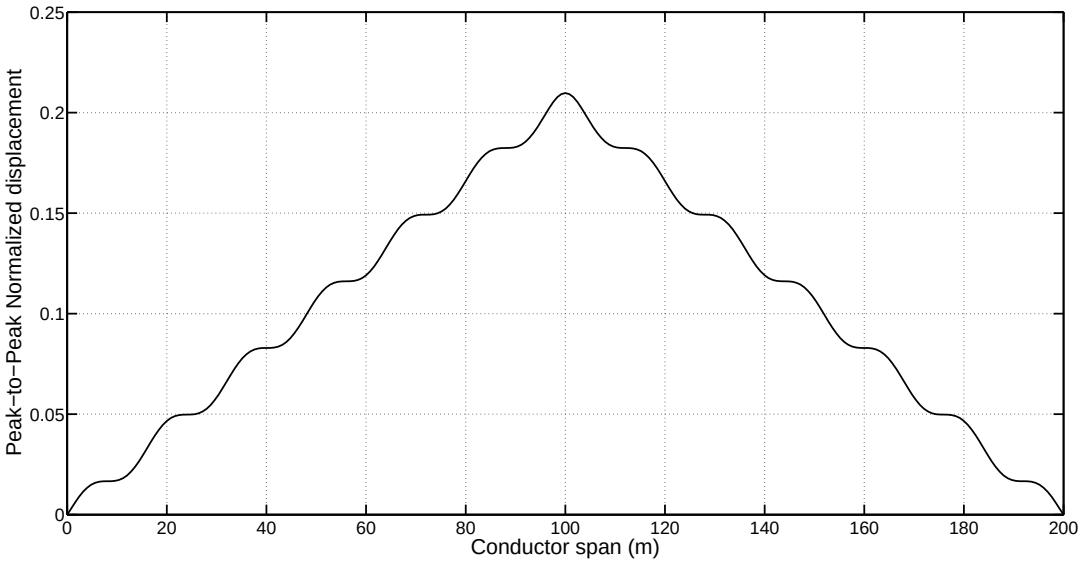

Figure 5.8: Amplitude of the conductor span when no damping is considered.

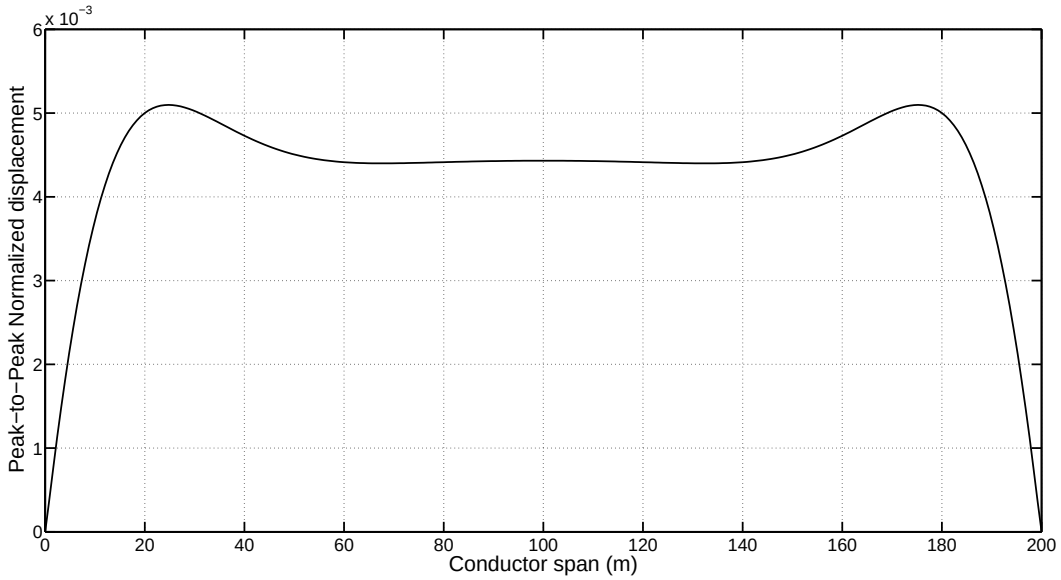

Figure 5.9: Amplitude of the conductor span when damping is considered.

It is evident that when the movement enters a steady-state regime, the maximum displacement of the conductor goes from being the node presented at the middle to the nodes near the suspension clamps, showing agreement with the results presented by [Vecchiarelli, 1997] for a taut string.

5.3 Forced vibration with one damper

5.3.1 Influence of symmetry or asymmetry of the damper counterweights

For this simulation one frequency was chosen, the first that falls within the vortex-shredding frequency range, which means the 25th mode of vibration with a frequency of $f_{25} = 9.26$ Hz.

This section tries to demonstrate the influence of the introduction of a single Stockbridge damper. It is known that the damper can have various counterweight combinations. However one of the most important factors is also the location of the damper within the conductor.

Considering that there is no damping in the simulation program, leading to the overlay of the 1st form with the nth mode of vibration (in this case $n = 25$), it was visible from previous analysis that the 1st mode is the dominant mode, with a much lower forcing frequency and that consequently leads to a much larger loop length.

Remembering that the loop length γ can be defined as:

$$\gamma_n = \frac{L}{n}, \tag{5.10}$$

where, L represents the conductor span length and n is the mode number at which the conductor is excited. For the 25th mode, the loop length results into:

$$\gamma_{25} = 8 \text{ m}, \tag{5.11}$$

which means that if the first mode of vibration wasn't considered the antinode of the conductor would be located at half of the loop length, at $x = 4$ m for the 25th mode, where the damper should be positioned to more efficiently reduce the vibration amplitude.

Even before the results of the simulations have shown one fact immediately stands out: when a damper is positioned at a certain distance from the suspension clamp, its damping properties are not ideal for the entire range of frequencies. Therefore, the damper must be positioned in order to reduce the movement of the mode which gives the largest displacement.

It is also clear that, since the 1st mode of vibration is dominant, considering the loop length of the first mode would lead to a much larger value of x, making it impossible to place the damper at such a distance from the clamp, since a normal range of practical values to position the damper is between 0.5 to 5 meters from the clamp. Therefore, for simulation purposes it is considered the loop length of the 25th mode, since it is the one that actually falls within the vortex-shredding frequency range.

The Stockbridge damper properties used in the simulations are shown in Table 5.4.

Table 5.4: Stockbridge damper properties

Stockbridge damper properties	
$\mathbf{L_l}$ **(m)**	0.2
$\mathbf{L_r}$ **(m)**	0.2
h (m)	0.05
$\boldsymbol{\rho}\mathbf{A_m}$ **(kg/m)**	0.498
$\mathbf{EI_m}$ **(Nm^2)**	3.19
$\mathbf{m_l}$ **(kg)**	[1 : 3]
$\mathbf{m_r}$ **(kg)**	[1 : 3]

For the simulations four cases are considered:

- Case 1 - Forced vibration with no dampers applied;
- Case 2 - Forced vibration with a symmetrical damper where $m_r = m_l = 2$ kg;
- Case 3 - Forced vibration with an asymmetrical damper where $m_r = 3$ kg and $m_l = 1$ kg;
- Case 4 - Forced vibration with an asymmetrical damper where $m_r = 1$ kg and $m_l = 3$ kg.

These cases are meant to show the conductor behaviour when subjected to various types of damper mass distributions, but with constant total damper mass, in this case a total mass of 4 kg. Figure 5.10 compares all the cases showing the values of $\overline{Y}$ of the conductor span.

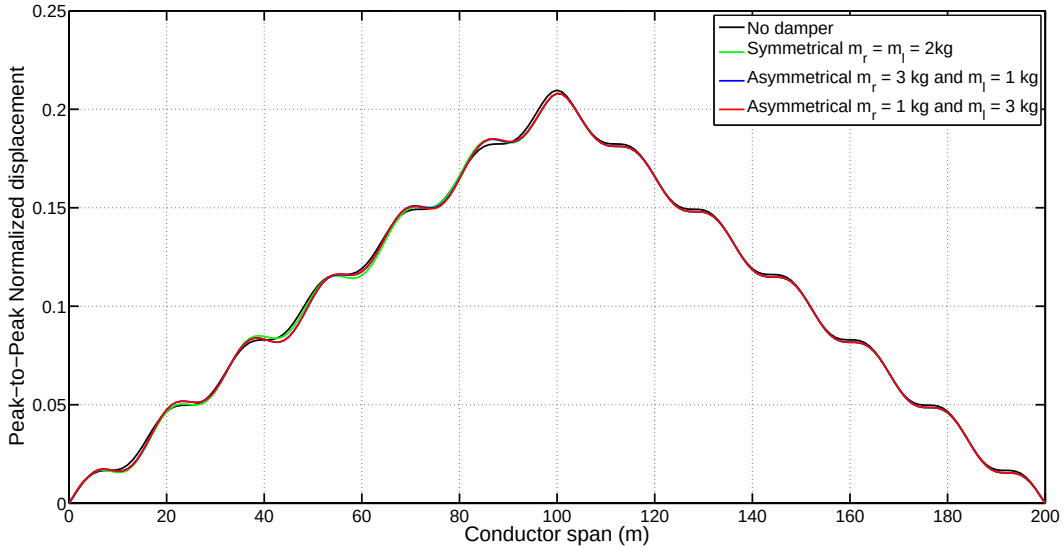

Figure 5.10: Values of displacement for the various cases throughout the conductor span.

It is possible to observe that changes in the conductor displacement aren't significant when one damper is applied, reluctantly of the damper mass distribution. Figure 5.11 demonstrates the difference of the maximum node displacement, presented at mid-span.

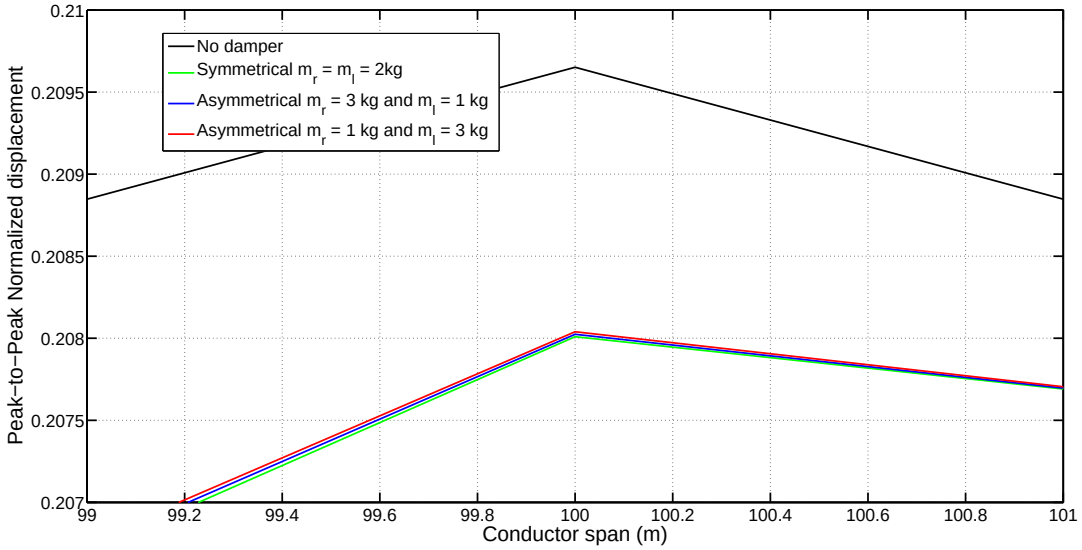

Figure 5.11: Values of displacement for the various cases for a specific conductor span.

This span interval is one of the intervals where the damper most notably reduces the vibration, but not to a great amount. From a visual standpoint, the symmetrical damper proves to be the one with largest reduction, followed by the asymmetrical damper from the third case and then by the fourth case, even though there aren't any significant differences between the cases with damper, as seen in Table 5.5.

Table 5.5: Values of the various noteworthy nodes for the various cases

ACSR conductor with f = 9.26 Hz				
Case	**Peak-to-peak normalized displacements**			
	$\overline{Y_{max}}$	$\overline{Y_{mid}}$	$\overline{Y_l}$	$\overline{Y_r}$
1	0.20974	0.20974	0.00592	0.00592
2	0.20801	0.20801	0.00637	0.00593
3	0.20801	0.20801	0.00604	0.00592
4	0.20801	0.20801	0.00612	0.00610

Even though graphically it appears that the symmetrical damper has a slight advantage relative to the other damper configurations, it is possible to see in Table 5.5 that the difference in value is not noticeable.

Regarding the left node displacement, the side where the damper is applied, note an increase when a symmetrical damper is applied when comparing to a damperless case. For the third case, where the right counterweight is effectively larger, the left node displacement is larger than the damperless case but lower than the second case, with a symmetric damper.

The fourth case, where the left counterweight has the largest mass, the reduction of the displacement on the left node is less noticeable when compared to the other asymmetrical mass distribution, but still with lower values than with a symmetrical damper.

For the right node there is no significant difference in the displacement behaviour in order to have any type of structured conclusion.

The minimal difference between the cases doesn't yet prove what type of damper configuration is the best for reducing aeolian vibration, in exception for the left and right node, which may not prove as important as the node with maximum displacement, since they heavily depend on the element discretization. These nodes can, however, give an idea on how the span sides will behave when dampers are applied.

5.3.2 Simulation with varying frequency

For this type of simulation the forcing frequency of the system is varied within the vortex-shredding frequency range for all the 4 cases previously mentioned. Figure 5.12 demonstrates the evolution of the maximum displacement node for the frequency range considered.

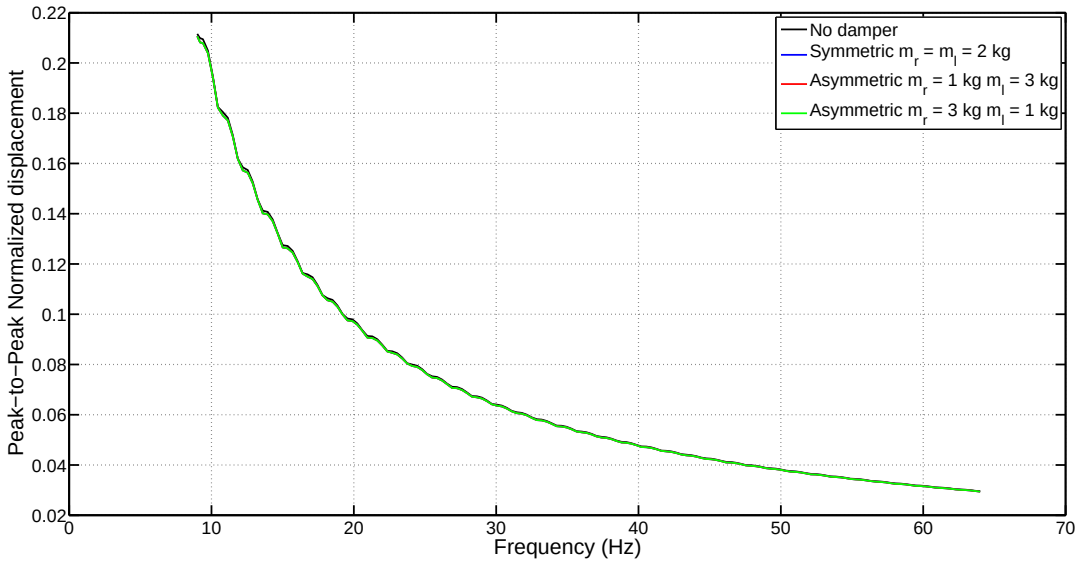

Figure 5.12: Maximum displacement for the various cases for varying forcing frequency.

As shown in previous simulations, the usage of a single damper does not prove to be much effective in reducing aeolian vibration. One of the biggest differences has proven to be in the vicinity of the forcing frequency of 9.26 Hz, as shown in Figure 5.13, where the largest displacement variation of the maximum displacement node is presented. It is also visible from Figure 5.12 that as the forcing frequency increases the maximum displacement amplitude decreases.

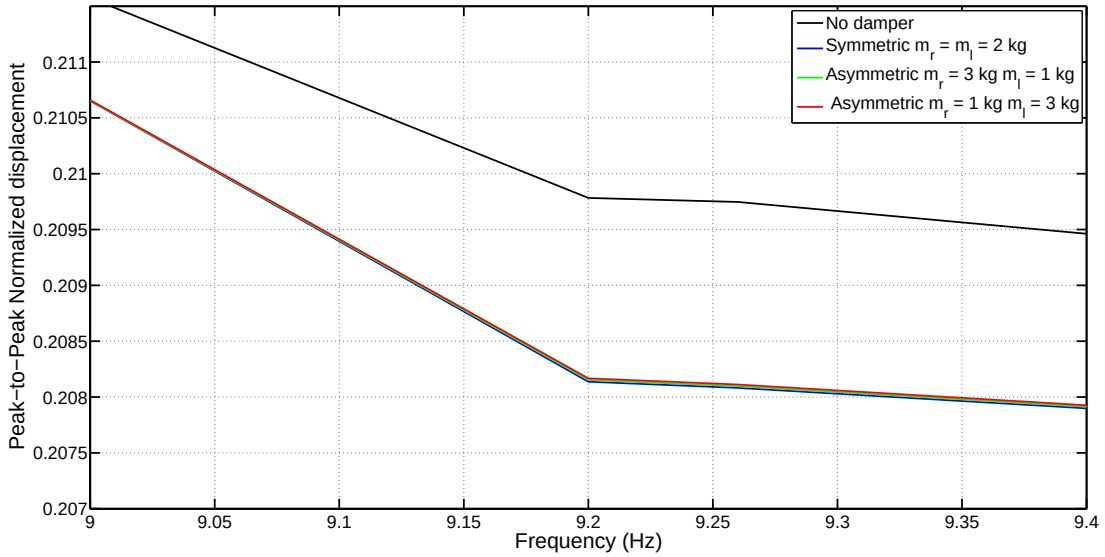

Figure 5.13: Specific range of Figure 5.12

Figures 5.14 and 5.15 show the behaviour of the left and right nodes for the various forcing frequencies.

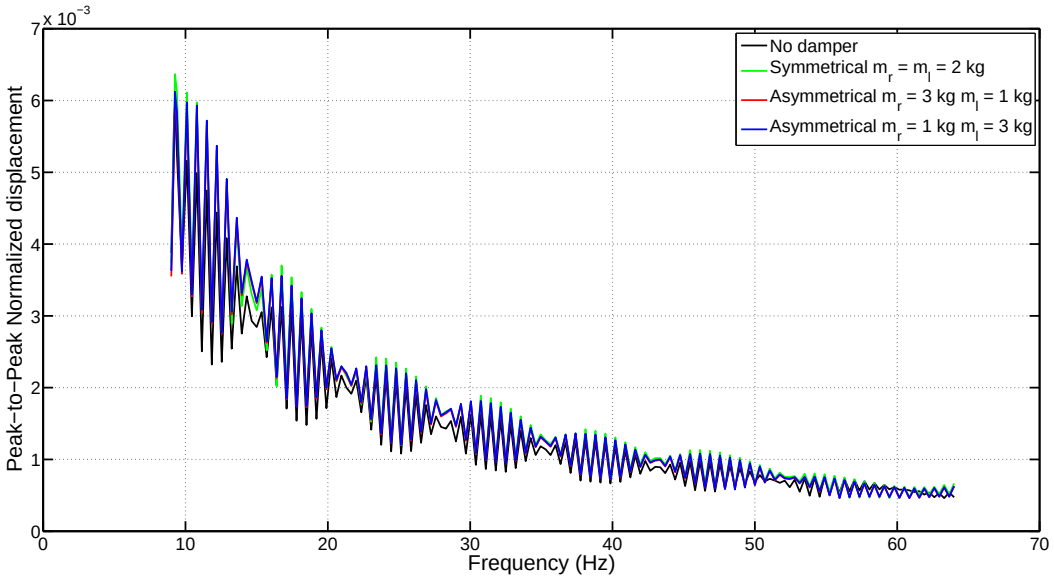

Figure 5.14: Left node displacement for the various cases for varying forcing frequency.

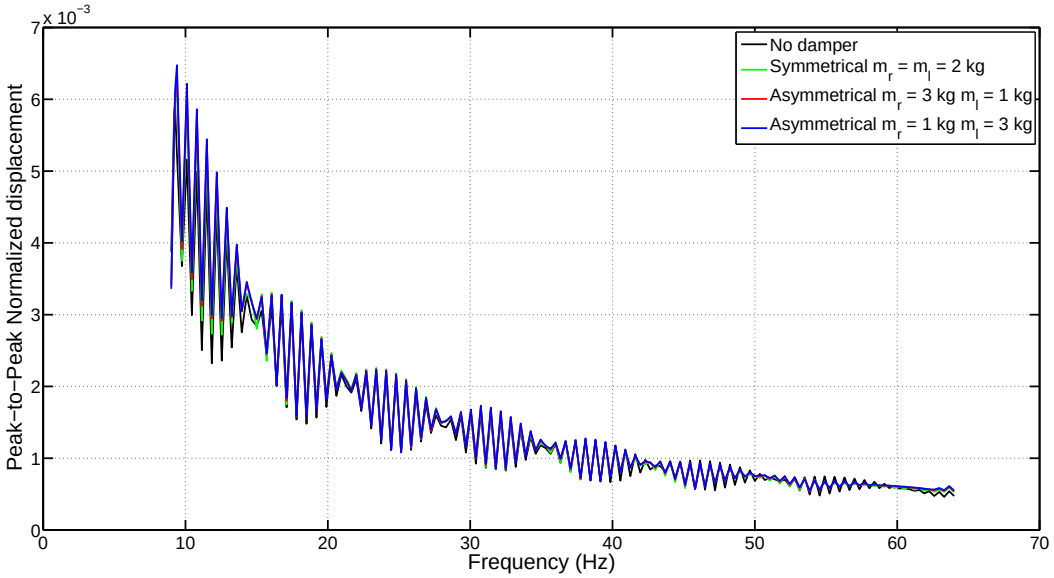

Figure 5.15: Right node displacement for the various cases for varying forcing frequency.

Both the left and right nodes apparently show the same behaviour, but slightly different from the node with maximum displacement. Even though the displacement decreases as the frequency increases, this decrease in value is not monotonous, showing to have larger variations in the start of the vortex-shredding frequency range and lowering when the value of frequency increases. These variations appear to be larger for the left node when in comparison with the right node.

Regarding the effectiveness of the damper for the right and left nodes, the damperless case actually proves to have lower values of displacement (albeit not a significant difference between the damperless and the damped cases) for lower values of frequency, becoming undistinguishable the difference between all the cases as the forcing frequency increases.

5.3.3 Simulation with varying damper location

This simulation was chosen in order to understand the effect that the damper has when its location from the left suspension clamp is varied. The forcing frequency is constant at $f = 9.26$ Hz, with $T = 25\%$ of the RTS.

It was said previously that the normal range of distance for the damper position from the suspension clamp would be between 0.5 to 5 m, due to the feasibility of implementation of the solution. However, this simulation was extended for a distance up to 10 m, and the reason will be explained further.

The results of the analysis are presented in Figure 5.16, for the values of $\overline{Y_{max}}$. The only cases considered were the second, third and fourth cases previously mentioned, due to the fact that the first case does not have any Stockbridge damper.

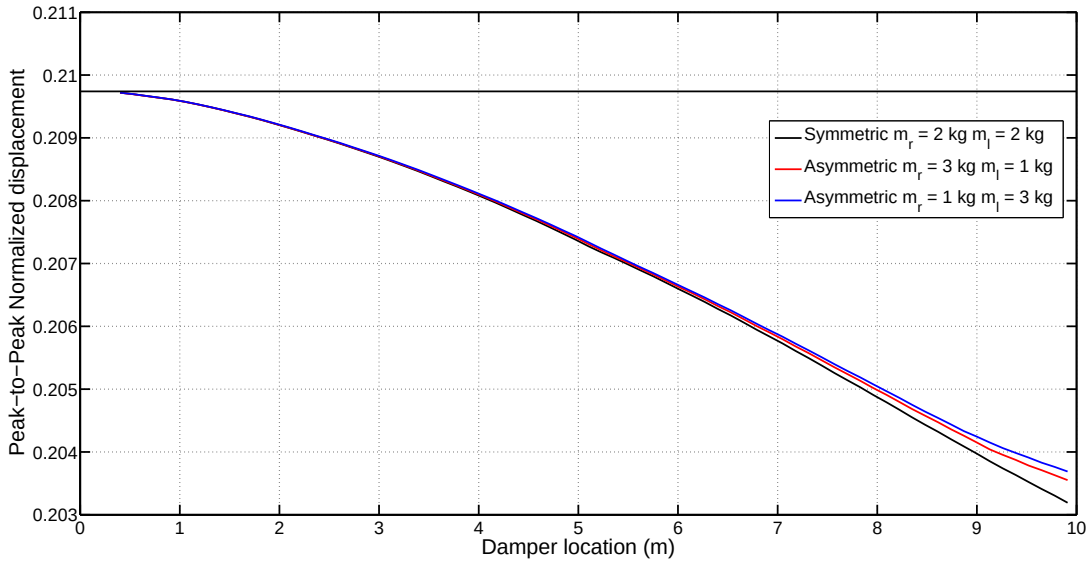

Figure 5.16: Maximum displacement versus damper location.

The results show a tendency of the value of $\overline{Y_{max}}$ to decrease with the increase of the damper's location throughout the span. The reason for this monotonous decrease is due to the consideration of the first mode of vibration being, in fact, the dominant mode.

This leads for a larger loop length where, in reality, the loop length of the first mode of vibration would be the entirety of the span, positioning the antinode at mid-span. Therefore it would be safe to assume that the maximum displacement would continuously decrease until half of the span length.

At the limiting distance of 5 m it is possible to notice only a slight difference between the three cases, with the symmetrical damper having a slight advantage over the remaining cases. This difference is significantly noticeable as the damper location increases for distances larger than 5 m.

Finally it is also possible to see a large black horizontal line on the plot (corresponding to the maximum displacement for a damperless case). This line shows the point at which is justified to use any type of damper which, in this case, is always efficient for the range chosen for the simulation.

As a final remark for this chapter, consider the behaviour of each of the damper's counterweights, which can be seen in Figure 5.17, for the symmetrical damper (second case).

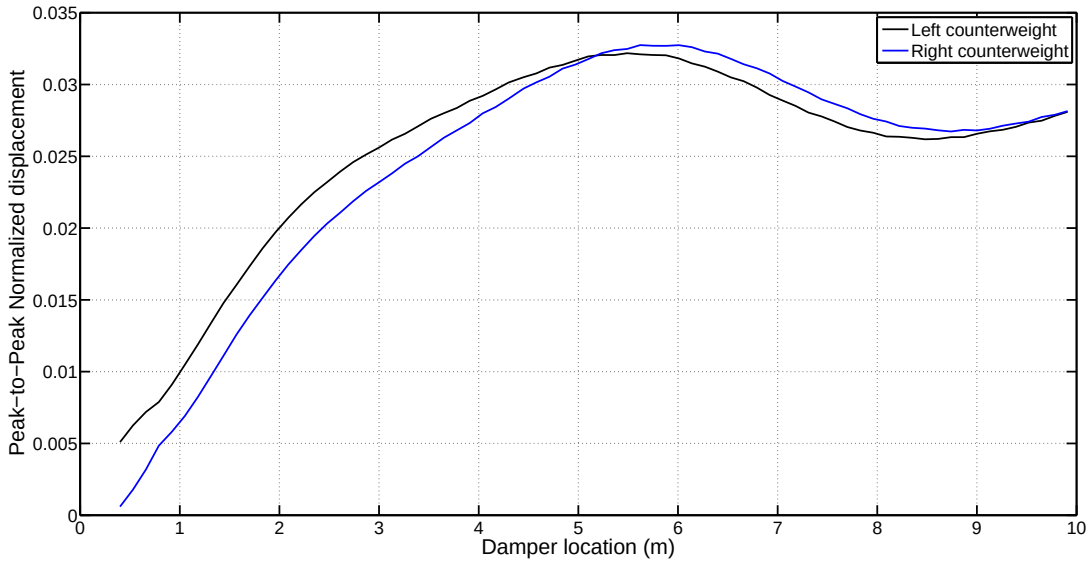

Figure 5.17: Damper's counterweights displacement versus damper location, for the symmetrical damper.

The behaviour with slight oscillation in the vicinity of the 4 to 10 m mark can be due to the fact of the counterweights being positioned at nodes or antinodes of the 25th mode shape, where the anti-node should be positioned at around 4 m. Remember that the 25th mode does not produce a large displacement as the 1st mode. It is then possible to conclude that the damper can be more susceptible to the conductor's own overlay of the two modes of vibration, in terms of displacement, than the conductor itself.

The damper's displacement variation with the damper location for the asymmetrical dampers are illustrated in Figures 5.18 and 5.19.

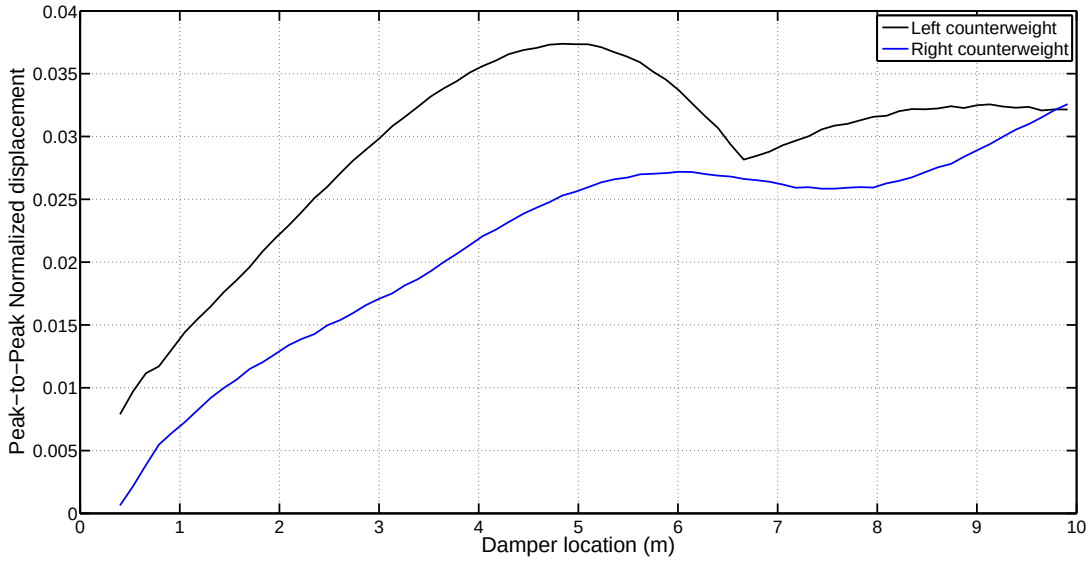

Figure 5.18: Damper's counterweights displacement versus damper location, for the asymmetrical damper with a right counterweight mass of 1 kg and a left counterweight mass of 3 kg.

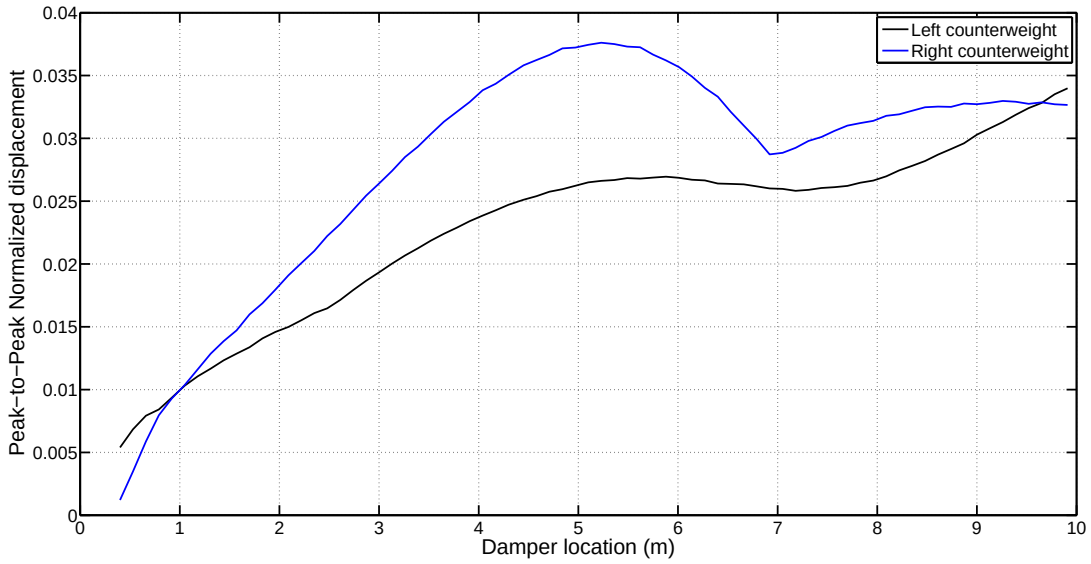

Figure 5.19: Damper's counterweights displacement versus damper location, for the asymmetrical damper with a right counterweight mass of 3 kg and a left counterweight mass of 1 kg.

5.3.4 Simulation with varying damper mass

For this simulation a constant forcing frequency of $f = 9.26$ Hz and a fixed damper location of 4 m from the left suspension clamp was chosen. In this analysis the values of both the counterweights are varied at the same time, to cover all the possibilities of symmetry and asymmetry.

Figures 5.20 and 5.21 present the evolution of the maximum and mid-span displacements.

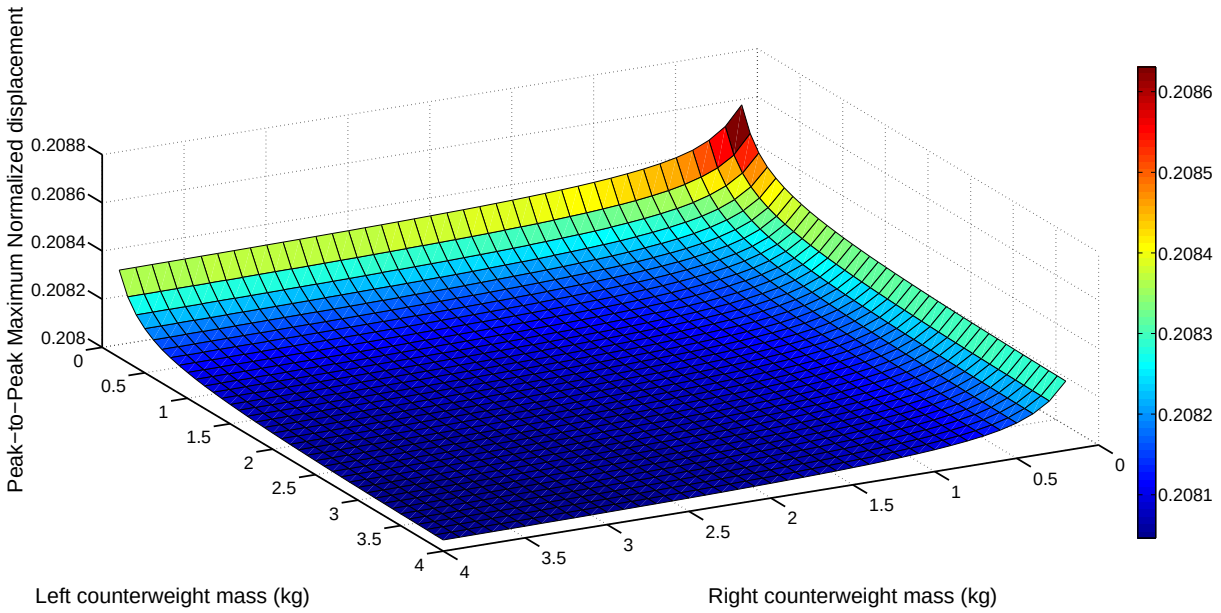

Figure 5.20: Maximum displacement for varying damper's counterweight masses.

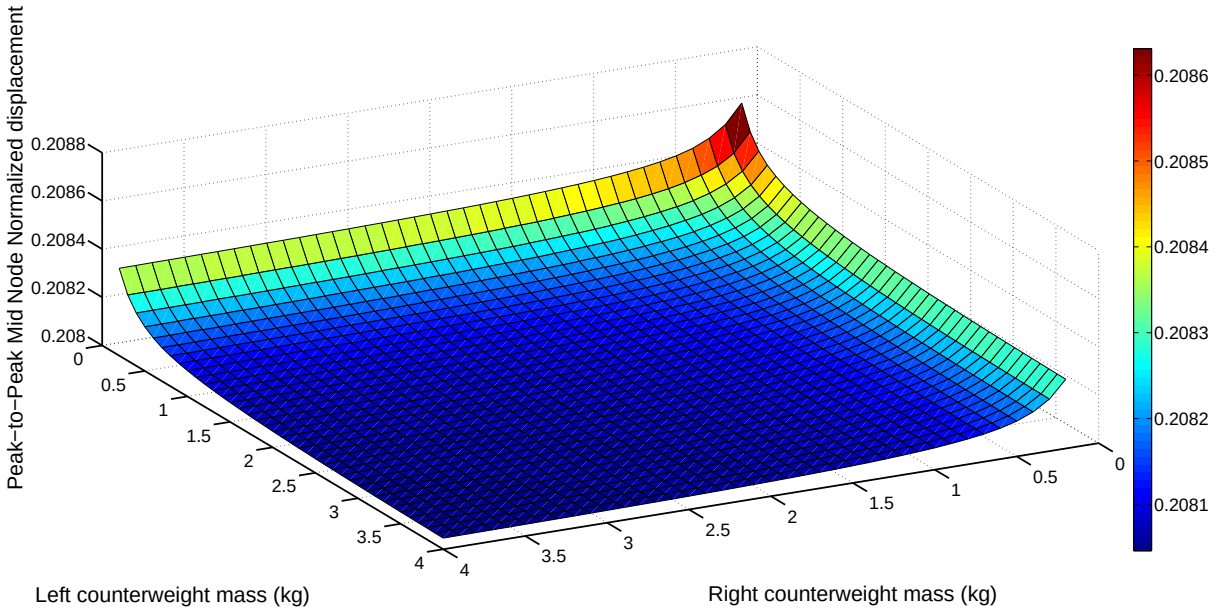

Figure 5.21: Mid-span displacement for varying damper's counterweight masses.

Both the figures show that the node with maximum displacement and the mid-span node present the same behaviour when the counterweight's masses are varied. They proved to be highly sensitive for dampers with very low mass, and being very insensitive to damper mass variations when the total mass of the damper (the sum of both the counterweights) is approximately larger than 1 kg.

Regarding the asymmetric distribution of the counterweights, the analysis proves to favor the dampers with larger weights on the left side than on the right side. In this case, the left counterweight is the one facing the suspension clamp. This does not correspond with what has been seen in previous analysis, but since this analysis covers the entire spectrum of damper weight combinations and that the previous sections covered specific damper distributions it is safe to assess that this analysis and conclusion are correct.

Figures 5.22 and 5.23 present the behaviour of the left and right node displacements, respectively.

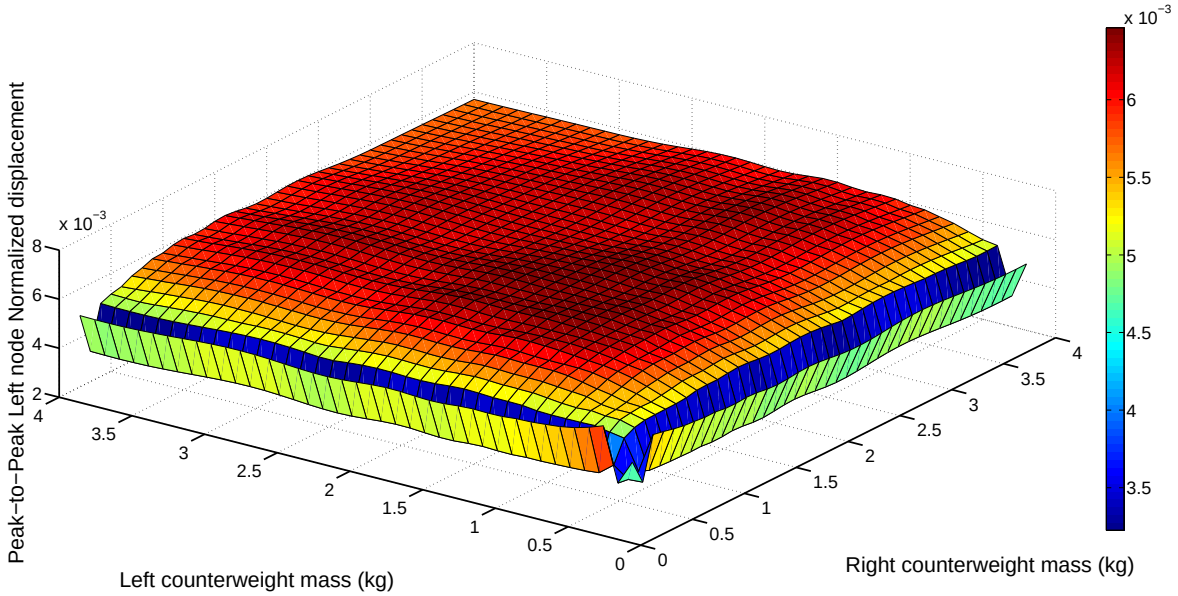

Figure 5.22: Left node displacement for varying damper's counterweight masses.

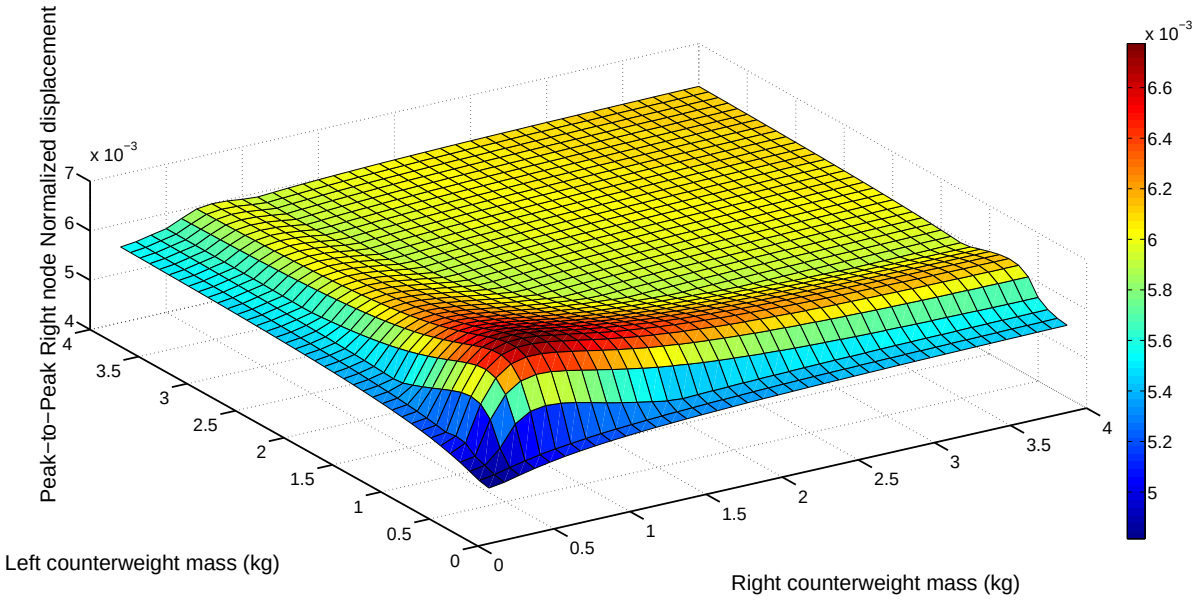

Figure 5.23: Right node displacement for varying damper's counterweight masses.

Even though the graphical representations of the displacements are different, both nodes present very similar behaviours. Their displacements are very sensitive for low mass dampers, either being symmetrical or asymmetrical, with the values stabilizing at a higher total damper mass.

Specifically for the right node, its lowest displacements occur when the damper is lower in mass, with a slight advantage for the symmetric damper case.

5.4 Optimal damper tuning for a conductor with one Stockbridge damper

For this analysis, the damper mass distribution is varied as well as the damper location, in order to determine the best combination of mass and damper location to reduce vibration. The damper is considered as positioned adjacent to the left suspension clamp.

Two cases were considered: the first case is the case where the damper has symmetrical mass distribution up to 5 kg. The second case fixes the total damper mass at 5 kg and runs the simulation for all the asymmetrical combinations of mass, whether being the right or the left counterweight mass the largest. All simulations were done with a forcing frequency of 9.26 Hz.

5.4.1 Simulation for a symmetrical mass distribution

As previously mentioned, this simulation covers all the possibilities of a symmetrical damper for a total damper mass up to 5 kg. Figure 5.24 presents the results of the analysis for the node with maximum displacement.

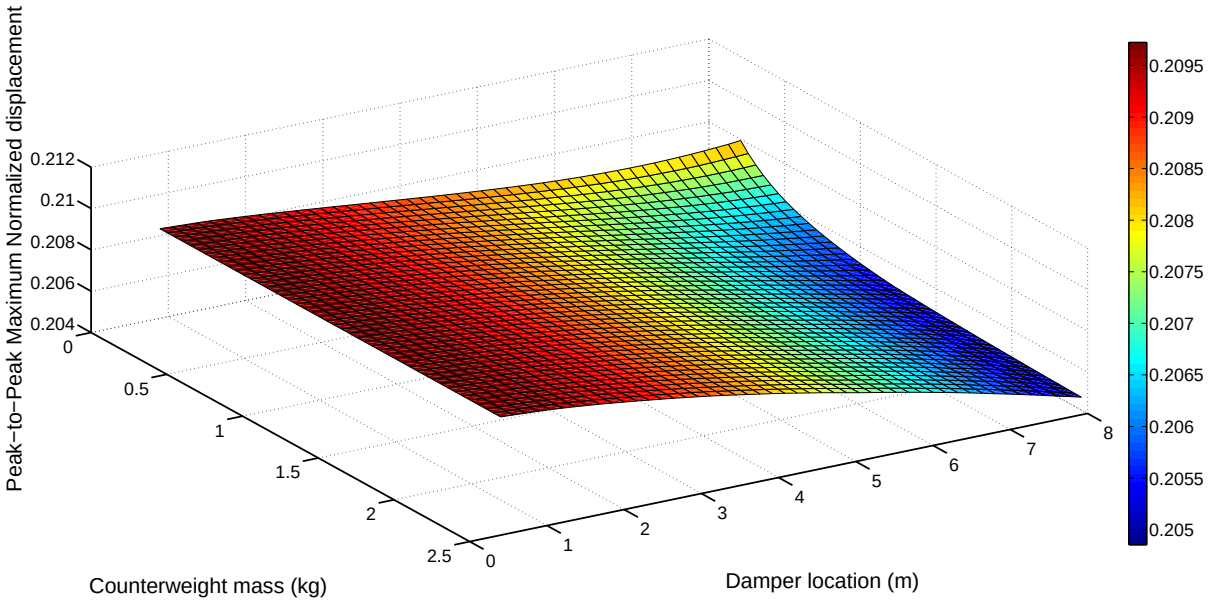

Figure 5.24: Maximum displacement of the conductor for varying symmetrical damper mass and damper location.

Observing the figure it is possible to conclude that, as previously mentioned, the larger the damper distance between the suspension clamp is, the more effective is the damper, although not proving as effective for very lightweight symmetrical dampers. In order to have a significant reduction in the displacement, with a maximum distance of 5 m from the suspension clamp, each of the counterweight should weigh more than at least 1 kg.

This proves that the system of the conductor plus a damper is relatively sensitive to the added inertial forces, as well as the damper location.

5.4.2 Simulation for an asymmetrical mass distribution

As previously mentioned, for this part of the simulation, two different types of cases were chosen in order to fully assess the behaviour of an asymmetrical damper.

The first analysis covers the possibility of an asymmetric damper with a larger left counterweight mass, while the second analysis covers the possibility of an asymmetric damper with a larger right counterweight mass. Figures 5.25 and 5.26 show the previously defined cases, respectively. Recall that the total mass of the damper is fixed at 5 kg, for all asymmetric cases.

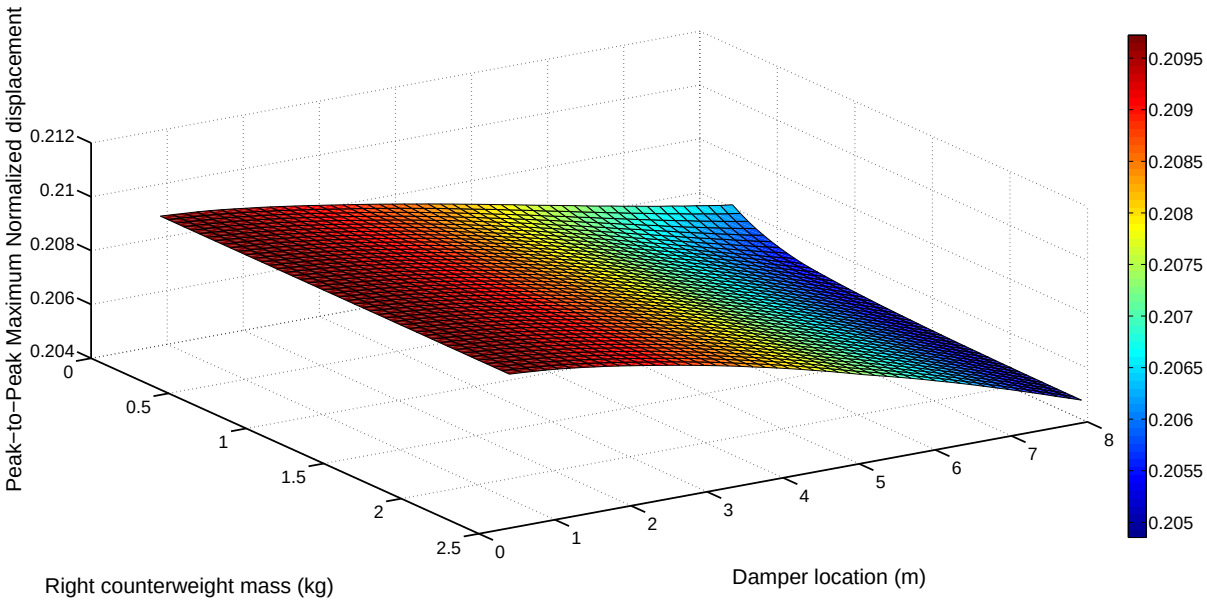

Figure 5.25: Maximum displacement of the conductor for varying asymmetrical damper mass and damper location: case of larger left mass.

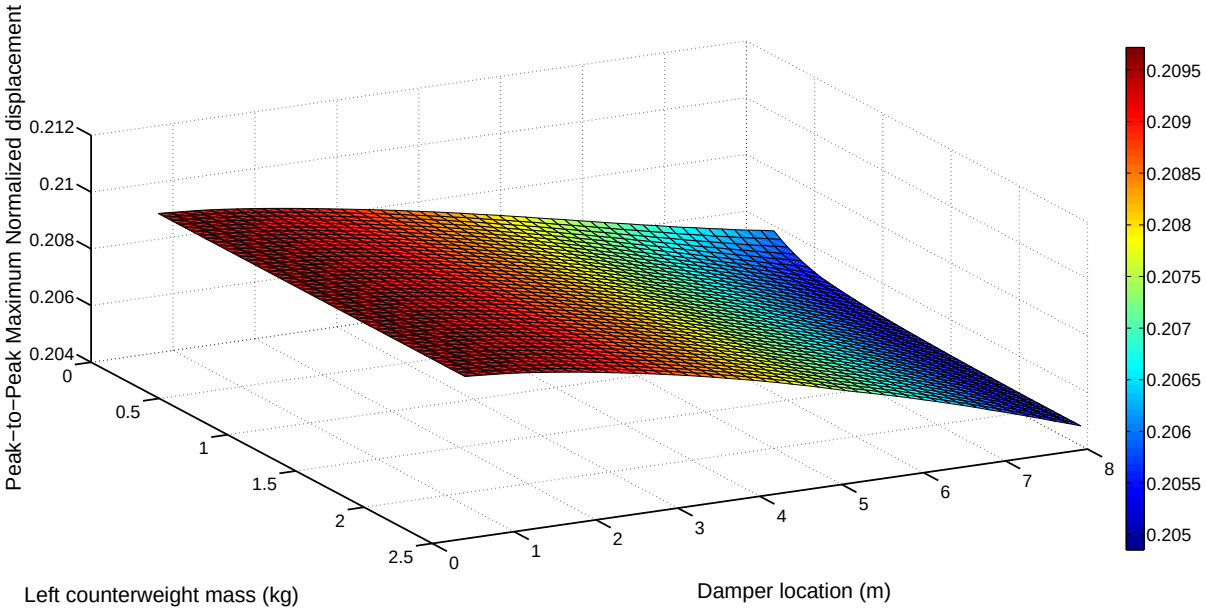

Figure 5.26: Maximum displacement of the conductor for varying asymmetrical damper mass and damper location: case of larger right mass.

Between the two cases, there isn't any visible difference in the behaviour up until to the feasible distance from the suspension clamp of 5 m. And since the total mass of the damper is always 5 kg the behaviour that the symmetrical damper had for a lightweight solution at high damper locations,

does not occur for the asymmetrical damper case, due to the increase of the inertial influence.

Comparing all the cases, both symmetrical and asymmetrical, and considering a damper position of 5 m from the left suspension clamp, three similar cases can be retrieved with equal displacements. The cases are the following:

- A symmetrical damper with $m_r = m_l = 1.1$ kg;
- An asymmetrical damper with $m_r = 1.2$ kg and $m_l = 3.8$ kg;
- An asymmetrical damper with $m_r = 3.8$ kg and $m_l = 1.2$ kg.

All three cases present a maximum peak-to-peak normalized displacement $\overline{Y_{max}}$ of approximately 0.20740. Remembering that the case with no damper applied has a value $\overline{Y_{max}}$ of 0.20974, the reduction in the maximum amplitude is approximately 1.12 %.

This analysis serves to confirm what has been shown in the previous chapters, where a relatively symmetrical lightweight damper can obtain the same values of amplitude reduction as an high mass strongly asymmetrical damper, when only one damper is used.

From now on, a new type of analysis will be introduced, the $\overline{Y_{max}}$ reduction which measures the reduction in the maximum peak-to-peak normalized displacement between a case with no damper $\overline{Y_{max\ u}}$ and a case with a damper $\overline{Y_{max\ d}}$ and can be calculated as:

$$\overline{Y_{max}} \text{ reduction } (\%) = \frac{\overline{Y_{max\,u}} - \overline{Y_{max\,d}}}{\overline{Y_{max\,u}}} \times 100\ \% \tag{5.12}$$

This variable makes possible a more direct analysis of how much of a change an usage of one or more dampers has to the entire mechanical system.

5.5 Implementation of more than one damper

Before introducing the new simulation parameters it is necessary to explain what was considered, in this work, the two forms of implementing more than one damper.

The first form is in the inclusion of dampers as a bundle. Including dampers in this form implies that the additional damper is adjacent to the first damper applied to the conductor. An example of the configuration can be seen in Figure 5.27. The figure also presents the distribution of the additional masses. The additional damper location is measured from the x_1 axis, when in bundle configuration.

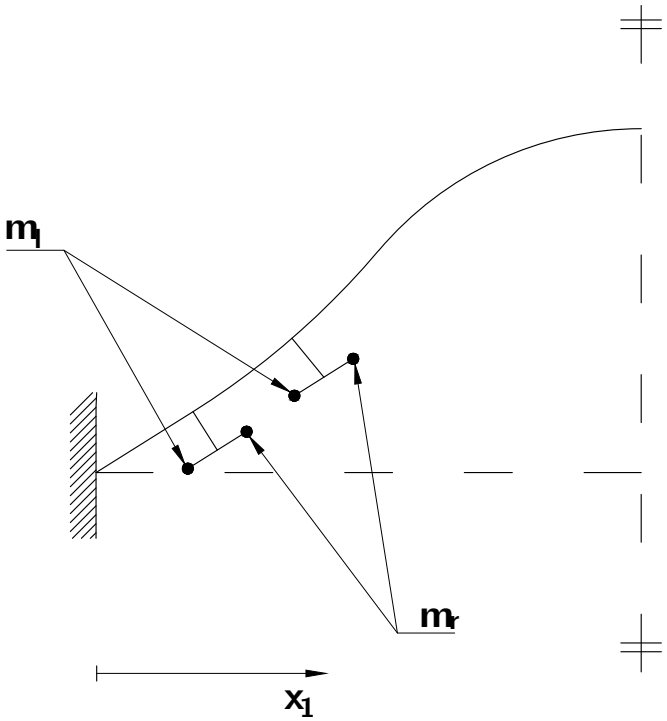

Figure 5.27: An example of a bundle of dampers on a conductor.

The second form of adding an additional damper to the system is on the other side of the span, where both the counterweights masses are displayed symmetrically, in reference to the mid-span of the conductor. Figure 5.28 presents the new configuration of adding dampers, with the respective mass distributions.

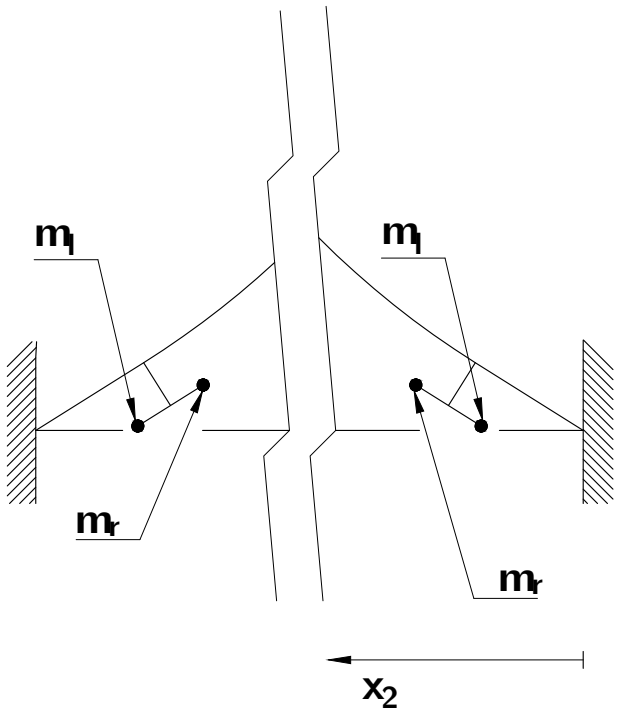

Figure 5.28: An example of span symmetry distribution of dampers.

It is possible to observe that when a damper is added on the opposite side of the conductor, the disposition of the damper masses shift in order to obtain mass symmetry. The position of the damper

in this type of configuration is measured from the x_2 axis.

From this point until the end of the results exposition, when mentioning the counterweight masses, it is relative to the first damper positioned at the left side. Two cases of dampers with the two damper configurations previously defined are used.

The dampers used are:

- Symmetric damper with $m_r = m_l = 1.1$ kg;
- Asymmetric damper with $m_r = 1.2$ kg and $m_l = 3.8$ kg.

Recall that the dampers considered are part of the damper analysis retrieved from the previous optimal damper tuning analysis. The damper configurations are the bundled and span symmetry condition. Figure 5.29 presents the results for the cases above mentioned, regarding the node with maximum amplitude.

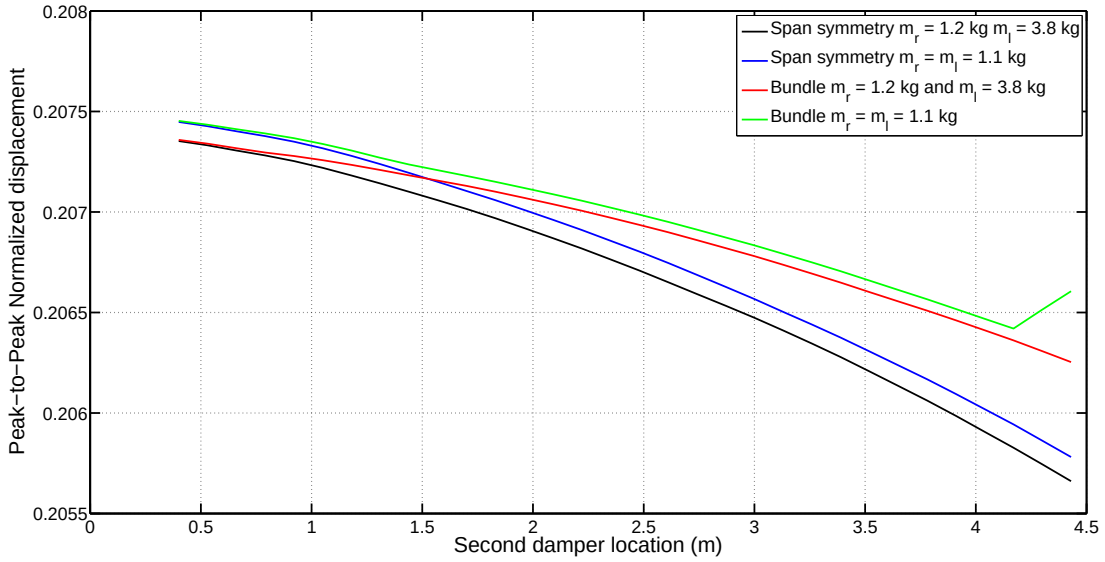

Figure 5.29: Comparison of two types of dampers for two types of configurations, evolution of the maximum amplitude.

As seen in previous cases, when increasing the damper location, either in a bundle condition or positioning them on the other side of the span, the value of maximum displacement effectively reduces, more effectively when a damper is located on the other side of the span. There is however, an exception, of the symmetrical bundled damper for damper locations larger than 4 m.

In a symmetrical configuration, the damper that presented the largest reduction in the maximum displacement was effectively the asymmetrical damper, contrary to what was seen in previous cases where only one damper was applied, the symmetrical damper proved to be slightly more effective. One of the most significant reasons why the asymmetrical damper reduces more vibration than the symmetrical is due to the fact that the total mass of the damper is considerably larger (up to 2 times). It is then possible to conclude that the choice of the dampers must have in consideration the position of the dampers, as well as the number of dampers necessary to reduce the maximum amplitude.

In order to prove which of the asymmetrical dampers was more effective, a comparison is done, with the results presented in Figure 5.30.

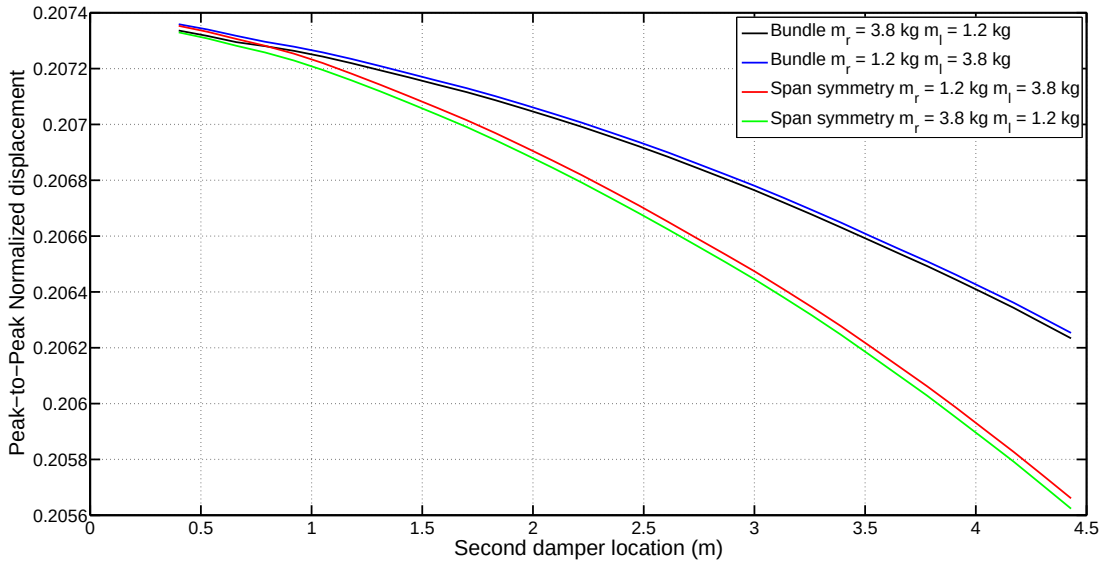

Figure 5.30: Maximum amplitude of two types of asymmetrical dampers for two types of configurations.

As expected, the bundle configuration of dampers proved to be the less efficient solution. When comparing the cases of asymmetrical dampers with a case of span symmetry, the damper that has the right counterweight as the largest mass, is the case that proves to produce more significant reduction in vibration, albeit not a significant one.

To further understand the effect of the vibration reduction when dampers are applied, a similar thought process as proposed by [Lu and Chan, 2007] was chosen, where six dampers were applied, three on each extremity of the span, symmetrically positioned from the mid-span, as well as the counterweight masses. For the left span each damper is positioned at 4, 4.5 and 5 m, respectively. The dampers of the right span are positioned symmetrically from the mid-span.

Four cases were considered:

- Case 1 - No dampers on the conductor;
- Case 2 - Symmetrical dampers where $m_r = m_l = 1.1$ kg;
- Case 3 - Asymmetrical dampers where $m_r = 3.8$ kg and $m_l = 1.2$ kg;
- Case 4 - Asymmetrical dampers where $m_r = 1.2$ kg and $m_l = 3.8$ kg.

For this simulation, in order to properly locate the dampers, the number of finite elements of the simulation was raised to 450. This change in element discretization required the recalculation of the displacement of the nodes for a damperless case. It is expected for the displacement of the node with maximum displacement to slightly increase and both the left and right node displacements to significantly reduce. This significant reduction is due to the fact that, as discretization increases, the left and right nodes become closer to each of their adjacent suspension clamps, that also due to the boundary conditions applied will result in a significant displacement reduction. Table 5.6 presents the results for all the simulations.

Table 5.6: Values of noteworthy nodes for the various cases with no damper and 6 dampers

ACSR conductor with $f = 9.26$ Hz					
Case	**Peak-to-peak normalized displacements**				$\overline{\mathbf{Y_{max}}}$ **reduction**
	$\overline{\mathbf{Y_{max}}}$	$\overline{\mathbf{Y_{mid}}}$	$\overline{\mathbf{Y_l}}$	$\overline{\mathbf{Y_r}}$	**%**
1	0.20999	0.20999	0.00327	0.00327	—
2	0.20535	0.20139	0.00402	0.00400	2.21
3	0.20228	0.20121	0.00393	0.00394	3.67
4	0.20269	0.20123	0.00404	0.00400	3.48

As expected, for the damperless case, the node with maximum displacement slightly increases as the number of elements increases and both the left and right node displacement decrease.

Here it is evident that an asymmetrical damper, when in a condition of more than one damper applied, produces a significant reduction in aeolian vibration, when compared to the symmetrical damper case, but at a significant cost in terms of damper mass, since the mass is considerably larger. The case of asymmetrical dampers with the same mass as a symmetric damper will be covered in the following sections.

Regarding the asymmetry of the dampers, the damper with larger mass in the right counterweight produces higher reductions in the maximum displacement when comparing to the other asymmetric damper, albeit not a significant difference, in accordance with the previous simulated cases.

As for the left and right node, the difference throughout all cases, it is proven that they might not be the best reference points to measure the behaviour of the conductor when dampers are applied and, therefore, the estimation of fatigue behaviour.

They do, however, provide information as to which disposition the conductor will have in their adjacent sides.

One of the most significant reasons why 6 dampers applied to such a system do not result in a large reduction of vibration might be due to the fact that the dampers don't have enough capacity to absorb the condutor vibration energy due to the high inertia of this conductor with 200 m.

5.5.1 Bending amplitude calculation

Remembering that the bending amplitude is directly related to the maximum amplitude of vibration of the conductor and that it can be calculated as [Vecchiarelli, 1997]:

$$Y_b = \frac{\overline{Y_{max}}}{2} \times \sin\left(0.089\frac{n\pi}{L}\right) \times 1000 \quad \text{mm} \tag{5.13}$$

The formula has been adapted to fit the variables used for this problem, as explained in Chapter 4.4. However, since there are no true reference values for an ACSR conductor of bending amplitude, ([Vecchiarelli, 1997] used values for an "Hawk" type conductor which showed similar mechanical properties of an ACSR conductor), this work will only present a relative analysis between the damped and undamped cases, through a reduction of bending amplitude variable, ϵ. Given the fact that the amplitude at 89 mm from the suspension is directly related to the maximum amplitude, the reduction of bending amplitude is equals to the reduction of the maximum amplitude. Therefore,

$$\epsilon(\%) = \frac{\overline{Y_{maxu}} - \overline{Y_{maxd}}}{\overline{Y_{maxu}}} \times 100 = \overline{Y_{max}} \text{ reduction.} \tag{5.14}$$

Given this new approach regarding the reduction of bending amplitude, it is simply a matter of changing the question from "Is this conductor safe from fatigue failure?" to, "How much safer is this conductor from fatigue failure?".

Remembering that the forcing frequency is the 25th and given the fact that ϵ is equals to the $\overline{Y_{max}}$ reduction, the reduction of bending amplitude for the second, third and fourth cases are 2.21, 3.67 and 3.48 %, respectively.

The next section will perform a somewhat similar analysis as the one done for this conductor, but with a different span length.

5.6 Influence of the span length

In order to evaluate the effect of the inertia of the conductor itself when dampers are used the same conductor is analyzed, but for a span length of 50 m with an axial tension of 25% of the RTS.

The analysis of the optimal damper tuning for one damper is done, merely for a symmetrical damper case, in order to retrieve the optimum symmetrical damper mass and location, and compare them to equivalent total mass asymmetrical dampers.

For this analysis it is also necessary to recalculate the natural frequencies of the conductor and determine which ones fit the vortex-shredding frequency range.

For a total number of 250 elements for the 50 m conductor the first resonant mode that falls within the frequency range is the 7th mode of vibration with a frequency $f = 10.37$ Hz. Since it is still considerably higher than the lower value of the vortex-shredding frequency range ($f = 9.13$ Hz), firstly the values of maximum displacement for both of the frequencies above mentioned are compared.

For a frequency of 10.37 Hz, the value of maximum peak-to-peak normalized displacement is 0.05194 and for a frequency of 9.13 Hz the peak-to-peak maximum normalized displacement is 0.06158. Given these values it is also possible to conclude that all the frequencies belonging to the vortex-shredding frequency can be considered resonant modes (or slight approximations of it), as proposed by [Meynen et al., 2005]. This is mainly due to the consideration of the minimum flexural rigidity EI, considering the behaviour of the conductor as similar to a string. For the following analysis, the forcing frequency used will be $f = 9.13$ Hz.

As mentioned previously, the optimum damper tuning analysis was done in order to determine the best location and damper mass distribution for a symmetrical damper, for just one damper positioned adjacent to the left suspension clamp.

Figures 5.31 and 5.32 present the evolution for the maximum and mid-span node displacements which present, to some extent, the same behaviour.

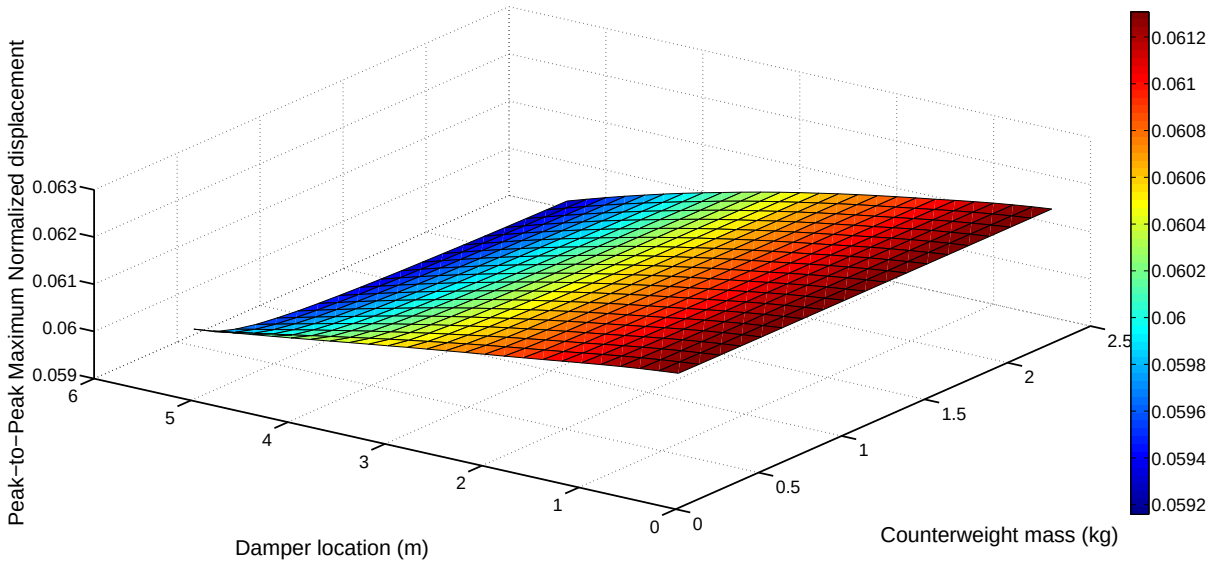

Figure 5.31: Optimal damper tuning for a symmetrical damper - maximum displacement node evolution.

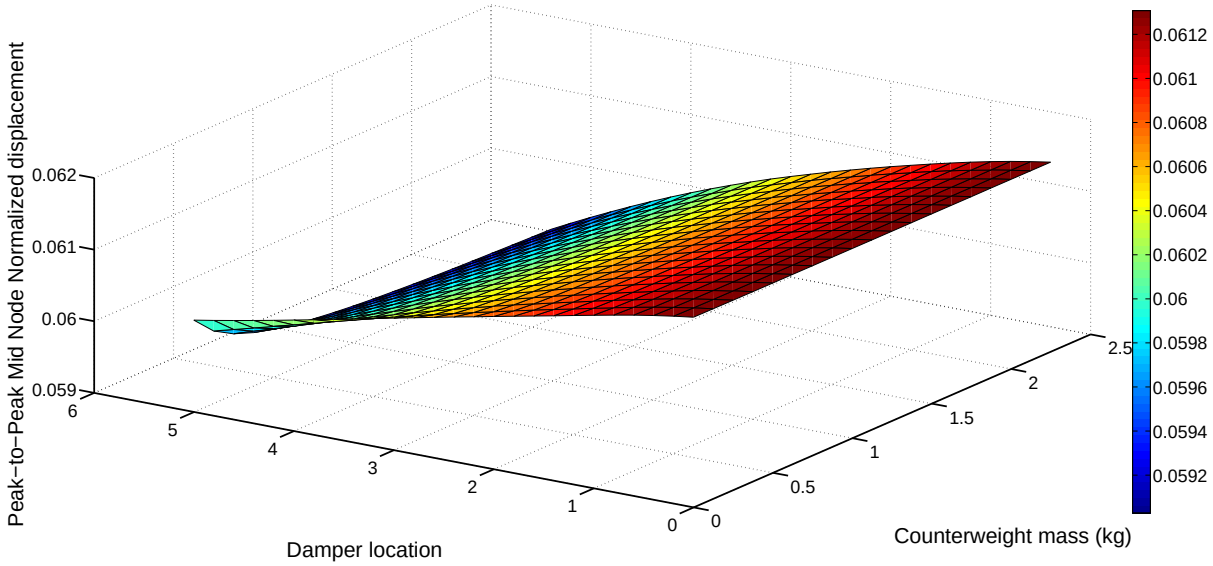

Figure 5.32: Optimal damper tuning for a symmetrical damper - middle node evolution.

To no surprise, the evolution of both the displacements decrease as the damper location increases, although the maximum node displacement is not as sensitive for low counterweight masses, as observed for the case with 200 m of span length.

Figures 5.33 and 5.34 present the behaviour of the left and right node, respectively.

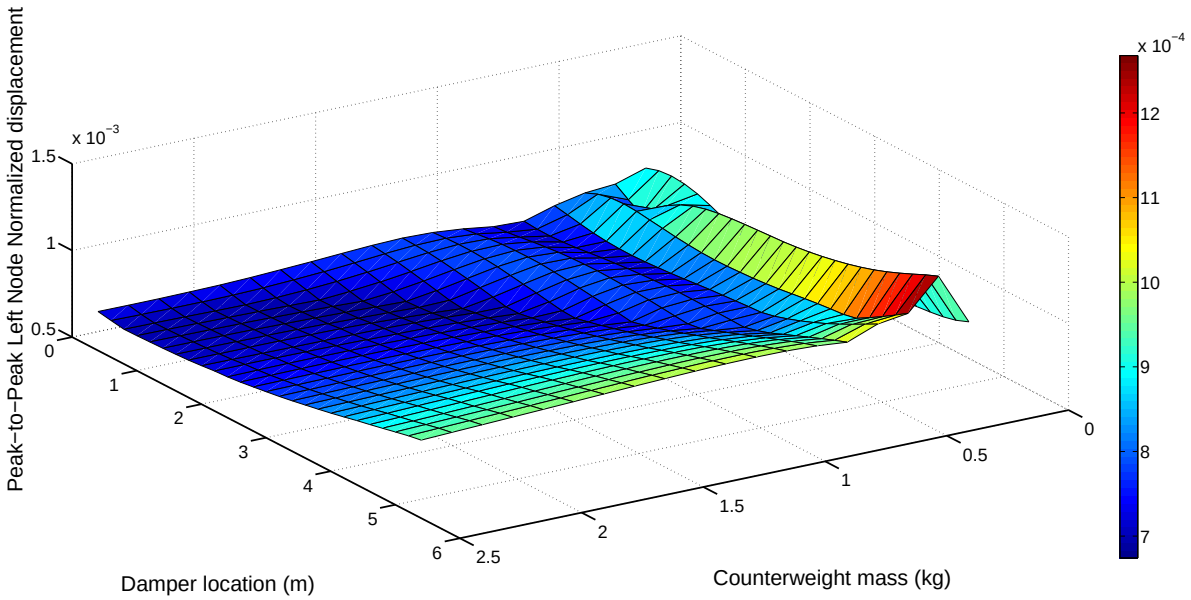

Figure 5.33: Optimal damper tuning for a symmetrical damper - left node evolution.

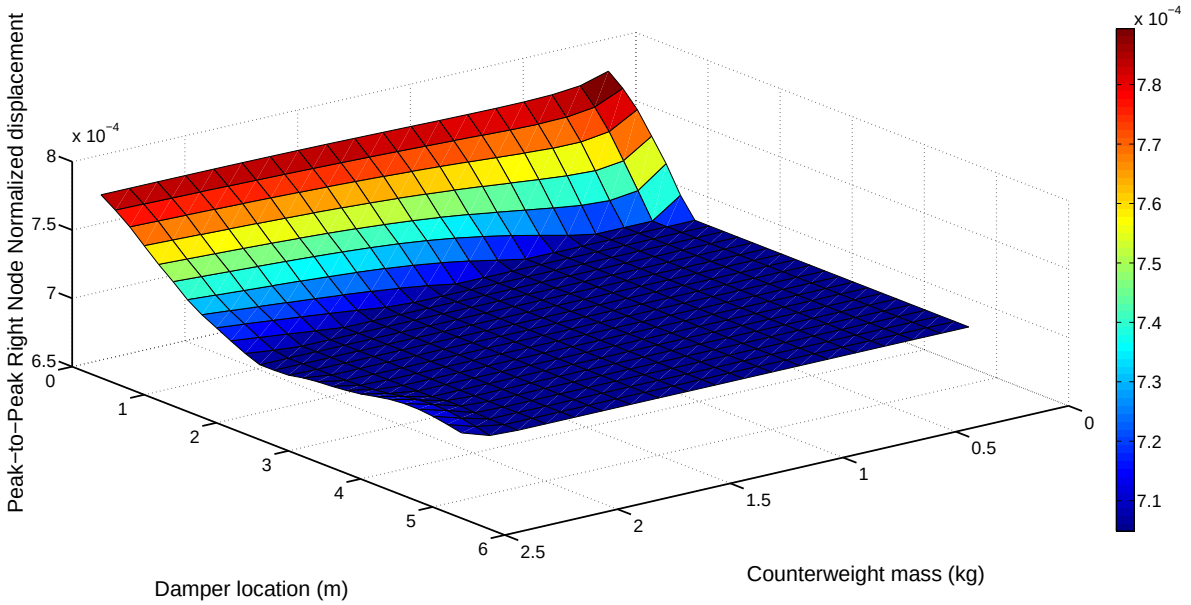

Figure 5.34: Optimal damper tuning for a symmetrical damper - right node evolution.

As opposed to the case with a span length of 200 m, both the left and right node present significantly different behaviours when compared with the previous case. The left node proves to be more sensitive for low mass dampers, independently of the damper location. For the right node, the displacement is heavily influenced by the position of the damper (recall that the damper is positioned at the opposite side) for low values of damper locations, with the displacement becoming independent of both location and mass when the damper location is larger than 2 m.

Using the data presented in Figure 5.31, a symmetrical damper with a total mass of 2.5 kg was chosen, at a position of 5 m from the suspension clamp.

Four new cases are considered:

- Case 1 - No dampers on the conductor;
- Case 2 - Symmetrical damper with $m_r = m_l = 1.25$ kg;
- Case 3 - Asymmetrical damper with $m_r = 1$ kg and $m_l = 1.5$ kg;
- Case 4 - Asymmetrical damper with $m_r = 1.5$ kg and $m_l = 1$ kg.

With all damper configurations positioned at 5 m from the left suspension span, Figure 5.35 demonstrates the evolution of the displacement throughout the conductor span for all cases, for a forcing frequency of 9.13 Hz.

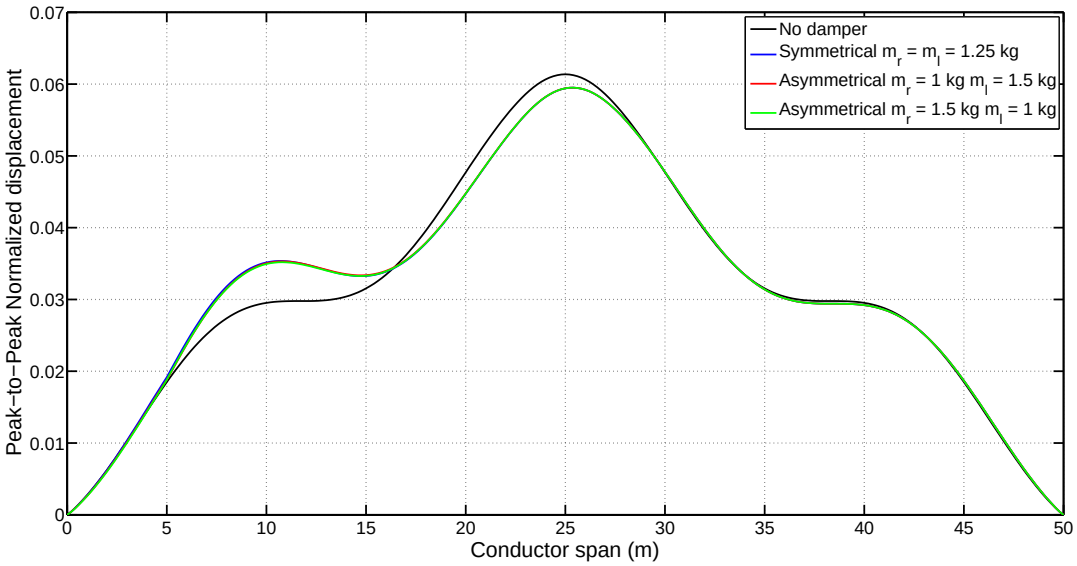

Figure 5.35: Evolution of the displacement throughout the conductor span for a span of 50 m.

Contrary to what happened with the span length of 200 m, the introduction of a single damper introduces a significant reduction of the maximum displacement of the conductor, albeit it does also cause a significant increase of displacement in the part of the conductor adjacent to where the damper is located. This phenomenon can be explained due to the fact that the movement of the mechanical system is at a frequency range that the damper is efficient, leading to larger displacements of the damper counterweights and effectively forcing the damped side of the conductor to be larger, a similar behaviour to what was shown in Chapter 5.2.4, where the conductor's maximum displacement would gradually go from the mid-span to the side, when damping is present.

What it is also visible is the minimum difference between all the cases with damper.

In order to better understand this phenomenon the same cases are simulated, but for a new number of elements, in this case, 400. The values of the analysis are presented in Table 5.7.

Table 5.7: Values of displacement for various noteworthy nodes for a span length of 50 m

ACSR conductor with f = 9.13 Hz					
Case	**Peak-to-peak normalized displacements**				$\overline{Y_{max}}$ **reduction / ϵ**
	$\overline{Y_{max}}$	$\overline{Y_{mid}}$	$\overline{Y_l}$	$\overline{Y_r}$	**%**
1	0.06158	0.06158	0.00041	0.00041	—
2	0.05969	0.05960	0.00056	0.00041	3.07
3	0.05971	0.05963	0.00056	0.00041	3.03
4	0.05969	0.05959	0.00056	0.00041	3.07

What is most important to retrieve from the data shown is the reduction of the values of the maximum displacement. With the addition of only one damper, the reduction of the maximum displacement is of equal magnitude as the one registered by the conductor with a 200 m span and 6 dampers. It is possible to conclude that the conductor length stands as an important factor when analyzing the effectiveness of dampers. It is also visible from Table 5.7 and Figure 5.35 that the damped side appears slightly larger values than the undamped side.

The worst case of damping (third case) was selected for two analysis, where firstly another damper would be added as a bundle configuration, and secondly where a second damper was already attached and another damper would be attached, again in a bundle configuration, having 3 dampers in total by the end.

Figure 5.36 presents the case where one damper is positioned in a bundle configuration, when already one damper is attached at 5 m from the suspension clamp.

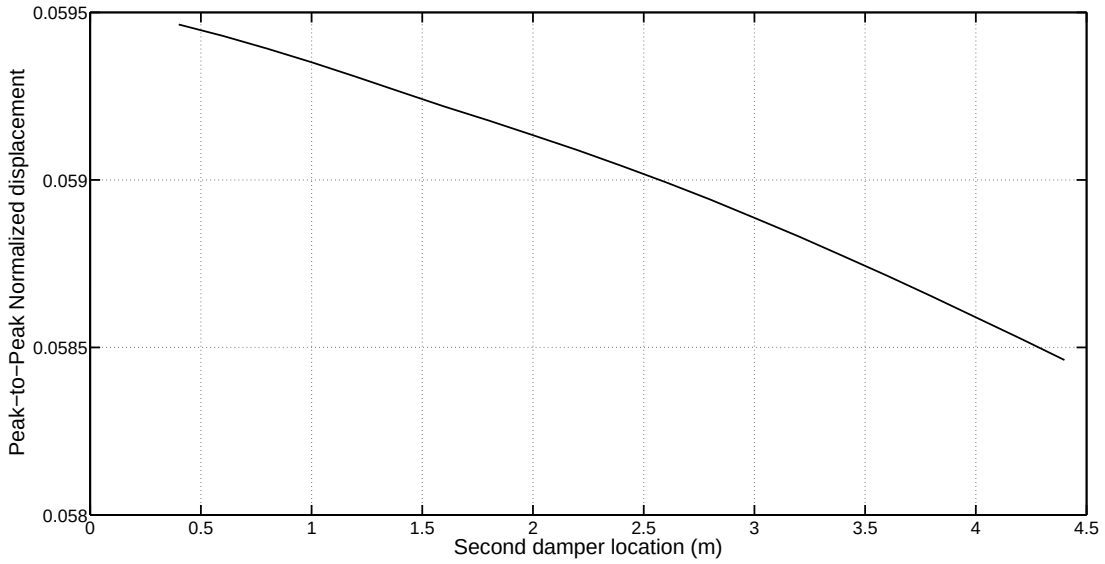

Figure 5.36: Evolution of the maximum displacement of the conductor for a second damper addition.

As expected, the value of the maximum displacement monotonously decreases as the damper approaches the position of the first damper (which represents the limit of feasibility of the damper application).

Figure 5.37 presents the case where already 2 dampers are positioned adjacently to the left suspension clamp at a distance of 4.5 and 5 m, showing the same behaviour as Figure 5.36.

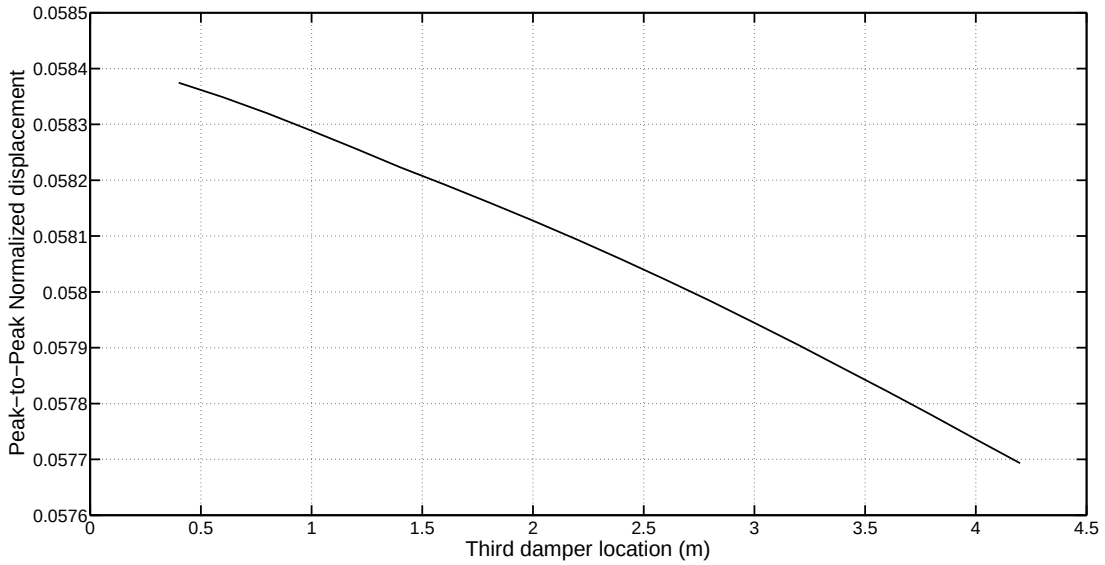

Figure 5.37: Evolution of the maximum displacement of the conductor for a third damper addition.

In order to be able to compare with the case of a span length of 200 m, the same procedure of using 6 dampers is used. The same case dampers previously mentioned with a total damper mass of 2.5 kg are used, with 3 dampers positioned in the left side at 4, 4.5 and 5 m from the left suspension clamp. The right-sided dampers are positioned symmetrically from the mid-span, as well as the counterweights. The results are presented in Table 5.8.

Table 5.8: Comparison of displacement values for noteworthy nodes for a span of 50 m and 6 dampers.

ACSR conductor with f = 9.13 Hz					
Case	**Peak-to-peak normalized displacements**				$\overline{Y_{max}}$ **reduction / ϵ**
	$\overline{Y_{max}}$	$\overline{Y_{mid}}$	$\overline{Y_l}$	$\overline{Y_r}$	**%**
1	0.06158	0.06158	0.00041	0.00041	—
2	0.05386	0.05386	0.00059	0.00058	12.5
3	0.05389	0.05389	0.00058	0.00058	12.5
4	0.05385	0.05385	0.00058	0.00057	12.6

The same behaviour as seen in the previous analysis is seen here for 6 dampers, except that the reduction of the maximum amplitude and bending amplitude is considerably larger when comparing to when only one damper is used and also significantly larger to when 6 dampers are used for a span length of 200 m, proving that larger span lengths are less affected by damper usage.

What is also visible is the behaviour of the left and right side of the span. Since the dampers are, apparently, in a frequency range in which they are efficient, the sides of the conductor will gradually increase, as the node with maximum displacement near the middle effectively decreases. This behaviour can be seen graphically in Figure 5.38, with a comparison between the damperless case and the symmetrical damper case.

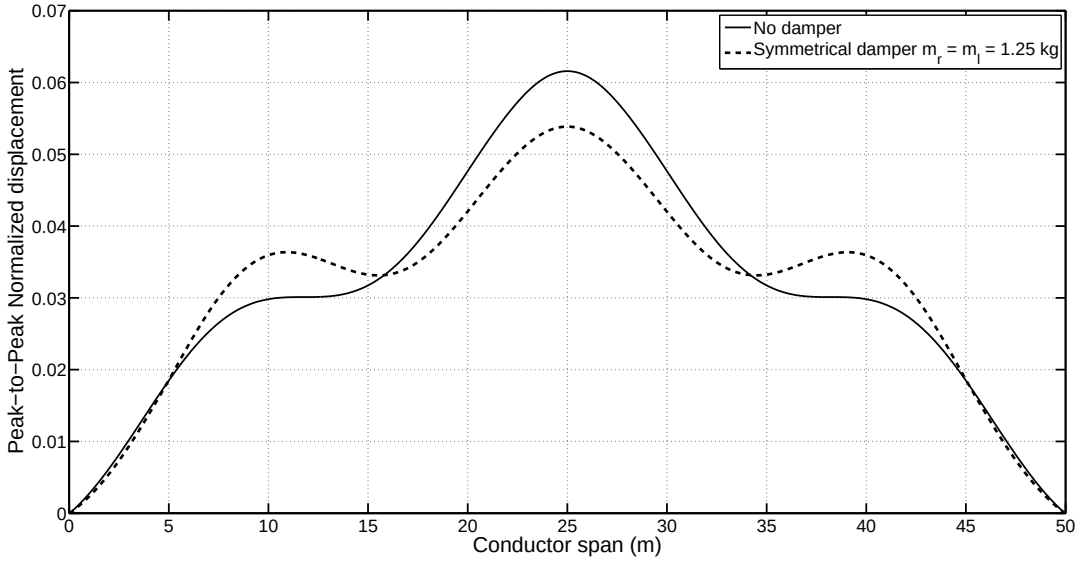

Figure 5.38: Peak-to-peak normalized displacement throughout the conductor span.

Another study conducted is the effect of stronger asymmetry conditions on asymmetric dampers and the effects of damper inertia on the conductor.

For the first part the following cases were considered, for the same total damper mass of 2.5 kg:

- Case 1 - No dampers on the conductor;
- Case 2 - Symmetrical damper with $m_r = m_l = 1.25$ kg;
- Case 3 - Asymmetrical damper with $m_r = 0.5$ kg and $m_l = 2$ kg;
- Case 4 - Asymmetrical damper with $m_r = 2$ kg and $m_l = 0.5$ kg.

The results are presented in Table 5.9.

Table 5.9: Displacement values for noteworthy nodes for a span of 50 m and 6 dampers: influence of higher asymmetry

ACSR conductor with f = 9.13 Hz					
Case	**Peak-to-peak normalized displacements**				$\overline{\mathbf{Y_{max}}}$ **reduction / ϵ**
	$\overline{\mathbf{Y_{max}}}$	$\overline{\mathbf{Y_{mid}}}$	$\overline{\mathbf{Y_l}}$	$\overline{\mathbf{Y_r}}$	**%**
1	0.06158	0.06158	0.00045	0.00045	—
2	0.05386	0.05386	0.00059	0.00059	12.5
3	0.05419	0.05419	0.00053	0.00053	12.0
4	0.05400	0.05400	0.00054	0.00052	12.3

It is possible to observe with comparison with the previous case that increasing the asymmetry effectively reduces the efficiency of the dampers against aeolian vibration.

The final study covers the possibility of a larger total damper mass, in this case 5 kg. Therefore, the new four cases are the following:

- Case 1 - No dampers on the conductor;

- Case 2 - Symmetrical damper with $m_r = m_l = 2.5$ kg;
- Case 3 - Asymmetrical damper with $m_r = 2$ kg and $m_l = 3$ kg;
- Case 4 - Asymmetrical damper with $m_r = 3$ kg and $m_l = 2$ kg.

The values for the simulations for all cases are presented in Table 5.10.

Table 5.10: Displacement values for noteworthy nodes for a span of 50 m and 6 dampers: influence of higher total damper mass

ACSR conductor with f = 9.13 Hz					
Case	**Peak-to-peak normalized displacements**				$\overline{\mathbf{Y_{max}}}$ **reduction / ϵ**
	$\overline{\mathbf{Y_{max}}}$	$\overline{\mathbf{Y_{mid}}}$	$\overline{\mathbf{Y_l}}$	$\overline{\mathbf{Y_r}}$	**%**
1	0.06158	0.06158	0.00045	0.00045	—
2	0.05361	0.05361	0.00058	0.00058	12.9
3	0.05363	0.05363	0.00058	0.00057	12.9
4	0.05361	0.05361	0.00058	0.00057	12.9

It is possible to see that when increasing the mass to the double of previous cases, increasing efficiency on the reduction of aeolian vibration is indeed present but not significantly when compared with the case of a total damper mass of 2.5 kg, proving that there is a limit to the inertial influence of the dampers when allocating them into a conductor.

5.6.1 Influence of the axial tension

Two studies were done in order to analyze the influence of the axial tension. The first study covers the case where the conductor is strung at 15% of the RTS and in the second case the conductor is strung at 35% of the RTS. The cases for this study are the same as the one for the calculation of the amplitude reduction, where 6 dampers are used with a total mass per damper of 2.5 kg.

In the first analysis the first mode that falls within the frequency range of vortex-shredding is the 8^{th} mode of vibration with $f = 9.18$ Hz. Since it is a frequency close to the lower value of the range, no modification was deemed necessary for the forcing frequency. The comparison of the maximum values of displacement for all cases are compared in Table 5.11, as well as the amplitude reductions.

Table 5.11: Amplitude values for conductor with T=15% of the RTS and a span length of 50 m

Amplitude comparison for T=15% RTS		
Case	$\overline{\mathbf{Y_{max}}}$	$\overline{\mathbf{Y_{max}}}$ **reduction / ϵ (%)**
1	0.06748	–
2	0.06480	4.00
3	0.06480	4.00
4	0.06480	4.00

The behaviour shown for 25% of the RTS is accentuated for 15% of the RTS, where the existence of a symmetrical or an asymmetrical damper does not lead to any significant variation in the value of maximum peak-to-peak normalized displacement and bending amplitude. The reduction in the value of the maximum displacement for all last three damped cases is of 4 %, proving that when reducing

the axial tension at which the conductor is subjected, the damper efficiency reduces, meaning that the conductor is not as safer from fatigue failure as was the case with $T = 25\%$ RTS.

Lastly, the case where the conductor is strung at 35% of the RTS is considered. The frequency that falls within the range of vortex-shredding is the 6^{th} mode of vibration with a frequency of $f = 10.514$ Hz. Since this value is somewhat larger from the lowest value of the frequency range, a forcing frequency of 9.13 Hz is considered. The results for the analysis are presented in Table 5.12.

Table 5.12: Amplitude values for conductor with T=35% of the RTS and a span length of 50 m

Amplitude comparison for T=35% RTS		
Case	$\overline{Y_{max}}$	$\overline{Y_{max}}$ **reduction / ϵ (%)**
1	0.04853	–
2	0.04145	14.6
3	0.04149	14.5
4	0.04145	14.6

Regarding the reduction of the maximum displacement and bending amplitude, it is possible to conclude that, as the axial tension at which the conductor is strung increases, the effectiveness of the damper usage increases as well, when analysing the values of $\overline{Y_{max}}$ reduction.

It is important to note that this conductor, due to high value of axial tension, which is not used in any of the literature (the range is between 20 to 25 %), is less susceptible to aeolian vibration, proven by the lower values of displacement, but due to the high tension at which the conductor is strung (10 % more than the maximum recommended limit), its safety from fatigue failure due to fretting should not be disregarded, as well as the risk of strand breakage.

5.7 Concluding remarks

The main conclusions to retrieve from this chapter are:

- The conductors present an high modal density and the modes of vibration in the range of the wind forcing frequency bandwidth are high order modes of vibration;
- The movement of the conductor in the initial instants is heavily dominated by the first modes of vibrations, which result in high values of displacement;
- The stationary component presents considerably lower displacement values when compared to the value when the overlay of the transient and stationary components are considered;
- The higher the forcing frequency, the lower the displacement values are;
- When considering the overlay of the transient and the stationary regime, increasing the damper location will always be effective in reducing vibration;
- When adding more dampers to the system, the value of maximum amplitude effectively decreases;
- The displacement reduction is more effective when the span lengths are lower;
- There appears to be a limit for the damper's inertial influence when reducing the conductor's vibration;
- As the axial tension at which the conductor is subjected to decreases, the higher the probability is of the conductor to be in risk of fatigue failure due to leading to larger values of displacement;

- Regarding the asymmetric dampers, the larger counterweight shows larger values of displacement, proving a higher capacity of dissipating energy.

CHAPTER 6

CONCLUSION

With the results gathered from the previous chapters, this chapter tries to expose in a condensed fashion the most important points regarding the study of conductor performance under aeolian vibration, without and with Stockbridge dampers, as well as the possibilities for future work in this field.

6.1 Conclusions

This present work, which resulted from the consideration of a somewhat new approach to the study of aeolian vibration through the implementation of the finite element analysis, produced a vast array of results which proved that the finite element method is a philosophy of approach with very high versatility and richness in terms of data outputs. Regarding the actual performance of the conductor it is possible to conclude that:

- The conductors present an high modal density and the modes of vibration in the range of the wind forcing frequency bandwidth are high order modes of vibration;
- As the forcing frequencies increases, whether considering a damped or an undamped case, the values of the conductor's nodal displacement decrease;
- Given the nature of the real wind behaviour, which is not always steady-state, the first modes of vibrations should be taken into account;
- The values of displacement of the conductor when it enters a damped steady-state regime are considerably lower that when the movement has an overlay of the transient and the stationary regimes;
- For a real case of an undamped response:
  - The conductor presents the overlay of two modes of vibration for brief moments, the stationary mode and the transient mode. In these moments the node with maximum displacement is presented in the middle or near it;
  - The damping of the response leads to the dissipation of the transient regime and therefore existing only the steady-state stationary response;
  - This stationary response leads the changing of the node with maximum displacement from the middle region to each of the extremities of the conductor, near the suspension clamps, with much smaller values of displacement.

- Since the case where the overlap of the two modes would have larger displacements than the stationary regime, locating a damper optimally to reduce the effect of the overlapped modes would lead for it to be always safer from fatigue damage;
- Due to the fact that the first mode is considered, the damper efficiency increases as its placement becomes farther from the suspension clamp (up to a distance of 5 m), leading to it becoming closer to the antinode. This is due to the fact that the loop length of the first form is much larger when compared to the rest of the forcing frequencies;
- For the damped cases, their effectiveness reduces as the span length increases. This is given due to the fact of the damper not having enough capacity to absorb the vibrations of the conductor for larger span lengths;
- To no surprise, when increasing the number of dampers in the system, the maximum displacement of the conductor decreases;
- This decrease, however, is not proportional to the number of dampers and their total value of mass. There appears to be a limit at which the inertial influence of the dampers effectively reduces the displacement of the conductor;
- When utilizing only one damper per conductor, results showed that a symmetrical lightweight damper can have the same results as an asymmetrical damper with much larger mass;
- When using more than one damper, positioning them in a span-symmetry condition is always more favorable than using them in a bundle configuration;
- For the same case when more than one damper is used, there is no significant difference between an asymmetrical damper (both configurations) and a symmetrical one, all with the same total damper mass;
- Regarding the asymmetrical dampers, the larger counterweight mass showed to dissipate more energy than the lower mass counterweight, proving the higher capacity of absorbing vibration;
- When utilizing dampers to reduce aeolian vibration, while the maximum displacement (presented at the middle for an undamped case) decreases, the damped sides appear to have larger displacements when compared to their undamped counterpart. This proves that even considering the overlap of the two modes of vibration of the conductor, when dampers are used, it would show indications of the same behaviour as the damped stationary steady-state response;
- This increase in displacement for the damped side mentioned previously can be explained due to the fact that the conductor-damper mechanical system entered a band of frequencies where the damper is efficient, leading to larger displacements of the damper's counterweights;
- Regarding the axial tension at which the conductor is strung, as the axial tension increases, the values of maximum displacement decrease. The efficiency of the dampers, however, increase.

6.2 Future work

Given the information obtained from this thesis work a number of future works can be proposed:

- The experimental study of the behaviour of the conductor and the Stockbridge damper to complement with the numerical data;

- With the experimental studies for both the components, it would be beneficial the determination of a damping matrix to introduce into the equation of motion;
- Regarding the damping matrix and the implementation in numerical solutions, it would also be beneficial to determine the possibility of considering an hysteretic or a viscous damping matrix;
- The study of considering the Stockbridge damper as a mechanical system with more than four degrees of freedom, due to the flexibility of the messenger cables;
- The study of the effect of the messenger cable length to the conductor performance.

REFERENCES

C. R. F. Azevedo and T. Cescon. Failure analysis of aluminum cable steel reinforced (ACSR) conductor of the transmission line crossing the Paraná river. *Engineering Failure Analysis*, 9(6):645 – 664, 2002. doi: http://dx.doi.org/10.1016/S1350-6307(02)00021-3.

N. Barbieri and R. Barbieri. Dynamic analysis of stockbridge damper. *Advances in Acoustics & Vibration*, 2012:1 – 8, 2012. URL `http://search.ebscohost.com/login.aspx?direct=true&db=a9h&AN=84996022&lang=pt-br&site=ehost-live`.

N. Barbieri, O. H. de Souza Júnior, and R. Barbieri. Dynamical analysis of transmission line cables. part 1 linear theory. *Mechanical Systems and Signal Processing*, 18(3):659 – 669, 2004. doi: http://dx.doi.org/10.1016/S0888-3270(02)00217-0.

O. Barry. Finite element analysis of a single conductor with a stockbridge damper under aeolian vibration. Master's thesis, Ryerson University, Canada, 2010.

M. Boniardi, S. Cinvera, F. D'Errico, and C. Tagliabue. Fretting fatigue phenomena on an all aluminium alloy conductor. *Key Engineering Materials*, 348-349:5–8, 2007.

R. Claren and G. Diana. Mathematical analysis of transmission line vibration. *IEEE Transactions on Power Apparatus and Systems*, 1969. doi: http://dx.doi.org/10.1109/TPAS.1969.292291.

G. Diana and M. Falco. On the forces transmitted to a vibrating cylinder by a blowing fluid. *Meccanica*, 6(1):9–22, 1971. doi: http://dx.doi.org/10.1007/BF02129047.

G. Diana, F. Cheli, F. Fossati, and A. Manenti. Aeolian vibrations of overhead transmission lines: computation in turbulence conditions. *Journal of Wind Engineering and Industrial Aerodynamics*, 46 - 47(0):639 – 648, 1993. doi: http://dx.doi.org/10.1016/0167-6105(93)90332-I.

O. M. Griffin and G. H. Koopmann. The vortex-excited lift and reaction forces on resonantly vibrating cylinders. *Journal of Sound and Vibration*, 54(3):435 – 448, 1977. doi: http://dx.doi.org/10.1016/0022-460X(77)90451-5.

A. V. Guedes, C. F. Matt, and E. S. C. Cavalcanti. Experimental investigation of the dynamic behavior of Stockbridge Dampers. *18th International Congress of Mechanical Engineering*, 2005.

P. Hagedorn. Ein einfaches rechenmodell zur berechnung winderregter schwingungen an hochspannungsleitungen mit dämpfern. *Ingenieur-Archiv*, 49(3-4):161–177, 1980. doi: http://dx.doi.org/10.1007/BF01351330.

P. Hagedorn. On the computation of damped wind-excited vibrations of overhead transmission lines. *Journal of Sound and Vibration*, 83(2):253 – 271, 1982. doi: http://dx.doi.org/10.1016/S0022-460X(82)80090-4.

R. B. Kalombo, R. Loubser, and P. Moodley. Bending stress of stockbridge damper messenger cable: Experimental data and modelling. *18th World Conference on Nondestructive Testing*, 2012.

H. J. Krispin. Optimization of the efficiency of aeolian vibration dampers. *IEEE Power Africa Conference and Exposition Johannesburg, South Africa*, 2007.

A. Lara-Lopez and J. Colin-Venegas. Endurance of dampers for electric conductors. *International Journal of Fatigue*, 23(1):21 – 28, 2001. doi: http://dx.doi.org/10.1016/S0142-1123(00)00072-4.

J. H. Lienhard. *Synopsis of lift, drag, and vortex frequency data for rigid circular cylinders*. Washington State University, College of Enineering - Reserch Division, Pullman, Washington, 1966.

M. L. Lu and J. K. Chan. An efficient algorithm for aeolian vibration of single conductor with multiple dampers. *IEEE transactions on power delivery*, 22(3):1822–1829, 2007.

S. Meynen, H. Verma, P. Hagedorn, and M. Schäfer. On the numerical simulation of vortex-induced vibrations of oscillating conductors. *Journal of Fluids and Structures*, 21(1):41 – 48, 2005. doi: http://dx.doi.org/10.1016/j.jfluidstructs.2005.05.019.

A. Nawrocki and M. Labrosse. A finite element model for simple straight wire rope strands. *Computers & Structures*, 77(4):345 – 359, 2000. doi: http://dx.doi.org/10.1016/S0045-7949(00)00026-2.

E. Oñate. *Structural Analysis with the Finite Element Method. Vol. 2 Beams, Plates and Shells*. Springer, 2013.

J. N. Reddy. *An Introduction to the Finite Element Method*. McGraw Hill, third edition, 2006.

A. S. Richardson. Performance requirements for vibration dampers. *Electric Power Systems Research*, 36(1):21 – 28, 1996. doi: http://dx.doi.org/10.1016/0378-7796(95)01008-4.

D. Sauter and P. Hagedorn. On the hysteresis of wire cables in stockbridge dampers. *International Journal of Non-Linear Mechanics*, 37(8):1453 – 1459, 2002. doi: http://dx.doi.org/10.1016/S0020-7462(02)00028-8.

J. Vecchiarelli. *Aeolian vibration of a conductor with a Stockbridge Type Damper*. PhD thesis, University of Toronto, Canada, 1997.

J. Vecchiarelli, I. G. Currie, and D. G. Havard. Computational analysis of aeolian vibration with a stockbridge-type damper. *Journal of Fluids and Structures*, 14(4):489 – 509, 2000. doi: http://dx.doi.org/10.1006/jfls.1999.0279.

H. Verma and P. Hagedorn. Wind induced vibrations of long electrical overhead transmission line spans: A modified approach. *Wind and Structures*, 8(2):89–106, 2005.

H. Wagner, V. Ramamurti, R. V. R. Sastry, and K. Hartmann. Dynamics of stockbridge dampers. *Journal of Sound and Vibration*, 30(2):207 – IN2, 1973. doi: http://dx.doi.org/10.1016/S0022-460X(73)80114-2.

H. Q. Wang, J. C. Miao, J. H. Luo, F. Huang, and L. G. Wang. The free vibration of long-span transmission line conductors with dampers. *Journal of Sound and Vibration*, 208(4):501 – 516, 1997. doi: http://dx.doi.org/10.1006/jsvi.1997.1196.

H. Wolf, B. Adam, and Z. Bozic. The impact of empirical rules for aeolian vibrations in overhead transmission lines. *Transactions of FAMENA*, 34(2):47 – 58, 2010. URL `http://search.ebscohost.com/login.aspx?direct=true&db=a9h&AN=52412237&lang=pt-br&site=ehost-live`.